MAX PLANCK INSTITUTE FOR
SOLID STATE RESEARCH

Characterization of Atomic Structure and Electrostatic Characteristic in Complex Oxides by 4D-STEM and STEM-EELS

Chao Yang

Dissertation submitted as a requirement for the degree of Doctor of Philosophy
November 2023 – Technical University of Darmstadt (TUD) – D17

Darmstadt, 2023

Characterization of Atomic Structure and Electrostatic Characteristic in Complex Oxides by 4D-STEM and STEM-EELS

Dissertation submitted to the Department of Materials and Earth Sciences at Technische Universität Darmstadt

in Fulfillment of the Requirements for the Degree of Doctor of Philosophy (Dr. rer. nat.)

By

Chao Yang
Max Planck Institute for Solid State Research

Born in Shanxi, China

Referee: Prof. Dr. Christian Kübel
Co-referee: Prof. Dr. Peter A. van Aken

Date of Submission: 01.11.2023
Date of Oral Examination: 12.12.2023

TECHNISCHE UNIVERSITAT DARMSTADT

Darmstadt 2023

Chao Yang: Characterization of Atomic Structure and Electrostatic Characteristic in Complex Oxides by 4D-STEM and STEM-EELS

Darmstadt, Technische Universität Darmstadt
Publication Year of Dissertation at TUprints: 2024
URN: urn:nbn:de:tuda-tuprints-264695
Date of Oral Examination: 12.12.2023

THESIS SUPERVISOR

Prof. Dr. Peter A. van Aken
Professor of Geo-Material Science
Max Planck Institute for Solid State Research
Stuttgart Center for Electron Microscopy (StEM)

THESIS COMMITTEE

Prof. Dr. Christian Kübel
Referee
Professor of Geo-Material Science
Department of Materials & Earth Sciences
Technical University of Darmstadt

Prof. Dr. Peter A. van Aken
Co-Referee
Professor of Geo-Material Science
Department of Geo- and Material Sciences
Technical University of Darmstadt

Prof. Dr. Andreas Rosenauer
Examiner
Professor of Physics
Institute of Solid State Physics
Universität Bremen

Prof. Dr. Lambert Alff
Examiner
Professor of Materials Science
Department of Electrical Engineering and Information Technology
Technical University Darmstadt

Characterization of Atomic Structure and Electrostatic Characteristic in Complex Oxides by 4D-STEM and STEM-EELS

By

Chao Yang

Submitted to the Department of Materials and Earth Sciences on 01.11.2023 in Partial Fulfillment of the Requirements for the Degree of Doctor of Philosophy in Geo-Material sciences

ABSTRACT

Complex oxides exhibit a wide range of intriguing physical properties resulting from intricate atomic arrangements and complex electronic interactions. Accurate characterization of the atomic structure and electrostatic characteristics of these materials is crucial for elucidating their functional properties and enabling the design of novel devices. In this study, we employ advanced electron microscopy techniques, specifically four-dimensional scanning transmission electron microscopy (4D-STEM) and electron energy loss spectroscopy (EELS), to investigate the atomic structure and electrostatic properties of complex oxides.

The 4D-STEM technique enables the acquisition of rich information from electron diffraction patterns, allowing the precise recording of atomic positions and the analysis of complex electron interactions within the crystal lattice. High-resolution images of the atomic structure can be reconstructed, enabling the identification of defects, interfaces, and subtle structural distortions present in the complex oxides. The electrostatic field or charge distribution within a thin sample can also be extracted by calculating the momentum transfer of the electron beam. By combining 4D-STEM with STEM-EELS, one can obtain a comprehensive understanding of the local atomic and electronic structure, as well as the charge distribution and their interactions within specific regions of interest in complex oxides, e.g., defects, interfaces, surfaces, and grain boundaries.

In this thesis, we firstly studied the atomic structure and electrostatic characteristics at a grain boundary (GB) in a $SrTiO_3$ bicrystal. We demonstrate that the Σ5 GB is rich in Ti and poor in Sr. We investigate possible effects on the variation of the atomic electrostatic field, including oxygen vacancies, Ti valence change, and accumulation of cations. A negative charge resulting from a space charge zone in $SrTiO_3$

compensates for a positive charge accumulated at the GB, which is in agreement with the double-Schottky-barrier model. It demonstrates the feasibility of characterizing the electrostatic properties at the nanometer scale by 4D-STEM, which provides comprehensive insights into understanding the GB structure and its associated effects on the electrostatic properties.

We also investigated the atomic structures and electrostatic characteristics at specific regions surrounding a Ruddlesden-Popper fault in a $NdNiO_3$ film, the interfaces between $SrTiO_3$ and $NdNiO_2$, and the surface of the partially reduced nickelate films. The $NdNiO_3$ system has received considerable attention due to the discovery of superconductivity in $Nd_{0.8}Sr_{0.2}NiO_2$. In rare earth nickelates, Ruddlesden-Popper (RP) faults play a significant role in the functional properties, motivating us to investigate their microstructural characteristics and electronic structure. Therefore, we employed aberration-corrected scanning transmission electron microscopy and spectroscopy to study a $NdNiO_3$ film grown by layer-by-layer molecular beam epitaxy (MBE). We found RP faults with multiple configurations in high-angle annular dark-field images. Quantitative analysis of the variation in lattice constants indicates that large strains exist around the substrate-film interface. We demonstrate that the Ni valence change around RP faults is associated with strain and structure variation. This work provides insight into the microstructure and electronic-structure modifications around RP faults in nickelates.

In addition, interface polarity plays a vital role in the physical properties of oxide heterointerfaces, as it can cause specific modifications of the electronic and atomic structure. Reconstruction due to the strong polarity of the $NdNiO_2/SrTiO_3$ interface in recently discovered superconducting nickelate films may play an important role, since no superconductivity has been observed in the bulk. Thus, we investigated the effects of oxygen distribution, polyhedral distortion, elemental intermixing, and dimensionality in $NdNiO_2/SrTiO_3$ superlattices grown on $SrTiO_3$ (001) substrates. Oxygen distribution maps show a gradual variation of the oxygen content in the nickelate layer. Remarkably, we demonstrate a thickness-dependent interface reconstruction due to a polar discontinuity. An average cation displacement of $\sim$0.025 nm at interfaces in $8NdNiO_2/4SrTiO_3$ superlattices is twice as large as that in $4NdNiO_2/2SrTiO_3$ superlattices.

Furthermore, the polarity of a surface can also affect the electronic and structural properties of oxide thin films through electrostatic effects. Understanding the mechanism behind these effects requires knowledge of the atomic structure and electrostatic characteristics at the surface. We used annular bright-field (ABF) imaging to investigate the surface structure of a $Pr_{0.8}Sr_{0.2}NiO_{2+x}$ ($0 < x < 1$) film. We observed a polar distortion coupled with octahedral rotations in a fully oxidized $Pr_{0.8}Sr_{0.2}NiO_3$ sample and a stronger polar distortion in a partially reduced sample. Its spatial depth is about three unit cells from the surface. Additionally, we used 4D-STEM to directly image the local atomic electric field surrounding Ni atoms near the surface and discovered distinct valence variations of Ni atoms, which were confirmed by EELS. Our results suggest that the strong surface reconstruction in the reduced sample is closely related to the formation of oxygen vacancies by topochemical reduction. Benefited from the advantages of 4D-STEM and STEM-EELS, this thesis presents the detailed studies of the atomic structure and electrostatic characteristic at defects, interfaces, surfaces, and grain boundaries in complex oxides, providing insights into understanding the mechanism of the physical behaviors at the atomic scale.

KURZFASSUNG

Komplexe Oxide zeigen eine breite Palette faszinierender physikalischer Eigenschaften, die sich aus komplexen atomaren Anordnungen und komplexen elektronischen Wechselwirkungen ergeben. Eine präzise Charakterisierung der atomaren Struktur und elektrostatischen Eigenschaften dieser Materialien ist entscheidend, um ihre funktionellen Eigenschaften aufzuklären und die Entwicklung neuartiger Bauelemente zu ermöglichen. In dieser Studie verwenden wir neueste Elektronenmikroskopie-Techniken, insbesondere die 4-dimensionale Raster-Transmissionselektronenmikroskopie (4D-STEM) und die Elektronenenergieverlustspektroskopie (EELS), um die atomare Struktur und die elektrostatischen Eigenschaften von komplexen Oxiden zu untersuchen.

Die 4D-STEM-Technik ermöglicht die Erfassung vielfältiger Informationen aus Elektronenbeugungsmustern, die eine präzise Aufzeichnung von Atompositionen und die Analyse komplexer Elektronenwechselwirkungen innerhalb des Kristallgitters ermöglichen. Hochauflösende Abbildungen der atomaren Struktur können rekonstruiert werden, um Defekte, Grenzflächen und subtile strukturelle Verzerrungen in den komplexen Oxiden zu identifizieren. Das elektrostatische Feld oder die Ladungsverteilung innerhalb einer dünnen Probe können durch Berechnung des Impulsübertrags des Elektronenstrahls extrahiert werden. Durch die Kombination von 4D-STEM mit STEM-EELS erhält man ein umfassendes Verständnis der lokalen atomaren und elektronischen Struktur sowie der Ladungsverteilung und ihrer Wechselwirkungen in ausgewählten Bereichen in komplexen Oxiden, wie Defekte, Grenzflächen, Oberflächen und Korngrenzen.

In dieser Arbeit haben wir zunächst die atomare Struktur und elektrostatische Eigenschaften an der Korngrenze (GB) in einem $SrTiO_3$-Bikristall untersucht. Wir zeigen, dass die Σ5-GB reich an Ti und verarmt an Sr ist. Wir untersuchen mögliche Auswirkungen auf die Variation des atomaren elektrostatischen Feldes, einschließlich Sauerstoffleerstellen, Änderungen in der Ti-Valenz und Ansammlung von Kationen. Eine negative Ladung, die aus einer Raumladungszone in $SrTiO_3$ resultiert, kompensiert eine positive Ladung, die an der GB akkumuliert wird, was mit dem Modell der doppelten Schottky-Barriere übereinstimmt. Dies zeigt, dass elektrostatische Eigenschaften im Nanometer-Maßstab durch 4D-STEM charakterisiert werden können, was umfassende Einblicke in die GB-Struktur und deren Auswirkungen auf die elektrostatischen Eigenschaften ermöglicht.

Wir haben weiterhin die atomaren Strukturen und elektrostatischen Eigenschaften in den spezifischen Bereichen um Ruddlesden-Popper-Fehlern in einem $NdNiO_3$-Film, den Grenzflächen zwischen $SrTiO_3$ und $NdNiO_2$ und der Oberfläche der teilweise reduzierten Nickelat-Filme untersucht. Das $NdNiO_3$-System hat aufgrund der Entdeckung der Supraleitfähigkeit in $Nd_{0.8}Sr_{0.2}NiO_2$ viel Aufmerksamkeit erregt. In Seltenerd-Nickelaten spielen Ruddlesden-Popper-Fehler eine wichtige Rolle für die funktionellen Eigenschaften, was uns dazu motiviert hat, die mikrostrukturellen Merkmale und die elektronische Struktur zu untersuchen. Dazu haben wir aberrationskorrigierte Rastertransmissionselektronenmikroskopie und -spektroskopie verwendet, um einen durch Molekularstrahlepitaxie (MBE) hergestellten $NdNiO_3$-Film zu untersuchen. Wir fanden RP-Fehler mit mehreren Konfigurationen in HAADF-(high-angle annular dark-field) Aufnahmen. Die quantitative Analyse der Variation der Gitterkonstanten deutet darauf hin, dass große Dehnungen um die Substrat-Film-Grenzfläche bestehen. Wir zeigen, dass die Änderung der Ni-Valenz um RP-Fehler mit einer

Dehnung und Strukturveränderung zusammenhängt. Diese Arbeit liefert Einblicke in die Mikrostruktur und die Modifikationen der elektronischen Struktur um RP-Fehler in Nickelaten.

Darüber hinaus spielt die Polarität der Grenzfläche eine wichtige Rolle für die physikalischen Eigenschaften von Oxid-Heterogrenzflächen, da sie spezifische Modifikationen der elektronischen und atomaren Struktur verursachen kann. Die Rekonstruktion aufgrund der starken Polarität der $NdNiO_2/SrTiO_3$-Grenzfläche in kürzlich entdeckten supraleitenden Nickelatfilmen könnte eine wichtige Rolle spielen, da im Volumenmaterial keine Supraleitung beobachtet wurde. Daher haben wir die Auswirkungen der Sauerstoffverteilung, der polyedrischen Verzerrung, der chemischen Vermischung und der Dimensionalität in $NdNiO_2/SrTiO_3$-Übergittern untersucht, die auf $SrTiO_3$ (001)-Substraten gewachsen sind. Die Bilder der Sauerstoffverteilung zeigen eine graduelle Variation des Sauerstoffgehalts in der Nickelatschicht. Bemerkenswert ist, dass wir eine dickeabhängige Rekonstruktion der Grenzfläche aufgrund einer polaren Diskontinuität nachweisen können. Die durchschnittliche Verschiebung der Kationen von ~0,025 nm an den Grenzflächen in $8NdNiO_2/4SrTiO_3$-Übergittern ist doppelt so groß wie in $4NdNiO_2/2SrTiO_3$-Übergittern.

Darüber hinaus kann auch die Polarität einer Oberfläche die elektronischen und strukturellen Eigenschaften von Oxid-Dünnschichten durch elektrostatische Effekte beeinflussen. Um den Mechanismus hinter diesen Effekten zu verstehen, sind Kenntnisse über die atomare Struktur und die elektrostatischen Eigenschaften an der Oberfläche erforderlich. Wir haben die Oberflächenstruktur eines $Pr_{0.8}Sr_{0.2}NiO_{2+x}$ ($0 < x < 1$)-Films mit Hilfe von ABF-(annular bright-field) Abbildungen untersucht. Wir haben eine polare Verzerrung in Verbindung mit Oktaeder-Rotationen in einer vollständig oxidierten $Pr_{0.8}Sr_{0.2}NiO_3$-Probe und eine stärkere polare Verzerrung in einer teilweise reduzierten Probe beobachtet. Ihre räumliche Ausdehnung beträgt etwa drei Elementarellen von der Oberfläche aus. Darüber hinaus haben wir mit 4D-STEM das lokale atomare elektrische Feld um die Ni-Atome in der Nähe der Oberfläche direkt abgebildet und deutliche Valenzvariationen der Ni-Atome entdeckt, die durch EELS bestätigt wurden. Unsere Ergebnisse legen nahe, dass die starke Oberflächenrekonstruktion in der reduzierten Probe eng mit der Bildung von Sauerstoffleerstellen durch die topotaktische Reduktion zusammenhängt. Dank der Vorteile von 4D-STEM und STEM-EELS präsentiert diese Arbeit detaillierte Studien zur atomaren Struktur und elektrostatischen Eigenschaften von Defekten, Grenzflächen, Oberflächen und Korngrenzen in komplexen Oxiden und liefert Einblicke in den Mechanismus des physikalischen Verhaltens auf atomarer Skala.

ACKNOWLEDGMENTS

I would like to express my deepest gratitude and appreciation to all those who have contributed to the completion of this thesis.

First and foremost, I owe my deepest gratitude to my supervisor Prof. Dr. Peter A. van Aken who brought me into the wonderland of electron microscopy. Without his unwavering support, mentorship, patience, and encouragement, I would not have been able to complete my studies. His expertise, constructive feedback, and constant encouragement have been instrumental in shaping this thesis. I am truly grateful for his guidance and for pushing me to explore new ideas and approaches. I am also grateful for his guidance in scientific writing, refining experimental results, and providing numerous opportunities to attend international conferences.

I am very grateful to Prof. Dr. Wang Yi for his consistent guidance during the first two years of my Ph.D. studies. When I started to learn the new 4D-STEM technique, which requires a solid understanding of programming and theory in STEM, his guidance proved to be very helpful. He generously shared his expertise in STEM-related techniques and provided me with his DM scripts. Under his guidance, I gradually familiarized myself with Python coding and mastered this technique step by step. In addition, I would like to express my sincere appreciation to my day-to-day supervisor, Dr. Wilfried Sigle, for his invaluable insights and guidance. Wilfried spent a considerable amount of time refining my manuscripts, reports, and dissertations, transforming them from unorganized compositions to their final polished form. I am truly grateful for their guidance and timely assistance. It has been an immense privilege and a great blessing to work with and learn from them. I would also like to thank Dr. Hongguang Wang for his insightful discussion of my papers, generous help with the EELS analysis, and sharing his experience in scientific writing.

I would like to thank our wonderful collaborators for their indispensable contributions. I have been fortunate to collaborate with colleagues, Prof. Bernhard Keimer, Dr. Eva Benckiser, and the people in their group, Dr. Roberto Ortiz, and Rebecca Pons, from the Max Planck Institute for Solid State Research. I sincerely thank Dr. Roberto Ortiz for growing wonderful $NdNiO_2/SrTiO_3$ superlattice samples; Rebecca Pons for growing beautiful $Pr_{0.8}Sr_{0.2}NiO_{2+x}$, and $PrNiO_{2+x}$ single crystal films. I am grateful to Dr. Eva Benckiser for fruitful discussions, and many insights into my work. I would also like to thank Dr. Gennady Logvenov for allowing me to work with members of his thin film technology group. Thanks to Rebecca Pons for teaching me how to use the MBE and grow samples. Thanks to Dr. Georg Cristiani, and Nico Bonmassar for their help with the MBE.

I am deeply indebted to many kind and warm-hearted people in the StEM group. I am grateful to Caroline Heer for her warm care and help since the day I arrived in Stuttgart, Germany. I am deeply grateful to Kersten Hahn and Peter Kopold for teaching me the techniques of electron microscopy. I appreciate that Ute Salzberger and Dr. Julia Deuschle for teaching me sample preparation techniques. I thank Dr. Tobias Heil for developing the exceptional software used for data acquisition. I would also like to thank Dr. Vesna Srot for her help with the TEM. I am grateful for the support of Marion Kelsch in nano-milling, and Birgit Bussmann in operating the ultramicrotomy. Thanks to the members of the StEM group, Dr. Kenan Elibol, Xuejiao Zhang, Dr. Xu Chen, Dr. Robin Lingstädt, Nicolas Bonmassar,

Dr. Yu-Mi Wu, Anna Scheid, Felicitas Predel, Dr. Eren Suyolcu, Dr. Nilesh Vats, Dr. Surong Guo, Dr. Devendra Negi, Pablo Sosa Lizama, Levon Kalaydjian for the pleasant and relaxing time together.

Last but not the least, I would like to thank my family for their open-mindedness, understanding, trust and support from the bottom of my heart.

BIOGRAPHICAL NOTE

EDUCATION

Ph.D.	Max Planck Institute for Solid State Research (MPI-FKF) Technical University of Darmstadt (TUD)	2019–2023
	Material Science	*Supervised by*, Prof. Dr. Peter A. van Aken
M.Sc.	Southwest University of Science and Technology	2015–2018
	Materials Science and Engineering	*Supervised by*, Prof. Dr. Xianhua Wei
B.Eng.	Southwest University of Science and Technology	2011–2015
	Materials Science and Engineering	*Supervised by*, Prof. Dr. Min Zeng

LIST OF PUBLICATIONS

Publications Related to the Present Thesis:

A. **Chao Yang**, Yi Wang, Wilfried Sigle, and Peter A. van Aken. "Determination of Grain-Boundary Structure and Electrostatic Characteristics in a $SrTiO_3$ Bicrystal by Four-Dimensional Electron Microscopy." *Nano Letters* 21, 21 (2021): 9138-9145.

B. **Chao Yang**, Yi Wang, Daniel Putzky, Wilfried Sigle, Hongguang Wang, Roberto A. Ortiz, Gennady Logvenov, Eva Benckiser, Bernhard Keimer, and Peter A. van Aken. "Ruddlesden–Popper Faults in $NdNiO_3$ Thin Films." *Symmetry* 14, 3 (2022): 464.

C. **Chao Yang**, Roberto Ortiz, Yi Wang, Daniel Putzky, Eva Benckiser, Bernhard Keimer, and Peter A. van Aken. "Generation of Ruddlesden-Popper faults in Sr doped $NdNiO_3$." *Microscopy and Microanalysis* 27, S1 (2021): 1198-1200.

D. **Chao Yang**, Yi Wang, Wilfried Sigle, and Peter A. van Aken. "Probing Grain-boundary Structure and Electrostatic Characteristics in a $SrTiO_3$ Bi-crystal by 4D-STEM." *Microscopy and Microanalysis* 28, S1 (2022): 592-594.

E. **Chao Yang**, Roberto A. Ortiz, Yi Wang, Wilfried Sigle, Hongguang Wang, Eva Benckiser, Bernhard Keimer, and Peter A. van Aken. "Thickness-Dependent Interface Polarity in Infinite-Layer Nickelate Superlattices." *Nano Letters*, 23 (2023): 3291-3297.

F. **Chao Yang**, Roberto A Ortiz, Yi Wang, Wilfried Sigle, Hongguang Wang, Eva Benckiser, Bernhard Keimer, Peter A van Aken. "Atomic Insights of Interface Polarity in $NdNiO_2/SrTiO_3$ Superlattices." *Microscopy and Microanalysis* 29, S1 (2023): 321-322.

Other Publications:

A. Bingjie Zhong, Chengyang Zuo, **Chao Yang**, Shilin Yang, Yun Li, Hongtao Yu, and Xianhua Wei. "Bifunctional europium doped $SrTiO_3$ ceramics with energy storage and photoluminescence." *Journal of Alloys and Compounds* 901 (2022): 163556.

B. Bingjie Zhong, Zhongmin Long, **Chao Yang**, Yun Li, and Xianhua Wei. "Colossal dielectric permittivity in co-doping $SrTiO_3$ ceramics by Nb and Mg." *Ceramics International* 46, 12 (2020): 20565-20569.

C. **Chao Yang**, Bingjie Zhong, Zhongmin Long, and Xianhua Wei. "The effect of sintering atmosphere on colossal permittivity in W+Mg/Al co-doped TiO_2 ceramics." *Ceramics International* 46, 3 (2020): 3420-3425.

D. Yanbin Wang, Wenjing Jie, **Chao Yang**, Xianhua Wei, and Jianhua Hao. "Colossal permittivity materials as superior dielectrics for diverse applications." *Advanced Functional Materials* 29, 27 (2019): 1808118.

E. **Chao Yang**, Xianhua Wei, and Jianhua Hao. "Disappearance and recovery of colossal permittivity in (Nb+ Mn) co-doped TiO_2." *Ceramics International* 44, 11 (2018): 12395-12400.

F. **Chao Yang**, Xianhua Wei, and Jianhua Hao. "Colossal permittivity in TiO_2 co-doped by donor Nb and isovalent Zr." *Journal of the American Ceramic Society* 101, 1 (2018): 307-315.

G. **Chao Yang**, Mei-Yan Tse, Xianhua Wei, and Jianhua Hao. "Colossal permittivity of (Mg+Nb) co-doped TiO_2 ceramics with low dielectric loss." *Journal of Materials Chemistry C* 5, 21 (2017): 5170-5175.

Submitted manuscripts:

A. **Chao Yang**, Rebecca Pons, Wilfried Sigle, Hongguang Wang, Eva Benckiser, Gennady Logvenov, Bernhard Keimer, Peter A. van Aken. "Atomic mechanism of strong surface reconstruction in partially reduced nickelate films." *Nature Communications*, 2023, *accepted.*

CONFERENCE CONTRIBUTIONS

A. **Chao Yang**, Roberto Ortiz, Yi Wang, Daniel Putzky, Eva Benckiser, Bernhard Keimer, and Peter A. van Aken. "Generation of Ruddlesden-Popper faults in Sr doped $NdNiO_3$." **(*Oral lecture*)**, Microscopy and Microanalysis, 2021, online, USA.

B. **Chao Yang**, Yi Wang, Wilfried Sigle, and Peter A. van Aken, **(*Oral lecture*)**, International Workshop at Ringberg Castle, June 2021, Germany.

C. **Chao Yang**, Yi Wang, Wilfried Sigle, and Peter A. van Aken. "Probing Grain-boundary Structure and Electrostatic Characteristics in a $SrTiO_3$ Bi-crystal by 4D-STEM." (***Poster presentation***), Microscopy and Microanalysis, July 31-August 4, 2022, Portland, OR, USA.

D. **Chao Yang**, Roberto A. Ortiz, Yi Wang, Wilfried Sigle, Hongguang Wang, Eva Benckiser, Bernhard Keimer, Peter A. van Aken. "Thickness-dependent interface polarity in infinite-layer nickelate superlattices." (***Oral lecture***), DPG-SKM, March 26-March 31, 2023, Dresden, Germany.

E. **Chao Yang**, Rebecca Pons, Wilfried Sigle, Hongguang Wang, Eva Benckiser, Bernhard Keimer, Peter A. van Aken. "Atomic insight of the surface polarity in partially reduced nickelates." (***Poster presentation***), E-MRS, May 29-June 3, 2023, Strasburg, France.

F. **<u>Chao Yang</u>**, Roberto A Ortiz, Yi Wang, Wilfried Sigle, Hongguang Wang, Eva Benckiser, Bernhard Keimer, Peter A van Aken. "Atomic Insights of Interface Polarity in $NdNiO_2/SrTiO_3$ Superlattices" (***Poster presentation***), Microscopy and Microanalysis, July 23-August 27, 2023, Minneapolis, USA.

Table of Content

List of Figures

List of abbreviations and symbols

Abbreviations

STEM	Scanning transmission electron microscopy
ACSTEM	Aberration-corrected scanning transmission electron microscopy
4D-STEM	Four-dimensional scanning transmission electron microscopy
DPC	Differential phase-contrast
iDPC	Integrated differential phase-contrast
CoM	Center of Mass
iCoM	Integrated Center of Mass
WDD	Wigner distribution deconvolution
PACBED	Position-averaged convergent beam electron diffraction
EELS	Electron energy-loss spectroscopy
EDX	Energy-dispersive X-ray spectroscopy
SEM	Scanning electron microscope
ABF	Annular bright field
HAADF	High-angle annular dark field
IAM	Independent atom model
ASE	Atomic simulation environment
DFT	Density-functional theory
FIB	Focused Ion Beam
PCA	Principal Component Analysis
PLD	Pulsed laser deposition
MBE	Molecular-beam epitaxy
RHEED	Reflection high energy electron diffraction
QCM	Quartz crystal microbalance
ICP-OES	Inductively coupled plasma optical emission spectroscopy
CTR	Crystal truncation rods
TMOs	Transition metal oxides
2DEG	Two-dimensional electron gas
PM	Paramagnetic
AFM	Antiferromagnetic
FM	Ferromagnetic
GB	Grain boundary
RP	Ruddlesden-Popper
STO	$SrTiO_3$
NNO2	$NdNiO_2$

NNO3	$NdNiO_3$
SL	Superlattice
*RE*NiO	Rare-earth nickelate

Symbols

e – Electron Charge

m_e – Electron mass

z – Electron Charge

v – Electron velocity

t – Time

$*$ – Complex conjugate

ψ – Wave functions

$\mathcal{F}$ – Fourier transform

P – Probability

$p_\perp$ – Momentum vector

$r_\perp$ – Position vectors

e – Electron Charge

H – Hamiltonian

V – Electrostatic potential

E – Electrostatic field

I_{Beam} – Beam intensity

ε_0 – Vacuum permittivity

h – Planck's constant

λ – Wavelength

$\otimes$ – Convolution

$\Delta p_\perp$ – Momentum transfer

ρ – Charge density

φ – Phase

∇ – Divergence

C – Constant

$\star$ – Cross correlation

A – Aperture factor

Chapter 1 Introduction

Chapter 1 introduces the importance and motivation of the study of the atomic structure and electrostatic characteristics in complex oxide materials. The development of the characterization techniques of the electrostatic characteristics by electron microscopy is summarized in detail.

1.1 Motivation

Electrostatic effects are crucial for understanding the physical and chemical properties of oxide materials as they can modify atomic and electronic structures through Coulomb forces. Complex transition metal oxides (TMOs) with strongly correlated electron systems are especially influenced by the strong electrostatic interactions between the charged ions. These interactions can create localized electronic states near the Fermi level, leading to novel electronic and magnetic properties. Additionally, electrostatic interactions play a critical role in the stability and structural properties of complex oxides. The crystal structure, stability, and phase transitions of complex oxides are determined by the electrostatic forces between charged ions. For example, the ferroelectricity of some complex oxides arises from the presence of spontaneous polarization, which is caused by electrostatic interactions between charged ions in the crystal lattice. Furthermore, the electrostatic discontinuity at interfaces between different materials can result in intriguing phenomena, such as the formation of a two-dimensional electron gas (2DEG). The $LaAlO_3/SrTiO_3$ interface[1] or the surface of $KTaO_3$[2] can exhibit a 2DEG due to the rearrangement of charges and electrostatic effects, leading to the emergence of unique physical properties like superconductivity[3-5] or charge-density-wave states[2]. Additionally, symmetry breaking can play a significant role in modifying the electrostatic characteristics of materials. Symmetry breaking leads to changes in the distribution of charges and electric fields, influencing the behavior of electrons and their interactions with other charged particles. For example, in strongly correlated electron systems, the competition between different types of ordering, such as charge, orbital, and spin order, can lead to rich phase diagrams and the appearance of unconventional electronic states. Therefore, this thesis is aimed to study the effects of electrostatic characteristics on the specific structures at the atomic scale, e.g., defects, geometry, interface, surface, and grain boundary, opening up opportunities for exploring and harnessing novel functionalities and applications.

Scanning transmission electron microscopy has been developed to probe the charge, atomic and electronic structures with high precision. By using conventional STEM techniques, like HAADF, ABF, one can quantify the atomic structure on the sub-angstrom level, proving the opportunity to measure the strain, structural distortion, rotation, ordering, and so on. Combined with EELS, the atomic resolution structure and chemical composition can be further resolved. With the development of fast detectors, a developed 4D-STEM technique has been used to not only image the atomic structure with high resolution, but also directly map the electrostatic field.

In this thesis, we utilized advanced electron microscopy techniques, specifically 4D-STEM and STEM-EELS, to investigate the intricate atomic and electronic structures, as well as the electrostatic properties, within distinct regions of interest. Specifically, the focus was directed towards the grain boundary in a $SrTiO_3$ bicrystal, as well as defects, interfaces, and surfaces present in reduced nickelate single crystal films. To fabricate the reduced nickelate samples, a topotactic reduction methodology was implemented,

involving the reduction of the perovskite phase of the nickelates. The initial growth of the perovskite phase was accomplished through two techniques: PLD and MBE. These techniques were employed to ensure the synthesis of high-quality samples with well-defined crystal structures.

1.2 Transition-metal oxides

1.2.1 Atomic structure and charge distribution at grain boundaries

The investigation of the atomic structure and charge distribution at a grain boundary is a critical aspect of understanding the properties and behavior of materials. Grain boundaries are interfaces that separate distinct crystalline domains within a material. These boundaries can exhibit different atomic arrangements and introduce discontinuities in the crystal lattice, resulting in variations in the electronic and electrostatic properties. To study the atomic structure at the grain boundary, advanced electron microscopy techniques can be employed. These techniques provide the capability to image the atomic arrangement at the boundary with high precision. The atomic structure at the grain boundary can manifest itself as a variety of defects, including dislocations, stacking faults, or vacancies. These defects can distort the lattice and introduce additional charges or electronic states near the boundary. The precise nature of the atomic structure at the grain boundary strongly influences the local electronic and electrostatic properties, including charge distribution, energy levels, and conductivity. In terms of charge distribution, the presence of a grain boundary can induce localized electric fields due to the discontinuity in the atomic arrangement. This variation in charge distribution can result in the accumulation or depletion of charge near the boundary. The charge distribution at the grain boundary can significantly affect the electronic properties of the material, such as the band structure, carrier mobility, and electronic transport. Furthermore, the atomic structure and charge distribution at the grain boundary can influence the reactivity and stability of the material. Grain boundaries often serve as sites for chemical reactions or diffusion processes due to the altered atomic arrangement and charge distribution. These characteristics can affect the material's mechanical properties, such as strength, ductility, and corrosion resistance. Understanding the atomic structure and charge distribution at a grain boundary is crucial for tailoring material properties and designing materials with enhanced performance. By characterizing and controlling the atomic-scale features at grain boundaries, researchers can manipulate the electronic and electrostatic properties of materials, leading to improved functionality and performance in various applications such as electronics, catalysis, energy storage, and more.

Over the past few decades, the double-Schottky-barrier model has emerged as a significant framework for elucidating the electrical characteristics of grain boundaries in ionic solids. This model provides an explanation for the electrical behavior of grain boundaries by introducing the concept of a GB-core charge. The electric field generated by this charge is offset by a space charge that forms on both sides of the grain boundary, resulting in the electrically blocking nature of the boundary, as shown in Fig. 1.1. In this thesis, I focus on studies of the atomic structure and electrostatic properties of a Σ5 grain boundary in a $SrTiO_3$ bicrystal.

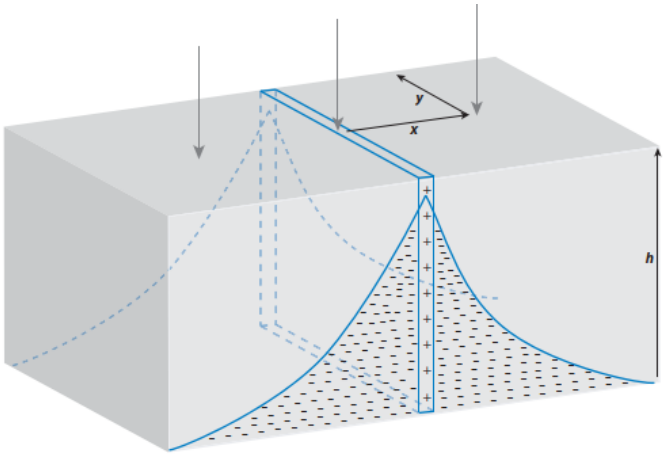

Figure 1.1 Schematic diagram of TEM specimen that contains a positively charged grain boundary and compensating space charge.[6] The gray arrows point out the beam direction. The figure is reproduced from Ref.[6]

1.2.2 Perovskite and infinite-layer nickelate heterostructures

Perovskite nickelates. The rare-earth nickelate perovskites (*RE*NiO_3) have attracted considerable attention in the field of condensed matter physics and materials science due to their intriguing physical properties, e.g., metal-insulator transitions,[7] charge ordering,[8] spin ordering,[7] magnetic ordering[9] and so on. Nickelates can be regarded as orthorhombically distorted perovskites, as the NiO_6 octahedra have obvious rotations compared to those in an ideal perovskite structure. In an ideal perovskite structure, the oxygen octahedra surrounding the central metal cation are undistorted and exhibit perfect symmetry. However, in nickelates, the NiO_6 octahedra undergo rotations, tilts, or other types of distortion. These distortions break the cubic symmetry of the crystal lattice to rhombohedral, orthorhombic, and monoclinic nickelates at different temperatures.[10-12] A tolerance factor has been used to quantify the degree of distortion or deviation from an ideal perovskite structure based on the size of the ions involved.[13] The general formula for the tolerance factor (t) can be written as

$$t = \frac{d_{RE-O}}{\sqrt{2}d_{Ni-O}}$$

where $d_{RE\text{-}O}$ is the spacing between the rare earth elements and oxygen, and $d_{Ni\text{-}O}$ indicates the spacing between Ni and O. Fig. 1.2 shows the phase diagram of the rare earth nickelates (*RE*NiO_3) as a function of temperature, the tolerance factor (t) and the Ni-O-Ni angle. Substituting different rare earths from La to Lu enable to tune the magnetic and electronic phases through a lattice distortion.

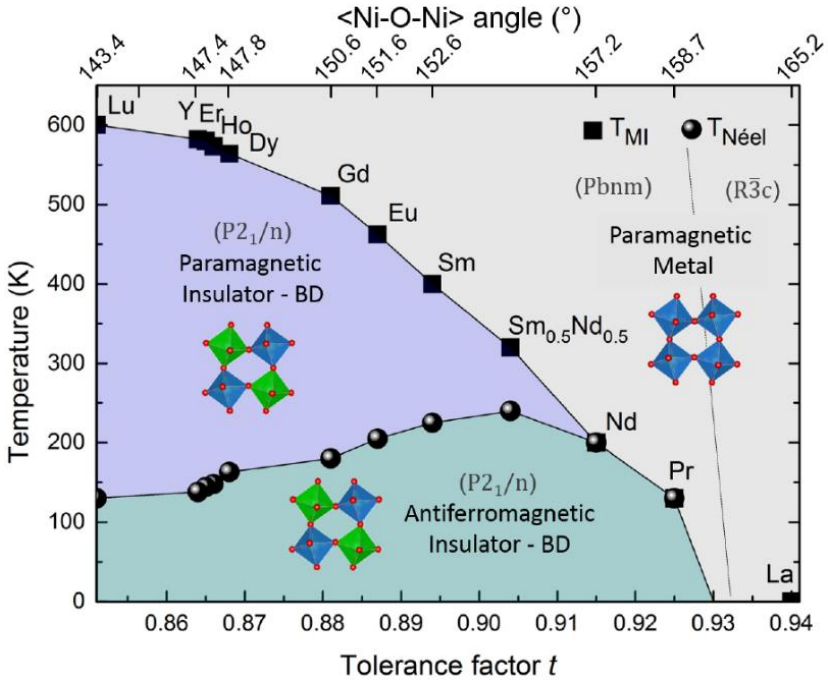

Figure 1.2 The phase diagram of bulk rare-earth nickelates consists of three regions: a paramagnetic metal (grey), a paramagnetic insulator (purple) and an antiferromagnetic insulator (green) phases as function of tolerance factor and Ni-O-Ni angle (reproduced from Ref.[14]).

The structure distortion is closely related to the electronic structure and plays a significant role in determining the properties. It can modify the bandwidth, alter the orbital overlap, induce charge localization or delocalization, and influence the strength of electronic correlations. The electronic properties of nickelates are mainly determined by the behavior of the electrons in their *d* orbitals. The *d* orbitals are involved in bonding to the oxygen atoms and in interactions with neighboring atoms or ligands. These specific arrangements of oxygen atoms around the metal ion introduce crystal field splitting. In an octahedral structure in Fig. 1.3a, the 3*d* orbital splits into two different levels e_g and t_{2g} (Fig. 1.3b). The energy level depends on the bond length of the metal ion and the six O ions.[15]

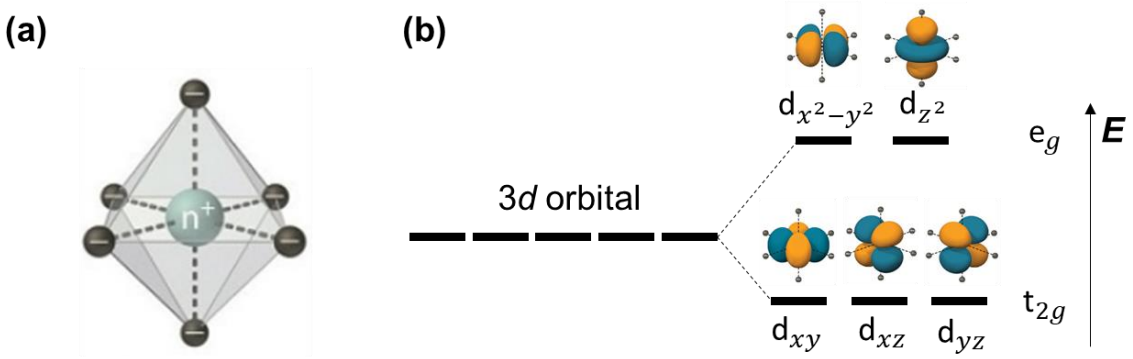

Figure 1.3 (a) An oxygen octahedral structure around a charged cation and the corresponding schematic figure (b) of the 3*d* orbital splitting (modified from the image in https://chem.libretexts.org).

In the case of perovskite nickelates with a $3d^7$ configuration, an elongated octahedral Jahn-Teller distortion also results in an orbital splitting with a lower energy of the d_{z^2} orbital compared to the $d_{x^2-y^2}$ orbital in Figure 1.4.[15] For compressed octahedra, the energy levels are reversed.

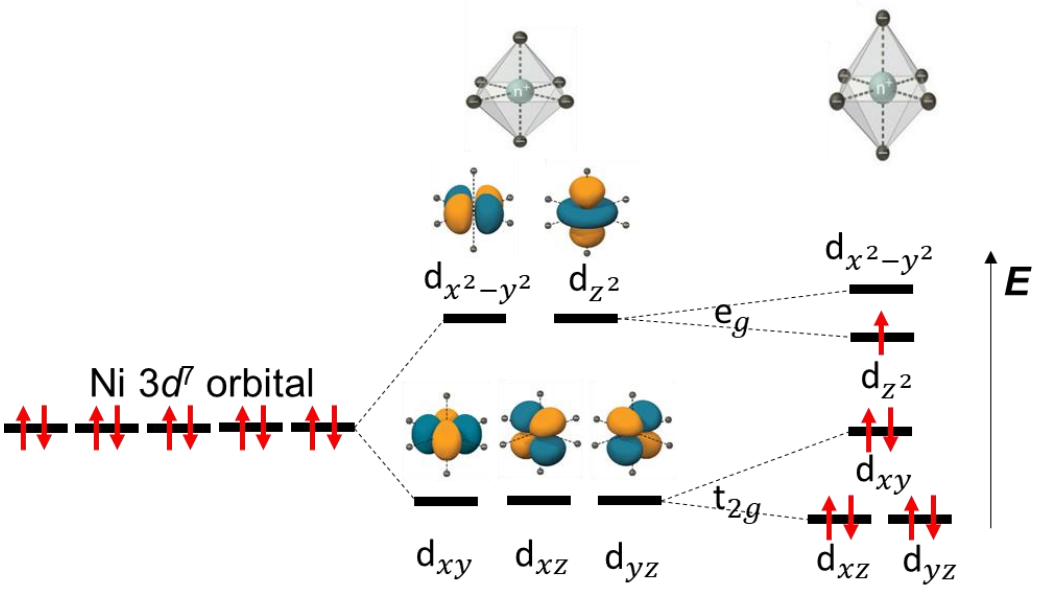

Figure 1.4 Illustration of the orbital degeneracy for a Ni $3d^7$ configuration with an elongated octahedral Jahn-Teller distortion (modified from the image at https://chem.libretexts.org).

Infinite-layer nickelate. Nickelates have a crystal structure similar to cuprates and share certain key characteristics, making them promising candidates for studying high-temperature superconductivity. Recently, superconductivity was obtained in an infinite layer $NdNiO_2$ thin film doped with Sr.[16] The apical oxygen atoms of the NiO_6 octahedra in the perovskite phase of nickelates were removed and then the infinite layer nickelate phase (see Fig. 1.5a) was obtained by a chemical reduction with CaH_2. In Fig. 1.5b, the $Nd_{0.8}Sr_{0.2}NiO_2$ sample shows superconductivity at ~9 K. However, reproducing the synthesis of superconducting nickelates has proven to be difficult due to the intricacies of oxygen deintercalation. Secondary Ruddlesden-Popper phases are easily formed during reduction (see Fig.1.5c, e). In the infinite layer nickelate phase shown in Fig. 1.5d, RP faults are still visible (see Fig.1.5e). Therefore, precise experimental techniques are required to control the oxygen content and achieve the desired doping levels in the nickelate compound while maintaining its structural integrity.[17]

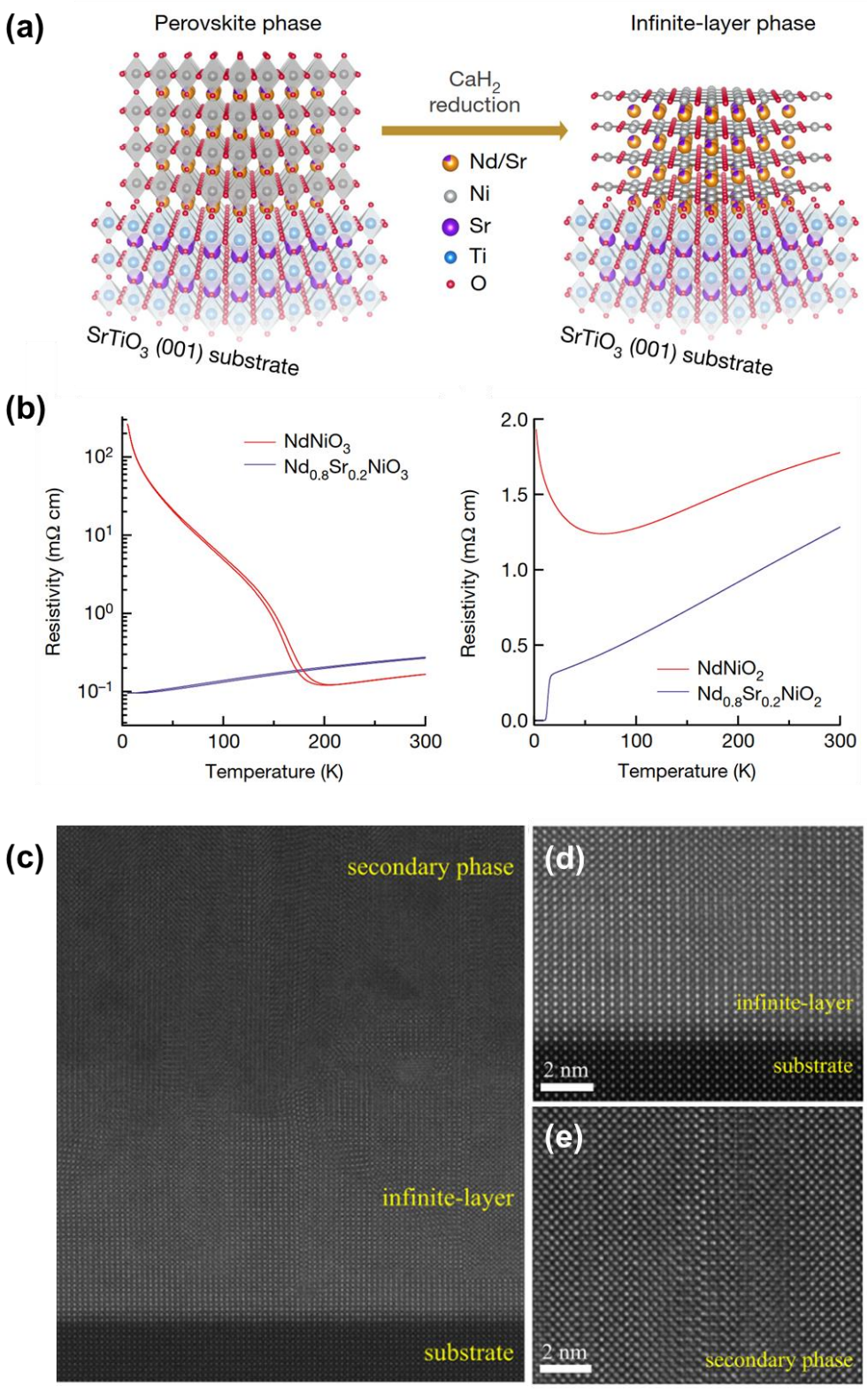

Figure 1.5 (a) Schematic structures of $Nd_{0.8}Sr_{0.2}NiO_3$ (left) and $Nd_{0.8}Sr_{0.2}NiO_2$ (right) thin films on the TiO_2-terminated single-crystal $SrTiO_3$ (001) substrate. (b) Resistivity as a function of temperature of the pristine $NdNiO_3$ and $Nd_{0.8}Sr_{0.2}NiO_3$ films and reduced $NdNiO_2$ and $Nd_{0.8}Sr_{0.2}NiO_2$ films. (c) HAADF image of the mixed-phase film after reduction. (d) Magnified image of the infinite-layer region. (e) Magnified image of the secondary phase region. Figures have been reproduced from Ref.[16-17]

As there is no superconductivity in bulk nickelates,[18] the RP structure, interface effects, and geometry effects attract increasing attention. Interestingly, superconductivity has also been obtained in a reduced RP $Nd_6Ni_5O_{12}$ film. In the square planar structure of nickelates, superconductivity is achieved in a Ni $3d^{8.8}$ configuration (see Fig. 1.6a, f) in the $Nd_6Ni_5O_{12}$ film, similar to the Sr-doped infinite-layer structure. A clear rock-salt layer is visible from the schematic structure of the RP phase and the corresponding HAADF images. The ABF image shows the square planar structure, while we can still observe residual apical oxygen. Additionally, the oxygen substructure is expected to be distorted at the RP fault plane due to an electrostatic discontinuity.[19] The role of the oxygen sub-structure at the fault plane and how it correlates with the infinite layer phase is not clear yet. In terms of interface effects, a strong polar discontinuity occurs at the interface with a connection of a $[Nd]^{3+}$-terminated infinite layer and a $[TiO_2]^0$-terminated STO substrate, causing the emergence of a 2DEG at the interface from DFT calculations.[20-21] The strong polarity at the interface could drive atomic and electronic reconstructions, leading to a rearrangement of atoms and a redistribution of electrons at the interface.[22] A similar reconstruction also occurs at polar surfaces. Since oxygen deintercalation is not homogeneous, it is important to control the exact stoichiometry in the film to reproduce nickelate superconductors. The dependence of the oxygen deficiency in nickelates has a significant effect on the structural geometry, leading to changes in the electronic and magnetic behaviors. For example, different arrangements of oxygen vacancy ordering can occur in oxygen-deficient nickelates, as suggested by the DFT calculations depicted in Fig.1.7. Bulk $LaNiO_3$ exhibits a rhombohedral structure characterized by NiO_6 octahedra. However, as the oxygen concentration decreases, structures such as NiO_5 pyramids and NiO_4 square planar arrangements are formed. In particular, in the case of $LaNiO_{2.75}$, five configurations have been proposed by DFT calculations.[23-24] Fig. 1.7(b) and (c) show the configurations of NiO_6 octahedra and NiO_4 square planar arrangements. Fig. 1.7(d), (e) and (f) display the configurations of NiO_5 pyramids and NiO_4 square planar arrangements, existing disordered and ordered oxygen vacancies. More NiO_4 square planar and less NiO_6 octahedra coexist in $LaNiO_{2.5}$ compared to that in $LaNiO_{2.75}$. A brownmillerite structure consisting of NiO_6 octahedra and NiO_5 pyramids is another possible configuration, similar to the brownmillerite phase of $CaCoO_{2.5}$.[25] Although $LaNiO_3$ is known to exhibit paramagnetism (PM) at all temperatures, some controversial experimental evidence has indicated the presence of antiferromagnetic (AFM) order in $LaNiO_3$. It has been proposed that the AFM behavior in $LaNiO_3$ is due to the presence of a small amount of oxygen vacancies. As the oxygen vacancy level further increases, $LaNiO_{2.5}$ shows AFM behavior below 152 K, whereas $LaNiO_{2.75}$ shows ferromagnetic (FM) structure below 225 K. On the other hand, $LaNiO_2$ shows no clear evidence of long-range magnetic order.

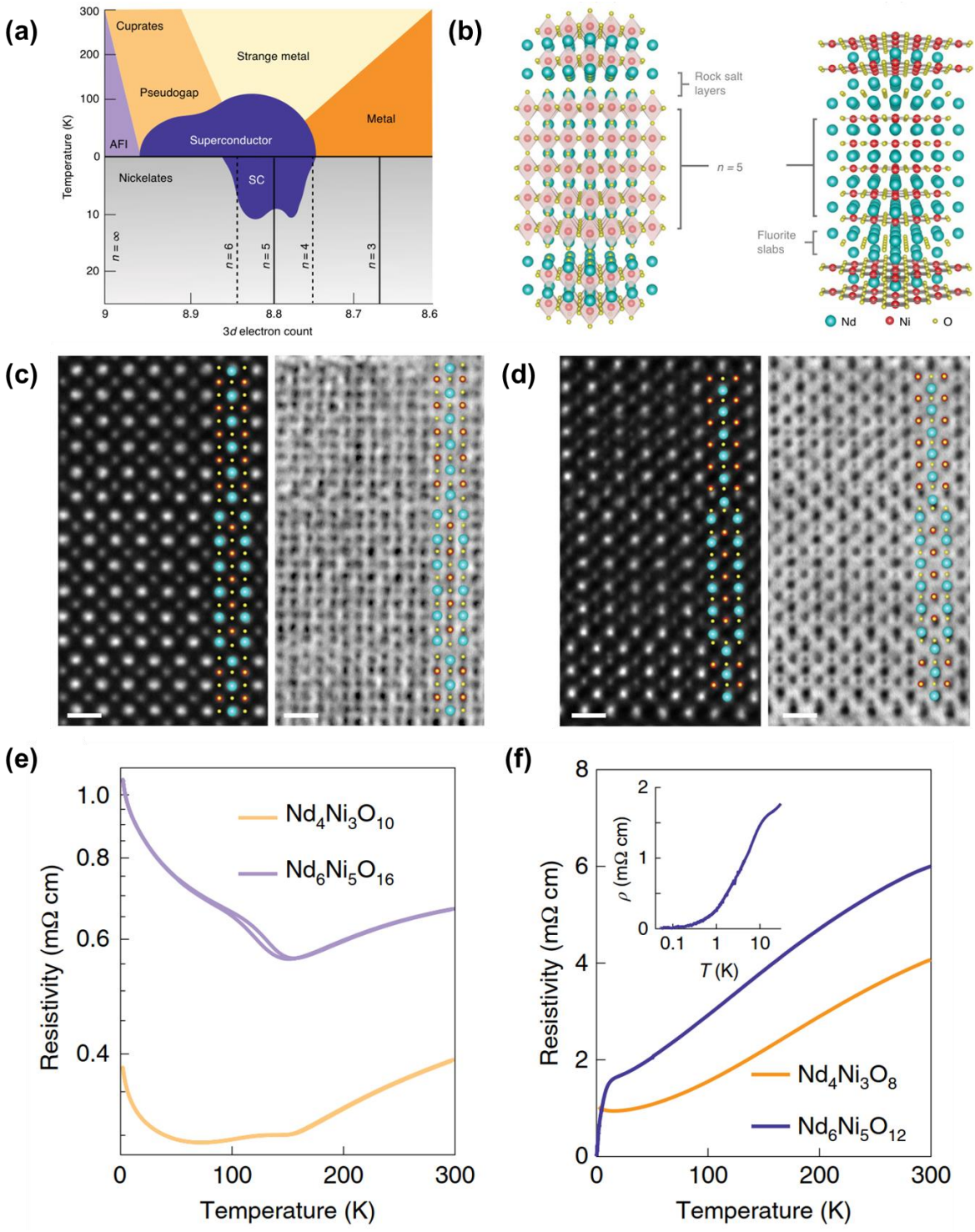

Figure 1.6 (a) Phase diagram for the electronic phases of the cuprates (top) and nickelates (bottom). (b) Crystal structures of $Nd_6Ni_5O_{16}$ RP phase (left) and $Nd_6Ni_5O_{12}$ reduced square-planar phase (right). HAADF and ABF images of (c) RP phase and (d) square-planar phase. (e) Resistivity for the $Nd_4Ni_3O_{10}$ and $Nd_6Ni_5O_{16}$ RP compounds. (f) Resistivity for the $Nd_4Ni_3O_8$ and $Nd_6Ni_5O_{12}$ square-planar phases. This figure is reproduced from Ref.[26].

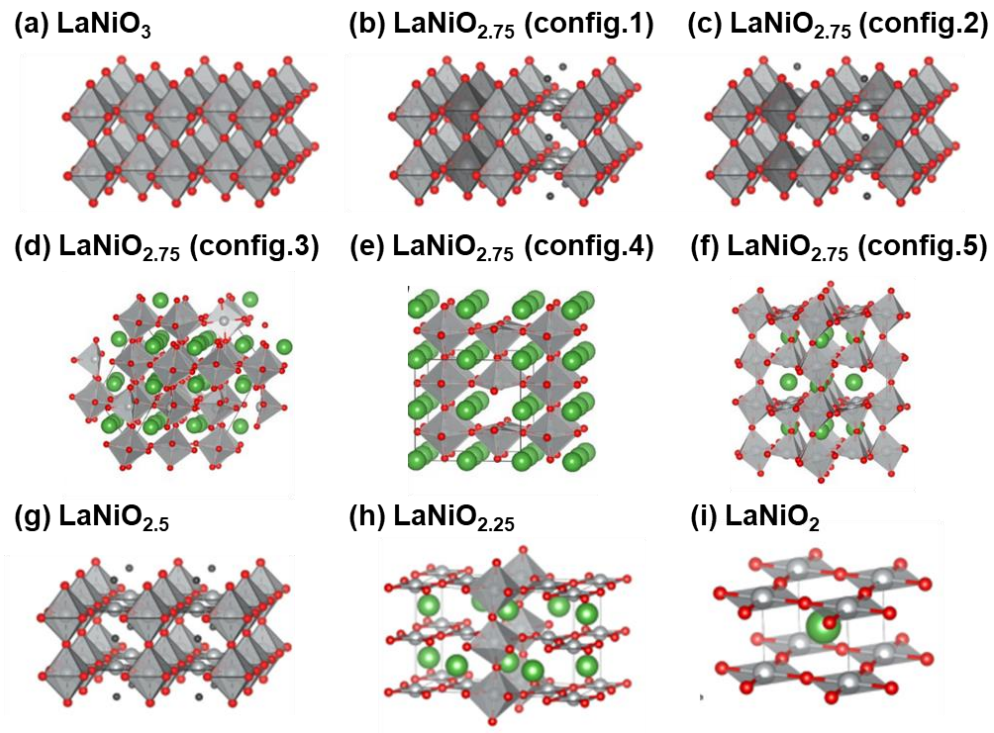

Figure 1.7 Crystal structures of (a) $LaNiO_3$, (b) $LaNiO_{2.75}$ (configuration 1), (c) $LaNiO_{2.75}$ (configuration 2), (d) $LaNiO_{2.75}$ (configuration 3), (e) $LaNiO_{2.75}$ (configuration 4), (f) $LaNiO_{2.75}$ (configuration 5), (g) $LaNiO_{2.5}$, (h) $LaNiO_{2.25}$, and (i) $LaNiO_2$. Figures are reproduced from Ref.[23-24].

The multiple configurations of Ni and ligand bonding result in different electronic configurations. In a pyramidal nickelate (Ni $3d^8$), the electronic configuration is shown in Figure 1.8b. In a square planar nickelate (Ni $3d^9$), the electrons of the ligands are only attracted to the *xy* planes, where the corresponding energy level of the orbitals is higher in the *xy* planes, as shown in Fig. 1.8d. Therefore, an accurate determination of the atomic structure is essential to elucidate the mechanism of electronic and magnetic behaviors in nickelates and to provide guidance for their control. The interface, surface, and geometry of the film are discussed in Chapters 5 and 6.

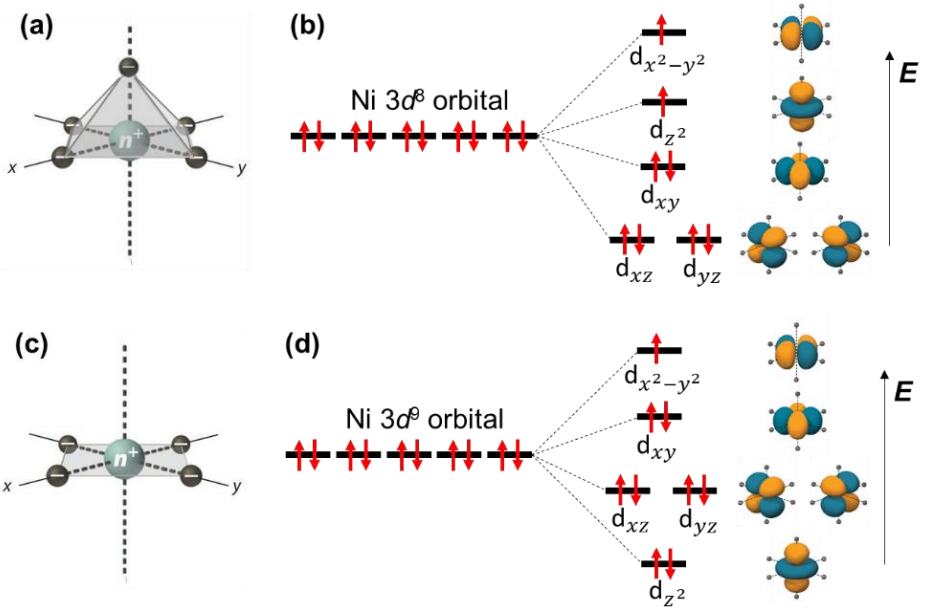

Figure 1.8 (a) A pyramidal structure and (b) the corresponding orbital degeneracy for the Ni $3d^8$ configuration. (c) A square planar structure and (d) the corresponding orbital degeneracy for the Ni $3d^9$ configuration (modified from the image at https://chem.libretexts.org).

1.3 Outline

This thesis, consisting of seven chapters, is dedicated to the investigation of the atomic structure and electrostatic characteristics in complex oxide materials using aberration-corrected 4D-STEM and spectroscopy. Chapter 1 serves as an introduction, providing the motivation for the research and outlining the topics that will be investigated throughout the thesis. Chapter 2 provides a comprehensive overview of the experimental methods used in this thesis. It begins with a brief introduction to the epitaxial growth process used for oxide heterostructures. Following the introduction to epitaxial growth, this chapter continues with a discussion of the microscopy techniques employed throughout the thesis, with a particular focus on 4D-STEM and EELS. The section dedicated to 4D-STEM and EELS covers their underlying principles, instrumentation, data processing, simulations, and the specific techniques used in the research. Chapter 3 focuses on the application of electrostatic field mapping using the 4D-STEM technique. This chapter explores the importance of characterizing and understanding the electrostatic fields present in a grain boundary. The 4D-STEM technique, with its high spatial resolution and sensitivity, allows the mapping and visualization of the charge distribution at both the atomic and nanoscale. In addition, we discuss the possible problems in reconstructing the field mapping for different special requirements, which is important for the interpretation of the measured field or charge information. In Chapter 4, we study different configurations of RP defects in a NdNiO3 film under tensile stress from a $SrTiO_3$ substrate. We discuss the microstructural and electronic structure changes around the RP faults, which are influenced by the local uneven electrostatics. Chapter 5 presents a comprehensive characterization of the $NdNiO_2/SrTiO_3$ interface. We demonstrate the thickness-dependent oxygen deintercalation during topochemical reduction. The strong polar discontinuity drives the interface reconstruction, which is closely related to the interface configuration. We perform a quantitative analysis of the oxygen distribution and occupancy, highlighting the presence of residual oxygen at the interfaces, which plays a crucial role in releasing the polar discontinuity. We observe a

thickness dependent interface polarity in infinite-layer nickelate superlattices. In addition, we map the field distribution across the interfaces and present potential artifacts in the field reconstruction at the interfaces. Chapter 6 focuses on surface polarity-induced reconstruction in nickelates with different degrees of reduction. We study the structural distortions, including oxygen rotation and polar distortions, occurring at the surface of the pristine sample. Our results show a more pronounced polar distortion in the reduced samples compared to the pristine sample. In addition, we use focused ion beam (FIB) and nano-milling sample preparation techniques to prepare high-quality thin TEM samples. We directly map the atomic electrostatic field surrounding the atomic columns, which allows us to gain a comprehensive understanding of the electrostatic environment. Chapter 7 summarizes the results obtained, followed by an outlook on future directions.

Chapter 2 Experimental methodology

This chapter provides a brief overview of the sample synthesis and characterization. The films were grown by pulsed laser deposition and molecular beam epitaxy techniques. The reduced samples were synthesized by the topochemical reduction method[16-17]. In addition, advanced aberration-corrected STEM techniques, such as conventional STEM, EELS, the latest 4D-STEM, and related image reconstructions, calculations, and simulations are presented in detail.

2.1 Sample growth and preparation

2.1.1 Epitaxial growth of oxide films via pulsed laser deposition

Pulsed laser deposition is one of the most powerful techniques for growing epitaxial films and heterostructures on a substrate. Fig. 2.1a shows a sketch of a PLD system. By using a high-power pulsed laser beam to strike a target material inside a vacuum chamber, the target material is vaporized and deposited on a substrate surface to form a thin film. The focusing lens and mirrors are used to adjust the orientation and spot size of the laser beam. The vacuum and gas systems control and adjust the pressure and oxygen density in the chamber to grow oxide materials. During deposition, the target material can be rotated and the substrate heated. A variety of material targets are attached to the rotating holder for growing superlattices and heterostructures. To grow a high quality single crystal thin film by PLD, it is important to carefully control parameters such as laser fluence, gas type and pressure, termination, miscut and substrate temperature, and deposition rate. The nickelate superlattice samples investigated in this work are synthesized by the PLD system shown in Fig. 2.1b by members of the Solid State Spectroscopy group at the Max Planck Institute for Solid State Research (MPI-FKF). The growth conditions for nickelate superlattices have been well established in this group[27-29].

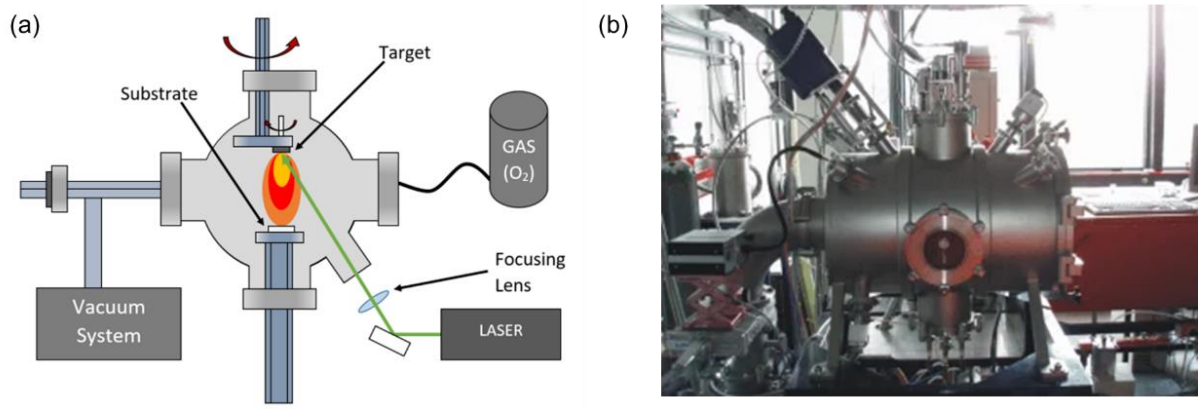

Figure 2.1 (a) Schematic diagram of a typical PLD system. (b) Photographs of the PLD system from the Scientific Facility Technology group of the Max Planck Institute for Solid State Research.

Growth of nickelate superlattices

The stoichiometric $NdNiO_3$ and $SrTiO_3$ targets were used to grow nickelate superlattices on TiO_2-terminated (001)-oriented STO substrates. Prior to each deposition, the target materials were polished to improve surface homogeneity. The substrate was cleaned with acetone in an ultrasonic sonicator for 10 min and then dried with N_2 gas. The substrate temperature is in the range of 600 and 700 ^oC, the

frequency of each pulse is 4 Hz, and the laser fluence for the growth of perovskite nickelates is ~1.6 J/cm^2. Ablation was performed with a KrF excimer laser at a wavelength of 248 nm. A shutter is used to change the target materials during superlattice growth.

2.1.2 Epitaxial growth of oxide films via molecular beam epitaxy

Molecular beam epitaxy is an epitaxy technique for growing various single crystal thin films with high precision and control. Figure 2.2a shows a sketch of an MBE tool at the Max Planck Institute for Solid State Research. The basic principle of MBE is to vaporize or sublimate individual atoms or molecules of a material from a heated source and deposit them on a substrate to form a crystalline film. The MBE system used here includes an in-situ reflection high-energy electron diffraction (RHEED) system for in-situ growth control, a quartz crystal microbalance (QCM) for measuring absolute deposition rates, an ozone delivery system for supplying ozone for oxygenation during the growth process, and an electropneumatic linear shutter for precise control of the layer-by-layer deposition process to within a small fraction of an atomic monolayer. The nickelate films were synthesized with the MBE system shown in Fig. 2.2b and Fig. 2.2c by members of the Solid State Spectroscopy group at the Max Planck Institute for Solid State Research (MPI-FKF).

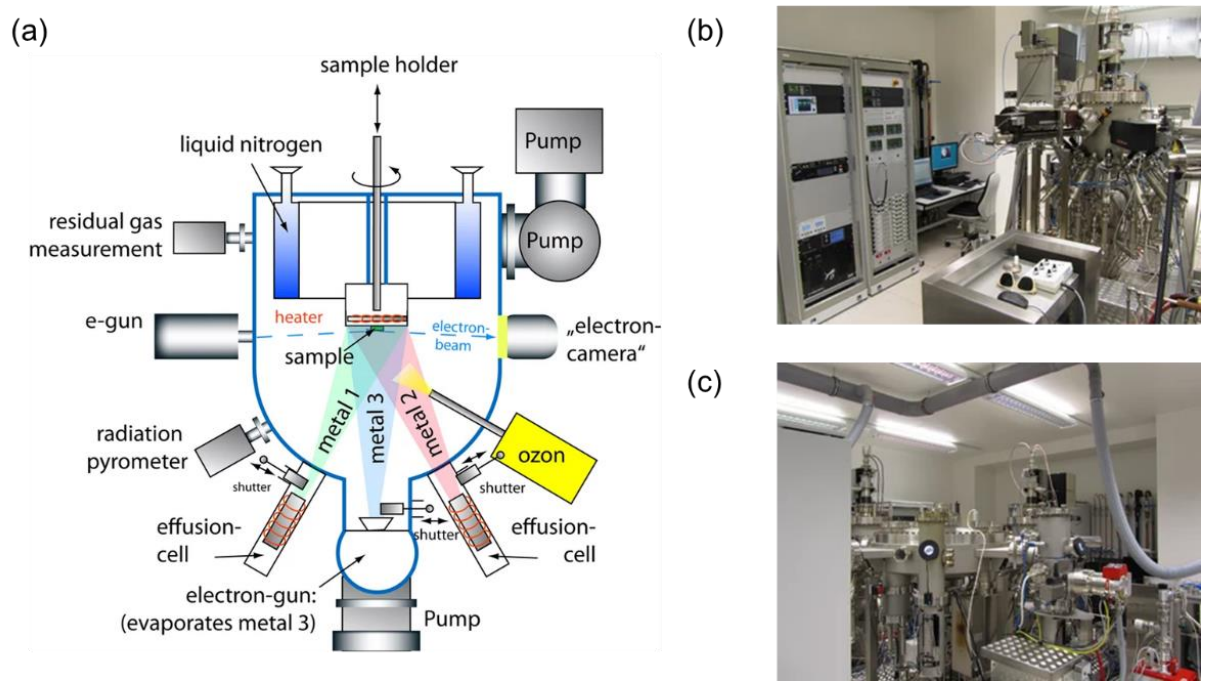

Figure 2.2 (a) Schematic of an MBE system. Photographs of (b) the oxide MBE growth chamber and (c) the storage chamber from Scientific Facility Technology group at the Max Planck Institute for Solid State Research.

Growth of $NdNiO_3$ thin films. The $NdNiO_3$ thin film was grown on TiO_2-terminated (001)-oriented STO at 630 °C in an ozone-oxygen atmosphere at a pressure of 1.8×10^{-5} Torr in an atomic layer-by-layer manner in a custom-made ozone-assisted MBE setup. It was then cooled after growth in the same atmosphere. The fluxes of the effusion cells were calibrated before growth using a quartz crystal microbalance and monitored during growth using in-situ reflection high-energy electron diffraction.

The effusion cell temperatures of the Nd and Ni sources are optimized at ~1510 °C and ~1350 °C, respectively.

Growth of $Pr_{0.8}Sr_{0.2}NiO_3$ thin films. The $Pr_{0.8}Sr_{0.2}NiO_3$ film was grown on a 1 × 1 cm^2 $NdGaO_3$ (110) single crystal at a substrate temperature of ~600°C and a pressure of 2.4 × 10^{-7} bar under ozone flow using the same MBE system used to grow the $NdNiO_3$ thin films. The effusion cell temperatures of the Pr, Ni, and Sr sources are optimized at ~1510 °C, ~1350 °C, and ~350 °C, respectively.

2.1.3 Topochemical reduction of nickelate films

Topochemical reduction has been used to synthesize new materials and has attracted much attention in oxide materials.[30-34] In this method, a precursor material is synthesized and then reduced using a chemical agent, such as calcium hydride (CaH_2), lithium hydride (LiH), lithium deuteride (LiD), and sodium hydride (NaH) or hydrogen (H_2). Topochemical reduction can be performed at relatively low temperatures, which is an advantage for synthesizing new phases. It also requires a well-defined crystal structure and good crystallinity of the precursor material to ensure a controlled and uniform reduction process. The non-stoichiometry in TMOs could lead to novel electronic and magnetic properties. For example, ordered oxygen vacancy phases in $LaCoO_{2.5}$ result in a ferromagnetic insulating state at near room temperature.[25] An insulating antiferromagnetic phase is stabilized in a $LaNiO_{2.5}$ film due to ordered oxygen vacancies.[24] In perovskite nickelates of $NdNiO_3$ and $SmNiO_3$ films, strong electron localization due to the formation of oxygen vacancies leads to a significant decrease in electrical conductivity.[35]

In our work, the oxygen deintercalation of the nickelate films was carried out via CaH_2 (an alkaline earth hydride). The reduction process is

$$RENiO_3 + CaH_2 \rightarrow RENiO_2 + CaO + H_2,$$

where Ni^{3+} is reduced to Ni^{2+}. By controlling the reduction parameters, e.g., reduction temperature, reduction time, and amount of CaH_2, different non-stoichiometric nickelate phases can be formed. As shown in the following sketch Fig. 2.3, CaH_2 powder and samples were sealed in a glass tube and separated by a small Au/Ag box to avoid direct contact. The glass tube was sealed in a glove box with an inert gas atmosphere to prevent the reactants from reacting prior to the desired reduction process.

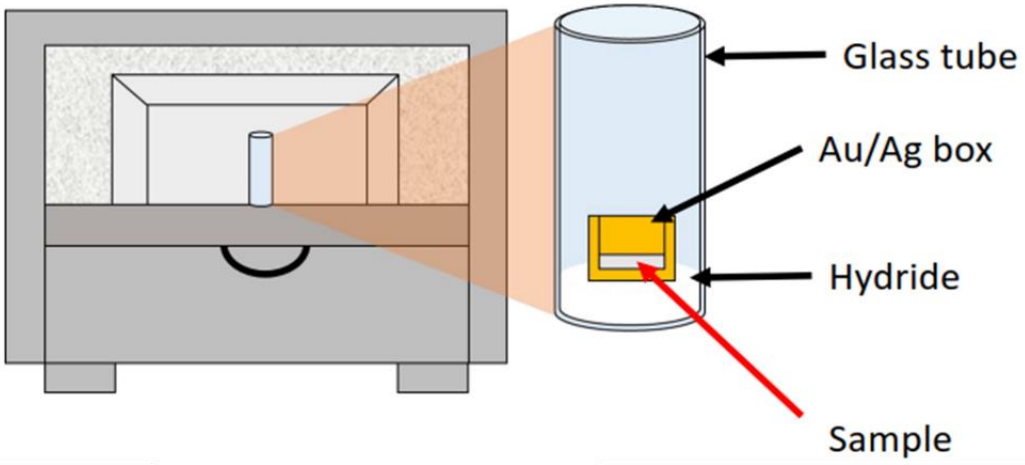

Figure 2.3 Schematic illustration of the setting of a topochemical reduction.

2.2 Characterization methodology

2.2.1 Conventional aberration-corrected scanning transmission electron microscopy

A brief introduction of STEM. Aberration-corrected scanning transmission electron microscopy has been a valuable tool in materials science and engineering for visualizing the atomic-scale structure and properties of materials for several decades. This technique can be considered as a combination of TEM and scanning electron microscopy (SEM). As shown in Figure 2.4, a spherical aberration-corrected STEM consists of an electron gun, condenser lenses, aberration corrector, objective lens, and detectors. The field emission sources or guns produce electrons, which are then converged by various condenser lenses to produce a convergent electron beam. Since spherical aberration limits the performance of the microscope, the electron beam distorted by the magnetic lens is corrected. The TEM textbooks in reference[36] provide a detailed discussion of the lens, aberrations, and correctors. In STEM mode, the convergent electron beam scans the surface of a sample, and we can construct real-space images of atoms by capturing the scattered electrons at different ranges of collection angles via detectors, such as in high-angle annular dark-field (HAADF) and annular bright-field (ABF) imaging. In addition, the measurement of energy loss by electron spectrometers is critical for the interpretation of inelastic interactions between the electron beam and the sample, e.g., phonon excitations, inter- and intra-band transitions, plasmon excitations, and inner-shell ionizations.

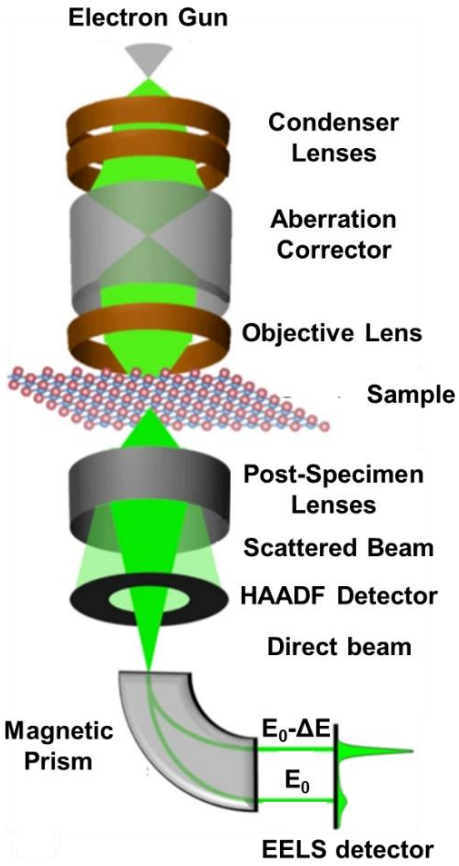

Figure 2.4 A schematic diagram of a probe-corrected STEM (Modified from the Ref.[37]).

STEM configuration used in this study. The TEM measurements in this study were performed on a JEOL JEM-ARM200F microscope equipped with a hexapole DCOR probe corrector and a Gatan GIF Quantum ERS K2 spectrometer. This state-of-the-art TEM is well suited for advanced analytical high-resolution studies of materials. The microscope can be operated at various voltages including 30 kV, 60 kV, 80 kV and 200 kV. For the characterization of oxide materials in this thesis, the STEM was set to operate at 200 kV. At this voltage, the microscope has a spatial resolution of 0.063 nm and an energy resolution of 0.3 eV. The tilt angle is limited to ± 26°. This microscope is equipped with a JEOL HAADF detector, a JEOL BF detector, a Gatan ADF detector, a Gatan BF detector, and a Merlin direct electron detector from Quantum Detector.

2.2.2 4D-STEM

Recent developments in detector technology have made it possible to acquire complete diffraction patterns in momentum space at each scanning probe position in real space. This breakthrough technique, called 4D-STEM, generates a comprehensive 4D dataset that includes the scan coordinates and diffraction patterns. Compared to traditional STEM imaging methods, 4D-STEM provides significant improvements in several imaging techniques, including virtual HAADF and ABF imaging, strain mapping, orientation mapping, field mapping, and ptychography. This chapter provides detailed information on the relevant methods used in our studies. Fig. 2.5 illustrates the signal detection process using conventional STEM and pixelated detectors. The conventional ADF and BF detectors capture electrons in a fixed angular range and record only a single value per probe position, while pixelated

detectors can capture all electrons passing through the sample with up to 256 × 256 values per probe position. The collection angles of HAADF and ABF imaging are in the range of 83-205 mrad and 10-20 mrad, respectively, for a 20.4 mrad electron beam.

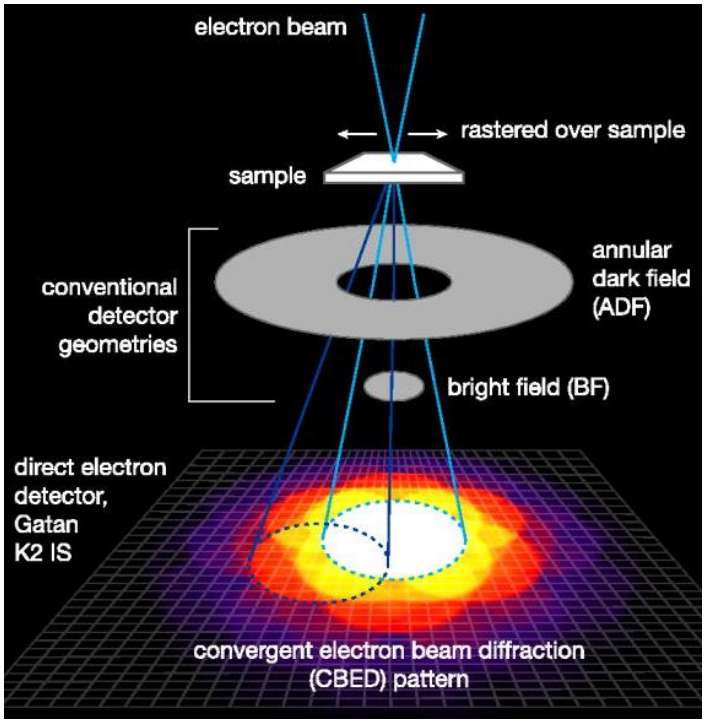

Figure 2.5 A schematic diagram of conventional STEM and 4D-STEM. (Reproduced from the Ref.[38]).

2.2.2.1 Virtual detectors for imaging

Virtual detectors are a powerful and innovative technique used in 4D-STEM imaging that allows the simulation of the imaging process for a specific detector without the need to physically modify the detector. This method allows users to extract a specific range of signals from a 4D dataset by applying a variety of geometric masks to the data that would be impractical to physically fabricate. A common application of virtual detectors is virtual selected area diffraction imaging, where the diffraction images obtained from multiple selected real-space probe positions in the 4D dataset are summed. Another application is similar to physical annular detectors, where the intensity of a subset of pixels in the 4D-dataset is summed and the resulting value is assigned to the corresponding scan coordinate in real space. Figure 2.6 shows an example of the use of virtual annular detectors. Figure 2.6a shows a position-averaged convergent beam electron diffraction (PACBED) pattern. The signal within the area of the direct electron beam can be selected for BF imaging. The signal selected from the annular regions inside and outside the beam are used for ADF and ABF imaging, respectively. This method of selecting signals in specific annular regions allows different types of information to be extracted from the sample under investigation. Specifically, BF imaging highlights the presence of defects or changes in the thickness of the sample, while ABF imaging can reveal the atomic structure of the material. ADF imaging can be used to detect heavy elements or regions with high atomic number contrast.

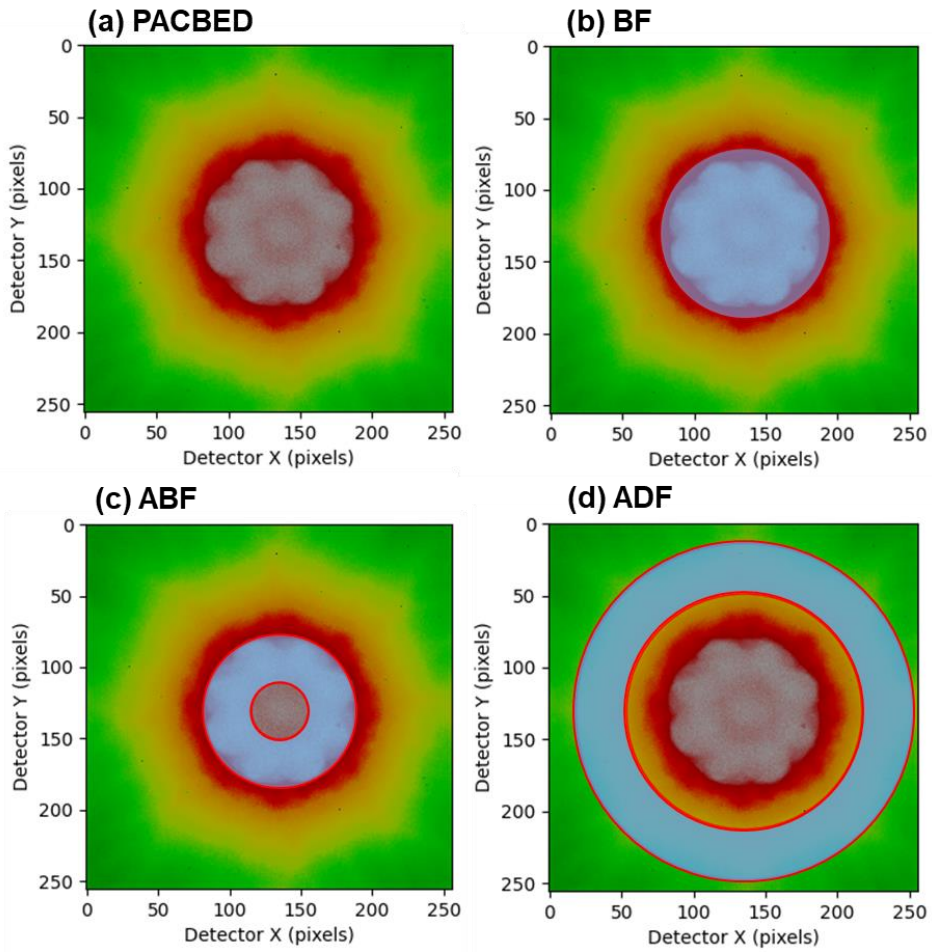

Figure 2.6 Virtual detectors used in in 4D-STEM imaging. (a) A position-averaged convergent beam electron diffraction (PACBED) pattern. (b) virtual BF detector, (c) virtual ABF detector, and (d) Virtual ADF detector applied on the PACBED pattern.

2.2.2.2 Differential phase-contrast (DPC) imaging

The incident electron beam undergoes a phase change as it interacts with the object, which creates image contrast, as in optical and X-ray microscopy. A well-known technique, differential phase contrast (DPC) imaging, was proposed to image the structure of weakly interacting phase objects. In the 1970s, the DPC detection method was also introduced into STEM by Dekkers and de Lang[39], which reduces the effect of aberrations on the generation of phase contrast compared to conventional annular detection methods. The key point is to divide the detector into two opposite segments and measure the difference of the detected signals. Figure 2.7 presents the basic principle of DPC in the diffraction plane. In a simplified situation, the electron beam B_0 passes through the object, forming a direct beam and two diffracted beams B_{-1} and B_{+1}. The opposite split detectors D_L and D_R detect the antiphase interference signals in the regions A_{-1} and A_{+1} during a scan mode. By subtracting the signals in A_{-1} and A_{+1}, their intensity modulations can be added, resulting in amplitude contrast cancellation. Theoretically, Waddell *et al*[39] proposed that the differential phase contrast images represent the gradient of the object potential (the object electromagnetic field) in the direction of the beam scan. With more effort, Chapman *et al*[40] applied the DPC method to the quantitative study of magnetic structures in a ferromagnetic film in 1978. And later, the application of DPC in STEM was mainly used to study magnetic materials at low

resolution. In 2010, Shibata *et al*[41] further developed the DPC method by using 16-segment detectors for atomic resolution imaging. Lohr et al[42] demonstrated the capability of the DPC method for nanoscale polarization electric field mapping in an InGaN quantum well. Atomic electric field mapping by DPC was followed by Shibata et al[43] in aberration-corrected STEM. To date, electric field mapping by DPC is well established.

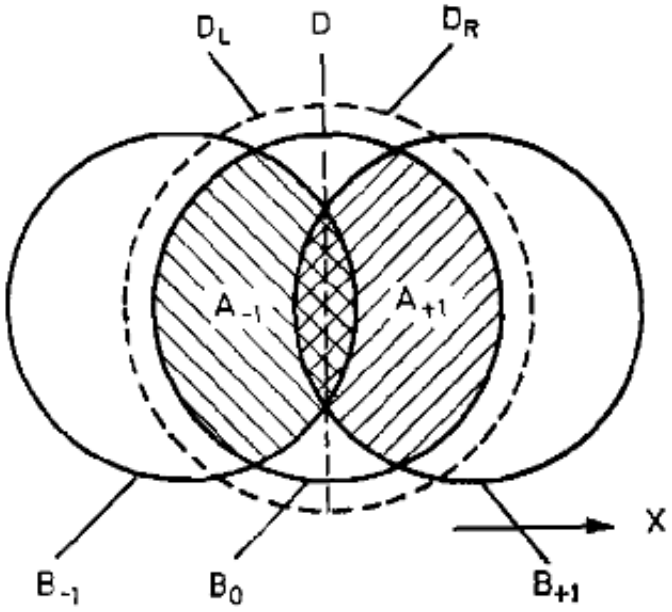

Figure 2.7 Basic principle of the DPC at the diffraction plane (Reproduced from ref.[39]).

2.2.2.3 Center-of-Mass (CoM) imaging

In 1977, Waddell *et al*[39] made a modification of the DPC method of Dekkers and de Lang and proposed the first moment detector to measure the transverse momentum of the electron beam through the specimen by calculating the center of mass of the electron beam intensity. They demonstrated the linear relationship between the phase gradient of the specimen transmission function and the momentum transfer. With the development of fast detectors, the entire electron density distribution can be recorded at the detector plane in the experiment, reigniting the discussion of CoM and DPC methods. A mathematical proof is essential to understand the imaging principle and the linear relationship between phase change and momentum transfer. In 2014, Müller *et al*[44] provided a quantum mechanical explanation for the measurement of the electrostatic field using the CoM method. In 2016, Lazić *et al*[45] also proved a similar result and presented a comprehensive analysis of the image contrast converted from the DPC and CoM methods. We briefly review both explanations here.

A quantum mechanical approach. Since the sample and diffraction planes are related by the Fourier transform, an equivalent representation is given,

$$\psi(p_\perp) \propto \mathcal{F}[\psi(r_\perp)] \tag{2.1}$$

where $\psi(r_\perp)$ is the real-space wave function and $\psi(p_\perp)$ is the momentum-space wave function. According to quantum mechanics, the probability $P(p_\perp)$ of observing the momentum operator $p_\perp$ is given by

$$P(p_\perp) = |\psi(p_\perp)|^2 \tag{2.2}$$

Then the quantum mechanical expectation value for the momentum operator $<p_\perp>$ is

$$\langle p_\perp \rangle = \int p_\perp P(p_\perp) \mathrm{d}p_\perp = \int p_\perp |\psi(p_\perp)|^2 \mathrm{d}p_\perp = \int p_\perp \psi^*(p_\perp)\psi(p_\perp) \mathrm{d}p_\perp \tag{2.3}$$

where * denotes the complex conjugate. To relate the sample thickness to the momentum, it is necessary to introduce time arguments. According to Ehrenfest's theorem,

$$\frac{d}{dt}\langle p_\perp \rangle = \frac{1}{i\hbar}\langle [p_\perp, H] \rangle + \langle \frac{\partial p_\perp}{\partial t} \rangle \tag{2.4}$$

where H is Hamiltonian. Since $\partial p_\perp / \partial t = 0$, we get

$$\frac{d}{dt}\langle p_\perp \rangle = \frac{1}{i\hbar}\langle [p_\perp, H] \rangle \tag{2.5}$$

The Hamiltonian of a charged particle in an electric field is

$$H = \frac{1}{2m_e} p^2 + eV \tag{2.6}$$

$$p_\perp = -i\hbar\nabla_\perp \tag{2.7}$$

And then,

$$[p_\perp, p^2] = 0 \tag{2.8}$$

$$[p_\perp, V] = -i\hbar \mathrm{grad}_\perp V = i\hbar E_\perp^{\mathrm{full}} \tag{2.9}$$

where $E_\perp^{\mathrm{full}}$ represents the lateral component of the field, m_e and e are the mass and charge of the electron, and V is the electrostatic potential, $p_\perp$ is the momentum operator. Then Ehrenfest's theorem is simplified to

$$\frac{d}{dt}\langle p_\perp \rangle = \frac{1}{i\hbar}\langle [p_\perp, H] \rangle = -e\langle E_\perp^{\mathrm{full}} \rangle \tag{2.10}$$

Using a paraxial approximation of $\frac{d}{dt} = \frac{dz}{dt}\frac{d}{dz} = v\frac{d}{dz}$ to convert the momentum function of t to the momentum function of z, we get

$$\frac{d}{dz}\langle p_\perp \rangle = -\frac{e}{v}\langle E_\perp^{\mathrm{full}} \rangle \tag{2.11}$$

Here, the expectation value of $E_\perp^{\mathrm{full}}$ is defined as

$$\langle E_\perp^{\mathrm{full}} \rangle = \langle \psi | \mathrm{E}_\perp^{\mathrm{full}} | \psi \rangle = \int E_\perp^{\mathrm{full}}(r_\perp, z)\psi^*(r_\perp, z)\psi(r_\perp, z)\, d^2 r_\perp \tag{2.12}$$

where the wave function $\psi(r_\perp, z)$ is the function of the position *x*, *y*, *z* inside the sample, which is unknown and affected by the unknown electrostatic field. To solve this problem, an approximation of the integration along *z* is made and results in the total change of the average momentum as

$$\Delta\langle p_\perp\rangle = -\frac{e}{v}\int\langle E_\perp^{\text{full}}\rangle dz = -\frac{e}{v}\iint E_\perp^{\text{full}}(r_\perp, z)\psi^*(r_\perp, z)\psi(r_\perp, z)d^2r_\perp dz \tag{2.13}$$

For a thin sample, we assume that the intensity of the electron wave is independent of *z*. The intensity at the incident wave is $I(r_\perp, z) = \psi^*(r_\perp, z=0)\psi(r_\perp, z=0) = I(r_\perp, 0)$. Then the electric field averaged in z-direction $E_\perp^a$ is

$$E_\perp^a(r_\perp) = \frac{1}{\Delta Z}\int E_\perp^{\text{full}}(r_\perp, z)dz \tag{2.14}$$

Assuming $\langle p_\perp\rangle = 0$ for the incident beam (z = 0), the momentum transfer becomes

$$\langle p_\perp\rangle = -\frac{ez}{v}\int E_\perp^a(r_\perp)I(r_\perp, 0)d^2r_\perp \tag{2.15}$$

In STEM mode, the position of the electron probe $R_\perp$ is changed instead of the intensity, the beam intensity of $I(r_\perp, 0)$ is rewritten as $I_{\text{Beam}}(R_\perp - r_\perp,\ 0)$. Then the measured electric field $E_\perp$ is a convolution of the true electric field $E_\perp^a$ with the intensity of the electron beam,

$$E_\perp(R_\perp - r_\perp) = \int E_\perp^a(r_\perp)I_{Beam}(R_\perp - r_\perp,\ 0)d^2r_\perp = E_\perp^a \otimes I_{\text{Beam}} \tag{2.16}$$

$$\langle p_\perp\rangle = -\frac{ez}{v}E_\perp^a \otimes I_{\text{Beam}} \tag{2.17}$$

Finally, we obtain the relationship between the measured electrostatic field and the momentum transfer projection averaged along the electron beam direction as shown below,

$$E_\perp = -\langle p_\perp\rangle\frac{v}{ez} \tag{2.18}$$

According to Maxwell's theory, we can convert the divergence of the electric field into the charge density,

$$\text{div}_\perp\langle p_\perp\rangle = -\frac{ez}{v}\text{div}_\perp E_\perp^a \otimes I_{\text{Beam}} = -\frac{e^2z}{v\varepsilon_0}\rho_\perp^T \otimes I_{\text{Beam}} \tag{2.19}$$

where ε_0 is the vacuum permittivity and $\rho_\perp^T$ is the total true charge density consisting of the electron and proton densities. In the experiment, the expectation value of the momentum transfer can be measured by calculating the center of mass of the diffraction patterns using fast detectors. Therefore, the measuring probe convolved electric field and charge density are

$$E_\perp = -h\frac{\sin(CoM)}{\lambda}\frac{v}{ez} \tag{2.20}$$

$$\rho_\perp = \varepsilon_0\left(\frac{\partial E_x}{\partial E_x} + \frac{\partial E_y}{\partial E_y}\right) \tag{2.21}$$

where *h* is Planck's constant and λ is the wavelength of the electron.

Mathematical formulation of the imaging process in STEM. This method mathematically represents the variations in amplitude and phase of the electron wave from formation, through interaction with the sample, to the detector plane. Figure 2.8 shows the schematic structure of a STEM mode. An electron probe is formed by the convergent lens and selected by a condenser aperture. We start with the wave function of $\psi(\vec{k})$ at the back focal plane, including an aperture factor of $A(\vec{k})$, an aberration factor of $e^{-i\chi(\vec{k})}$, and factors of spatial and temporal coherence of the source. Then the wave function of the input wave at the sample plane is

$$\psi_{\text{input}}(\vec{r}) = \mathcal{F}\left[\psi(\vec{k})\right](\vec{r}) \tag{2.22}$$

For a thin non-magnetic sample, we assume no amplitude change and only a phase change. Then the output wave function can be described as

$$\psi_{\text{output}}(\vec{r}, \vec{r}_p) = \psi_{\text{input}}(\vec{r}) e^{-i\varphi(\vec{r}+\vec{r}_p)} \tag{2.23}$$

Where the $e^{-i\varphi(\vec{r}+\vec{r}_p)}$ is a transmission function with a phase change and probe position $\vec{r}_p$. The wave function at the detector plane is the Fourier transform of the output wave function,

$$\psi_{\text{detector}}(\vec{k}, \vec{r}_p) = \mathcal{F}\left[\psi_{\text{output}}(\vec{r}, \vec{r}_p)\right](\vec{k}) = \mathcal{F}\left[\psi_{\text{input}}(\vec{r})\right](\vec{k}) \otimes \mathcal{F}\left[e^{-i\varphi(\vec{r}+\vec{r}_p)}\right](\vec{k}) \tag{2.24}$$

where $\otimes$ indicates a convolution. The convolution is defined as $\left(f(\vec{r}') \otimes g(\vec{r}')\right)(\vec{r}) \equiv \iint_{-\infty}^{\infty} f(\vec{r}')g(\vec{r} - \vec{r}')\mathrm{d}^2\vec{r}'$. The beam intensity at the detector plane is

$$I_{\text{detector}}(\vec{k}, \vec{r}_p) = |\psi_{\text{detector}}(\vec{k}, \vec{r}_p)|^2 \tag{2.25}$$

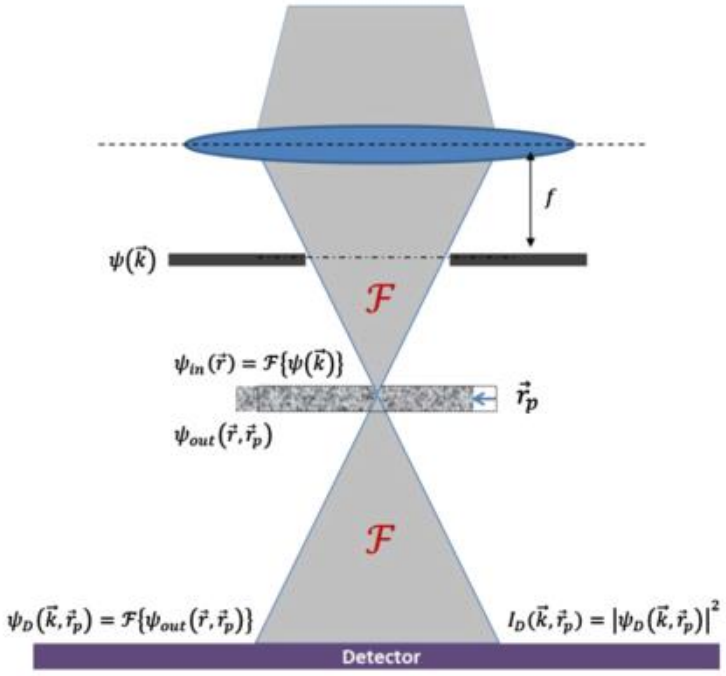

Figure 2.8 Imaging process in STEM (Reproduced from the Ref.[45]).

For a two-dimensional object with varying density $\sigma(x, y)$, the center of mass is

$$\mathrm{CoM}_x = \int\int x\sigma(x,y)\mathrm{d}x\mathrm{d}y \tag{2.26}$$

$$\mathrm{CoM}_y = \int\int y\sigma(x,y)\mathrm{d}x\mathrm{d}y \tag{2.27}$$

Then we can calculate the center of mass of the diffraction pattern I^{CoM_x} and I^{CoM_y},

$$I^{\mathrm{CoM}_x}(\vec{r}_p) = \iint_{-\infty}^{\infty} k_x I_{\mathrm{detector}}(\vec{k},\vec{r}_p)\mathrm{d}^2\vec{k} = \iint_{-\infty}^{\infty} k_x |\psi_{\mathrm{detector}}(\vec{k},\vec{r}_p)|^2\mathrm{d}^2\vec{k} \tag{2.28}$$

$$I^{\mathrm{CoM}_y}(\vec{r}_p) = \iint_{-\infty}^{\infty} k_y I_{\mathrm{detector}}(\vec{k},\vec{r}_p)\mathrm{d}^2\vec{k} = \iint_{-\infty}^{\infty} k_y |\psi_{\mathrm{detector}}(\vec{k},\vec{r}_p)|^2\mathrm{d}^2\vec{k} \tag{2.29}$$

where $\vec{k} = (k_x, k_y)$. With $\psi_{\mathrm{detector}}(\vec{k},\vec{r}_p) = \mathcal{F}[\psi_{\mathrm{output}}(\vec{r},\vec{r}_p)](\vec{k})$ mentioned above, we get

$$I^{\mathrm{CoM}_x}(\vec{r}_p) = \iint_{-\infty}^{\infty} k_x \mathcal{F}^*[\psi_{\mathrm{output}}(\vec{r}',\vec{r}_p)](\vec{k}) \cdot \mathcal{F}[\psi_{\mathrm{output}}(\vec{r}',\vec{r}_p)](\vec{k})\mathrm{d}^2\vec{k} \tag{2.30}$$

Given $k_x\mathcal{F}[f(\vec{r})] = \frac{1}{2\pi i}\mathcal{F}\left[\frac{\partial}{\partial x}f(\vec{r})\right]$ and $\mathcal{F}^*[f(\vec{r})] = \mathcal{F}[f^*(-\vec{r})]$, I^{CoM_x} can be written as

$$I^{\mathrm{CoM}_x}(\vec{r}_p) = \frac{1}{2\pi i}\iint_{-\infty}^{\infty} \mathcal{F}\left[\frac{\partial}{\partial x'}\psi_{\mathrm{output}}(\vec{r}',\vec{r}_p)\right](\vec{k}) \cdot \mathcal{F}[\psi^*_{\mathrm{output}}(-\vec{r}',\vec{r}_p)](\vec{k})\mathrm{d}^2\vec{k} \tag{2.31}$$

Since the product of the two Fourier transforms is equal to the Fourier transform of the convolution based on the convolution theorem, we get

$$I^{\mathrm{CoM}_x}(\vec{r}_p) = \frac{1}{2\pi i}\iint_{-\infty}^{\infty} \mathcal{F}\left[\left[\frac{\partial}{\partial x}\psi_{\mathrm{output}}(\vec{r},\vec{r}_p)\right] \otimes \psi^*_{\mathrm{output}}(-\vec{r},\vec{r}_p)\right](\vec{r}')\Big](\vec{k})\mathrm{d}^2\vec{k} \tag{2.32}$$

Since $\iint_{-\infty}^{\infty}\mathcal{F}[f(\vec{r})](\vec{k})\mathrm{d}^2\vec{k} = f(0)$, assuming the above integration is finite, we get

$$I^{\mathrm{CoM}_x}(\vec{r}_p) = \frac{1}{2\pi i}\left[\left[\frac{\partial}{\partial x}\psi_{\mathrm{output}}(\vec{r},\vec{r}_p)\right] \otimes \psi^*_{\mathrm{output}}(-\vec{r},\vec{r}_p)\right](\vec{r}')\Big|_{\vec{r}'=0} \tag{2.33}$$

By introducing the convolution relation $\left(f(\vec{r}') \otimes g(\vec{r}')\right)(\vec{r}) \equiv \iint_{-\infty}^{\infty} f(\vec{r}')\, g(\vec{r}-\vec{r}')\mathrm{d}^2\vec{r}'$, we obtain

$$I^{\mathrm{CoM}_x}(\vec{r}_p) = \frac{1}{2\pi i}\iint_{-\infty}^{\infty}\left[\frac{\partial}{\partial x}\psi_{\mathrm{output}}(\vec{r},\vec{r}_p)\right] \cdot \psi^*_{\mathrm{output}}(-(\vec{r}'-\vec{r}),\vec{r}_p)\mathrm{d}^2\vec{r}\Big|_{\vec{r}'=0} \tag{2.34}$$

For $\vec{r}' = 0$,

$$I^{\mathrm{CoM}_x}(\vec{r}_p) = \frac{1}{2\pi i}\iint_{-\infty}^{\infty}\left[\frac{\partial}{\partial x}\psi_{\mathrm{output}}(\vec{r},\vec{r}_p)\right] \cdot \psi^*_{\mathrm{output}}(\vec{r},\vec{r}_p)\mathrm{d}^2\vec{r} \tag{2.35}$$

we can transfer the ψ_{output} to ψ_{input} duo to the phase change for a thin sample, then

$$I^{\mathrm{CoM}_x}(\vec{r}_p) = \frac{1}{2\pi i}\iint_{-\infty}^{\infty}\frac{\partial\psi_{\mathrm{input}}(\vec{r})}{\partial x} \cdot \psi^*_{\mathrm{input}}(\vec{r})\mathrm{d}^2\vec{r} + \frac{1}{2\pi}\iint_{-\infty}^{\infty}\psi_{\mathrm{input}}(\vec{r}) \cdot \psi^*_{\mathrm{input}}(\vec{r}) \cdot \frac{\partial\varphi(\vec{r}+\vec{r}_p)}{\partial x}\mathrm{d}^2\vec{r} = C + \frac{1}{2\pi}\left[|\psi_{\mathrm{input}}(\vec{r})|^2 \star \frac{\partial\varphi(\vec{r})}{\partial x}\right](\vec{r}_p) \tag{2.36}$$

where the first term is a constant (C) wave that is not a function of $\vec{r}_p$ and is independent of the sample. The $\star$ indicates a cross-correlation between $\left|\psi_{\text{input}}(\vec{r})\right|^2$ and $\frac{\partial\varphi(\vec{r})}{\partial x}$ with the definition of $\left(f(\vec{r}') \star g(\vec{r}')\right)(\vec{r}) \equiv \iint_{-\infty}^{\infty} f^*(\vec{r}')\, g(\vec{r}'+\vec{r})\mathrm{d}^2\vec{r}'$. Similarly, the y-component of the center of mass of the diffraction pattern $I^{\mathrm{CoM}_y}\left(\vec{r}_p\right)$ can be obtained in the same way. Furthermore, a vector image of $\vec{I}^{\mathrm{CoM}}$ with a combination of $I^{\mathrm{CoM}_y}\left(\vec{r}_p\right)$ and $I^{\mathrm{CoM}_x}\left(\vec{r}_p\right)$ can be written as

$$\vec{I}^{\mathrm{CoM}}\left(\vec{r}_p\right) = I^{\mathrm{CoM}_x}\left(\vec{r}_p\right)\cdot\vec{k}_x + I^{\mathrm{CoM}_y}\left(\vec{r}_p\right)\cdot\vec{k}_y \tag{2.37}$$

where $\vec{k}_x$ and $\vec{k}_y$ are the unit vectors in the detector plane. Finally, we obtain the proof of a linear behavior between the gradient of the phase variation and the displacement of the center of mass of the diffraction pattern in STEM imaging,

$$\vec{I}^{\mathrm{CoM}}\left(\vec{r}_p\right) == C + \frac{1}{2\pi}\left[\left|\psi_{\text{input}}(\vec{r})\right|^2 \star \vec{\nabla}\varphi(\vec{r})\right]\left(\vec{r}_p\right) \tag{2.38}$$

An integrated CoM image $I^{\mathrm{iCoM}}\left(\vec{r}_p\right)$ can be written as

$$I^{\mathrm{iCoM}}\left(\vec{r}_p\right) = \frac{1}{2\pi}\left[\left|\psi_{\text{input}}(\vec{r})\right|^2 \star \varphi(\vec{r})\right]\left(\vec{r}_p\right) \tag{2.39}$$

The divergence of the CoM image $I^{\mathrm{dCoM}}\left(\vec{r}_p\right)$ is

$$I^{\mathrm{dCoM}}\left(\vec{r}_p\right) = \vec{\nabla}\cdot\vec{I}^{\mathrm{CoM}}\left(\vec{r}_p\right) = \frac{1}{2\pi}\left[\left|\psi_{\text{input}}(\vec{r})\right|^2 \star \nabla^2\varphi(\vec{r})\right]\left(\vec{r}_p\right) \tag{2.40}$$

For non-magnetic thin samples, the phase variations are proportional to the projected electrostatic potential, which can be related to the electrostatic field, and charge density according to Poisson's equation and Gauss's law,

$$\nabla^2 V(\vec{r}) = -\vec{\nabla}\cdot\vec{E}(\vec{r}) = -\frac{1}{\varepsilon_0}\rho(\vec{r}) \tag{2.41}$$

2.2.2.4 Electron ptychography

The name ptychography is derived from the Greek word "ptycho", which means to fold. Ptychography was first proposed by Walter Hoppe in 1969 to retrieve a crystal structure by calculating the phase of Bragg reflections.[46] It can be used for imaging with visible light, X-rays, extreme UV light, and electrons, and its resolution is not affected by beam diameter, optical aberration, and numerical aperture.[47] The main idea of electron ptychography is that the interference of two overlapping diffraction patterns can be used to estimate their phase difference. However, it seems to be very difficult to inverse the recorded interfering diffraction patterns by Fourier transform due to a phase assignment problem for the phase lost part.[48] To solve the ptychography inverse problem, various strategies have been invented to perform this calculation, such as Single Side Band (SSB) deconvolution[49], Wigner distribution deconvolution (WDD),[50] and iterative methods.[51-54]

2.2.3 Electron energy-loss spectroscopy

Electron Energy Loss Spectroscopy (EELS) is a powerful analytical technique that measures the energy distribution of scattered electrons that have interacted with a sample to provide information about the composition, chemical state, and structure of the sample. EELS can be used in both TEM and STEM modes. In STEM-EELS, the focused electron beam scans a thin sample and the energy loss of the electrons interacting with the sample can be measured by the EELS spectrometer at each probe position. This allows simultaneous acquisition of spectral data and atomic-scale imaging. As shown in Figure 2.9, the electrons with elastic interaction or no interaction between electron beam and the sample result in a zero loss peak. The inelastic interactions mainly include the phonon excitations, inter- and intra-band transitions, plasmon excitations, and inner shell ionizations. The energy ranges of these interactions are different and can be used for specific material characterization applications. Phonon excitation indicates atomic vibrations in a crystal lattice and the corresponding energy loss is on the order of milli-electron volts (meV). Plasmon excitation is the collective oscillation of electrons in a metal or semiconductor material with an energy range between 5 eV and 30 eV. The energy of the inter- and intra-band transition is in the range of 5 eV and 25 eV, giving the bandgap energy. Inner-shell excitation produces ionization edges, which indicate the ionization threshold and correspond to the binding energy of the inner shell. The typical energy loss is less than ~2 keV. The primary technique used in this study is core-loss EELS, which allows identification of the valence state of transition metals and elemental mapping in oxide materials.

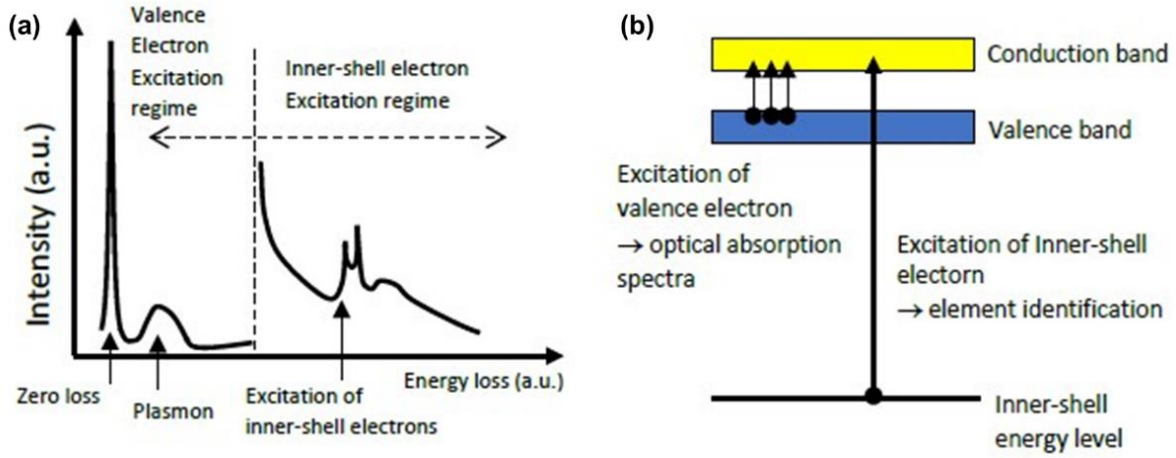

Figure 2.9 (a) Energy-loss spectrum with different loss mechanisms. (b) Excitation mechanisms in the sample. (image reproduced from https://www.mst.or.jp)

2.2.4 Energy-dispersive X-ray spectroscopy

Energy dispersive X-ray spectroscopy (EDX) is a commonly used analytical technique for elemental analysis and chemical characterization of a sample. It is easier to obtain elemental composition information from a larger area of a sample compared to EELS. In addition, EDX has a broader energy range than EELS, making it more effective in detecting heavy elements. Figure 2.10 presents the principle of EDX. When a sample is excited by an energy source (e.g., an electron beam from an electron microscope), it releases some of the absorbed energy by ejecting an electron located in the core shell of an atom. Subsequently, an electron located in an outer shell with higher energy levels moves into the

vacant core shell, producing an X-ray with a unique spectrum based on the originating atom. By combining EDX and ACSTEM, we can obtain atomic resolution elemental mapping using STEM-EDX. In this work, STEM-EDX was used to measure Sr doping and elemental distribution in nickelate films.

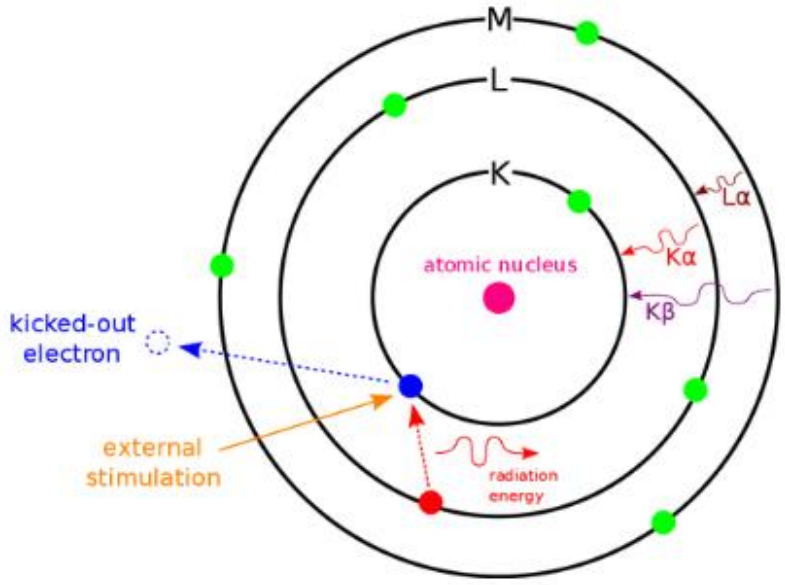

Figure 2.10 Principle of EDX. The process of external stimulation and the characteristic X-rays produced. (image reproduced from https://chem.libretexts.org)

2.3 Data processing and simulations

STEM is capable of characterizing the structural information and electrostatic characteristics of materials. By relying on data processing and simulations, we can extract valuable information from the STEM images and EELS spectra. Here, I will introduce several image processing methods and simulations used in this thesis.

2.3.1 Lattice deformation quantification

Understanding the atomic structure is critical to understanding the physical and chemical properties of oxide materials. By characterizing the atomic locations/positions in STEM images, we can analyze factors such as strain, oxygen occupancy, and distortion. The identification of atomic positions can be achieved by intensity fitting with Gaussian functions and center of mass calculations, which always involves some image denoising methods such as principal component analysis (PCA) and filtering techniques. Here, I use a Python library of Atomap[55] to quantify lattice distortions and oxygen occupancies in our images.

The atom detection process can be summarized in three steps: (a) denoise the images using the PCA method; (b) search for atomic positions in a given region of a STEM image; (c) refine the positions using center of mass calculation; (d) fit the atomic columns as a 2-D elliptical Gaussian function. The PCA method is used to improve the image quality. The center of mass calculation function of atomic columns in a 2D image was similar to the functions described in (2.26) and (2.27). The 2-D elliptic Gaussian function is defined as

$$I(x,y) = I_b + Aexp(-(a(x-x_0)^2 - 2b(x-x_0)(y-y_0) + c(y-y_0)^2)) \quad (2.42)$$

$$a = \frac{cos^2\theta}{2\sigma_x^2} + \frac{sin^2\theta}{2\sigma_y^2} \quad (2.43)$$

$$b = -\frac{sin2\theta}{4\sigma_x^2} + \frac{sin2\theta}{4\sigma_y^2} \quad (2.44)$$

$$c = \frac{sin^2\theta}{2\sigma_x^2} + \frac{cos^2\theta}{2\sigma_y^2} \quad (2.45)$$

where $I(x,y)$ is the Gaussian function, I_b is the background intensity, A is the amplitude, σ_x, σ_y are the standard deviations, x_0, y_0 are the center positions.[55]

2.3.3 4D-STEM simulation

As mentioned above, the field information can be reconstructed using the center of mass calculation of 4D-STEM data. A critical assumption for the field reconstruction is that the intensity of the electron wave is independent of *z*, since the electron wave function is complex and difficult to determine in a thick sample. In addition to the thickness effect, the contrasts from defects or asymmetric structures can cause the center of mass of CBED patterns to shift, creating a kind of artifact in the reconstruction of electrostatic fields. To understand these effects, 4D-STEM simulation is essential. Here, we briefly introduce two methods of 4D-STEM simulations used in this thesis.

QSTEM simulation.

QSTEM was developed by Prof. Dr. Christoph T. Koch[56] of the Humboldt University of Berlin. It is a well-established TEM image simulation software with a user-friendly interface based on the multislice algorithm with frozen phonon modeling, which allows the simulation of HAADF-STEM, ADF-STEM, ABF-STEM, and TEM images as well as diffraction patterns. By comparing the simulated TEM and experimental images, we can estimate specific structures and compositions of materials, e.g., defects, and non-stoichiometric structures. The simulation can be used to evaluate the effects of artifacts from beam broadening, tilt, asymmetric structure to quantitatively interpret the experimental images and spectral analysis. In this work, the simulations of HAADF and ABF images were performed to estimate the atomic structure of a grain boundary in a high-angle $SrTiO_3$ bicrystal. In addition, 4D-STEM simulations were performed by analyzing the diffraction patterns recorded for each probe position in QSTEM. Furthermore, it is possible to define non-stoichiometric element occupancies when building a supercell structure model. For more detailed theories of this simulation, please refer to the Ph.D. thesis of Prof. Dr. Christoph T. Koch.[56] The user manual is described on this website: https://www.physik.hu-berlin.de/en/sem/software/qstem-documentation.

abTEM simulation.

abTEM is another TEM image simulation package based on the multislice algorithm.[57] The main difference of this technique is the introduction of chemical bonding information, which is neglected in other TEM simulation packages. The electrostatic potential of a sample affects the transmission of electrons scattered through the sample. By comparing the images from experiment and simulation, one can understand the properties of the samples. Most TEM image simulations have used an Independent

Atom Model (IAM), which approximates the electrostatic potential of a sample as a superposition of isolated atoms. However, the chemical bonding between neighboring atoms can affect electron scattering. In this package, the electrostatic potential calculated by density functional theory has been introduced into the image simulations, allowing the valence bonding information to be compared with the experiment. This package is based on Python and connects to other atomic simulation environments such as the DFT code GPAW and IAM. It can be run on GPUs to improve computational performance. In this thesis, I performed the 4D-STEM simulation to calculate the center of mass of the electron beam shift. The step-by-step introduction to abTEM simulation is described on this website: https://abtem.readthedocs.io/en/latest/index.html.

Chapter 3 Grain-boundary structure and electrostatic characteristics in a $SrTiO_3$ bicrystal

3.1 Introduction

Direct imaging of electrostatic characteristics and determination of the magnitude and distribution of space charges at grain boundaries has always been challenging and has attracted attention for decades. Mainstream techniques use phase-contrast imaging, which is sensitive to electrostatic potentials in solids. For example, offline and inline electron holography, where the phase is reconstructed from the scattered exit electron wave through the object, allows imaging of the electrostatic potential with nanometer spatial resolution.[58-62] More recently, DPC has been used to reconstruct the electrostatic potential with atomic resolution from the difference signal of opposing detector segments. This difference signal is proportional to the beam deflection along the direction connecting the two segments.[43, 63-65] Shibata *et al.* described how the application of a segmented detector in DPC-STEM imaging enables real-time reconstruction of the HAADF image, the electric field vector map, and the charge density map, thus allowing the simultaneous acquisition of local atomic structure and chemical information from the same area.[63] Further progress has been made by using pixelated detectors instead of segmented detectors. Such pixelated detectors allow the acquisition of a complete diffraction pattern for each probe position on the specimen, also known as 4D-STEM. This has made it possible to measure electrostatic fields at the atomic scale, and a simplified quantum mechanical approach has been proposed to measure electric fields.[44] Gao *et al.* reported the quantitative characterization of the electric field and charge density of an ultrathin $SrTiO_3/BiFeO_3$ heterojunction at sub-angstrom resolution using 4D-STEM.[66] In addition, 4D-STEM can be used to image the electric field on a large scale, such as the polarization-induced internal electric field in 110 nm thick wurtzite AlN/GaN nanowires.[67] In general, most studies of electrostatic properties focus on heterojunctions, interfaces or point defects. The simultaneous characterization of atomic structure and electrostatic characteristics in more complicated defects, such as grain boundaries in electroceramic materials, is critical and essential to explore the mechanisms of electrical and mechanical behavior.

GBs play a dominant role in the electrical properties of many electroceramics. This is often related to non-stoichiometry or segregation, which can promote the formation of space charges near GBs. These effects can control the electrical conductivity across and along GBs. In recent decades, the double Schottky barrier model of boundary electrical blocking in ionic solids has been established, which explains the electrical behavior of GBs by the presence of a GB core charge whose electric field is compensated by a space charge on each side of the GB.[58, 68-72] For example, positively charged defects, e.g., oxygen vacancies or excess cations on an acceptor-doped $SrTiO_3$ GB, form a potential barrier. A negatively charged space-charge zone in the adjacent bulk regions compensates for these positively charged defects.[73] In general, these descriptions of charged defects and space-charge layers are derived indirectly from experimental data on bulk properties, e.g., from impedance spectroscopy or I-V properties.[68, 74-77]

Here, we selected a $SrTiO_3$ bicrystal with a $\Sigma 5$ grain boundary, which has a large tilt angle of 36.9° and contains a large number of charged defects. The observation of incomplete oxygen octahedra at such interfaces indicates an altered coordination environment of the cations due to the absence of oxygen

anions. In addition, the intermixing of cations at the grain boundary is important for understanding the microstructure of the grain boundary. In this work, we present studies of the microstructure, chemical composition, and electrostatic characteristics of a Σ5 grain boundary in a $SrTiO_3$ bicrystal at the nanometer and atomic scale using 4D-STEM in combination with advanced aberration-corrected STEM and EELS. We discuss how the charged defects, the change in the Ti valence state, and the structural distortion affect the measured averaged momentum transfer and the electrostatic field at the grain boundary, and demonstrate the usefulness of 4D-STEM for understanding grain boundary electrical properties.

3.2 Experimental parameters

Figure 3.1 shows a sketch of the synthesis process of a bicrystal. A single crystal is cut into two pieces and then joined together at high pressure and temperature.

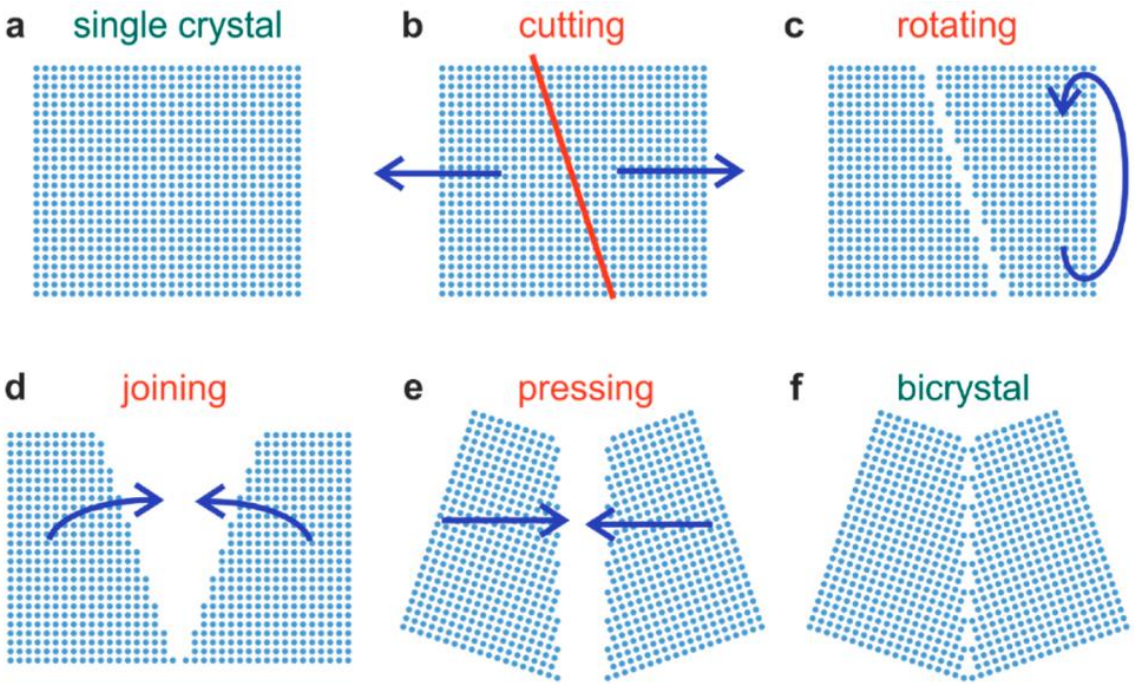

Figure 3.1 Synthesis process of a bicrystal.[78]

Here, a Σ 5 (310) [001] $SrTiO_3$ bicrystal was obtained from Shinkosha Co., Ltd. (Tokyo, Japan). The bicrystal has minute amounts of acceptor impurities (about 60 ppm), e.g., Fe, Cr, and Al, as determined by inductively coupled plasma optical emission spectroscopy (ICP-OES) analysis and listed in Table 3.1.

Table 3.1 Impurity concentration in $SrTiO_3$ bicrystal ceramics.

Host elements	*wt* %
Sr	47.6 ± 0.5
Ti	26.1 ± 0.3
O	25.9 ± 0.3

Impurities	*wt* %	*at%*
Si	0.01	0.066
Ca	0.01	0.046
Ba	0.007	0.009
Cr	0.001	0.004
Mg	0.0001	< 0.001
Fe	0.0001	< 0.001
Al	0.0002	0.001

These impurities act as acceptor dopants, which are compensated by oxygen vacancies. From the ICP-OES data, the oxygen deficiency amounts to about 0.2 at%. These acceptor dopants can induce the formation of oxygen vacancies according to the following formula,

$$A_2O_3 + 2Ti_{Ti}^{x} + O_O^{x} \rightleftharpoons 2A_{Ti}'' + V_O^{\cdot\cdot} + 2TiO_2$$

where A represents trivalent impurities. Besides, due to the intrinsic Schottky disorder reaction,

$$Sr_{Sr}^{x} + O_O^{x} \rightleftharpoons V_{Sr}'' + V_O^{\cdot\cdot} + SrO,$$

the concentration of frozen-in oxygen vacancies (about 56 ppm) can be estimated from the following Schottky equation (assuming they are frozen in at 1200 °C),[79]

$$[V_{Sr}''][V_O^{\cdot\cdot}] = K_S(T) = K_S^o \exp(\frac{E_S}{kT}) \quad (3.10)$$

where $[V_{Sr}'']$ is the ionized strontium vacancies, $[V_O^{\cdot\cdot}]$ indicates the oxygen vacancy, K_S is Schottky constant, E_S is Schottky energy, k is Boltzmann constant, T is temperature. Thus, Debye length λ and space-charge layer width λ^* can be calculated according to the double-Schottky-barrier model,[75]

$$\lambda = \sqrt{\frac{\varepsilon_0 \varepsilon_r kT}{2z_j^2 e^2 c_j}}, \quad (3.11)$$

$$\lambda^* = \sqrt{\frac{2\varepsilon_0 \varepsilon_r \Delta\emptyset_0}{z_j e c_j}}, \quad (3.12)$$

where ε_0 is the vacuum dielectric constant, ε_r is the dielectric permittivity of the material, z_j indicates the charge number of defect j, e is the elementary charge, and c_j is the concentration of defect j. We calculate a Debye length of around 3.1 nm. The width of the Mott-Schottky space charge layer is around 69 nm. The TEM specimen was prepared by a combination of dimple grinding and Ar-ion milling. The Ar-ion milling process is performed at liquid nitrogen temperature using a Gatan precision ion polishing system (Gatan PIPS, model 691).

The STEM investigations were performed on a spherical-aberration-corrected microscope (JEOL ARM200F, JEOL Co. Ltd.) equipped with a DCOR probe corrector (CEOS GmbH) and a Gatan GIF Quantum ERS K2 camera at 200 kV. The convergence semi-angle of the electron probe was 20.4 mrad for STEM imaging, and 6 mrad for large area electric field measurement. Generally, the convergence angle can be tuned by inserting different convergence apertures. The smallest convergence aperture is

20 µm with a convergence angle of around 14 mrad in our ARM200F microscope. To obtain a smaller convergence angle, we can manually reduce the convergence lens current while carefully aligning the corrector to obtain a perfect experimental parameter. The smallest convergence angle in this way can be achieved to around 3 mrad with a well-corrected electron probe, which is limited by the experimental setup. The convergence angle can be smaller if the beam correction is sacrificed. The range of collection semi-angles for HAADF imaging and ABF imaging was 70-300 mrad and 10-20 mrad, respectively. Spectral images were acquired with a dispersion of 0.5 eV per channel with an energy resolution of 1 eV and then de-noised using the PCA method.[80] A Merlin direct electron detector (256 × 256 pixels, Quantum Detectors) was used to record the diffraction patterns at each probe position. In the 4D-STEM experiments, the detector was operated in 1-bit continuous read/write mode with a pixel dwell time of 4.8×10^{-5} s, resulting in a frame rate of 20833 fps.

3.3 Results and Discussions

3.3.1 Broken symmetry at the grain boundary of a Σ5 (310) $SrTiO_3$ bicrystal

Fig. 3.2 shows atomically resolved STEM images of the Σ5 (310) [001] STO bicrystal, where Σ5 means that if we imagine both crystals overlapping, every fifth atomic position would be common to both lattices. Due to the translational asymmetry shown below, this geometric reasoning is not strictly true anymore. The Σ5 GB has a (310) GB plane and a [001] rotation axis.[81] Fig. 3.2 (a) and (b) show a uniform and high quality GB structure. We can easily identify the Sr and mixed Ti-O columns in the bulk region from the HAADF-STEM image according to the relationship between the atomic number *Z* and the intensity of each atomic column.[82] The tilt angle of the GB has the expected value of 36.9°. Besides, we find a translation of the two lattices of 0.05 nm parallel to the GB plane in Fig. 3.3, which is consistent with the reported values of 0.06 nm from HRTEM,[83] 0.05 nm from DFT and 0.07 nm from HAADF images.[70] Due to the reduced atomic contrast at the GB, we cannot distinguish the different elements from the HAADF image. The image contrast at the GB is weak, which is related to structural distortions, sample thickness, and/or the presence of vacancies.[83] From the corresponding ABF image in Fig. 3.2(c), the oxygen columns are clearly visible. This is the first attempt to image oxygen ions at a Σ5 GB in STO. In principle, not only cations but also anions are mirror symmetric with respect to the GB plane, if we ignore the small rigid-body translation.[83] However, the mirror symmetric structure is energetically unstable due to the close bonding of the oxygen ions.[83] We detect incomplete oxygen octahedra at the GB in Fig. 3.2c. In the TEM measurement, the structural distortion in the GB can hinder the quantification of O vacancies.

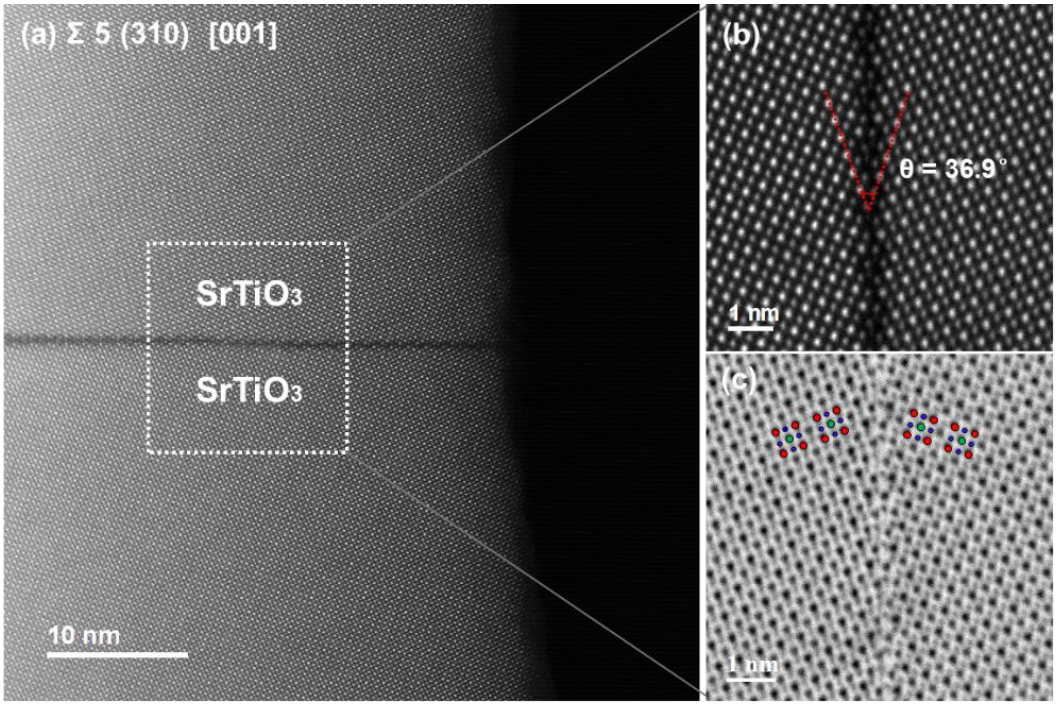

Figure 3.2 Microstructural characterization of the $SrTiO_3$ bicrystal. (a) An overview HAADF-STEM image of the Σ5 (310) [001] STO bicrystal. Atomically resolved (b) HAADF-STEM image and (c) ABF-STEM image, where oxygen columns are clearly visible and the image is overlaid with projections of the STO unit cell (Sr: red, Ti: green, O: blue).

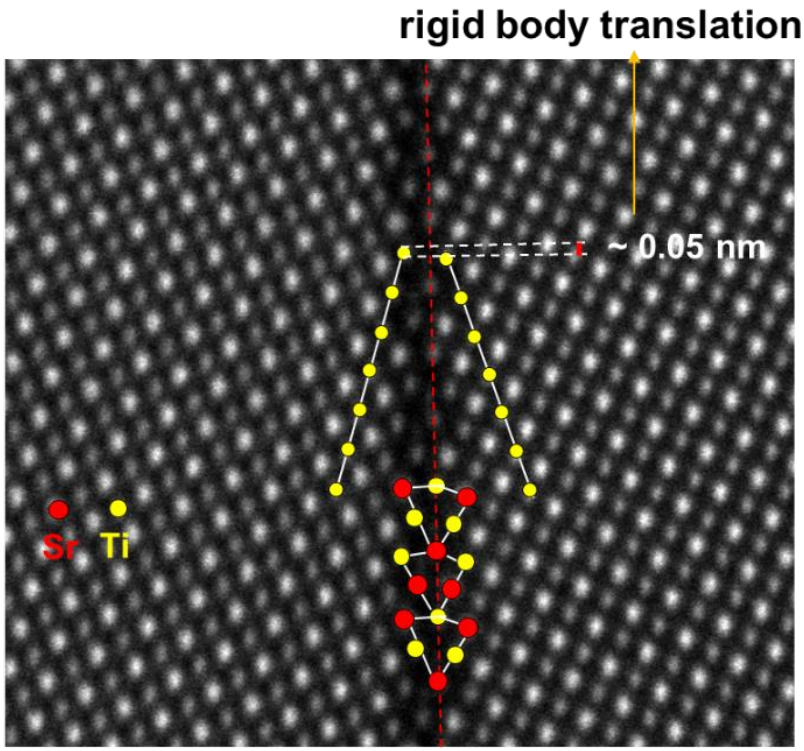

Figure 3.3 Rigid-body translation along the grain boundary perpendicular to the electron beam direction.

Furthermore, an apparent broken symmetry of the atomic structure at the GBs can induce structural distortion of the adjacent region, as shown in Figure 3.4. Specifically, there is a polar distortion of oxygen octahedra in the B region and an antiferrodistortive distortion in the adjacent A region, as shown in Fig. 3.4b. They are formed homogeneously at the periodic grain boundary core structure, which could affect the electrical and optical properties of the GBs. A similar antiferrodistortive distortion is observed at the GBs in a Σ13 (510)/[001] $SrTiO_3$ bicrystal,[84] which is induced by the expansion of the Ti ionic radii[84] and the formation of oxygen vacancies.[85] Besides, the polarity at the terminated surface at the GB may affect the oxygen distortion due to the electrostatic discontinuity.

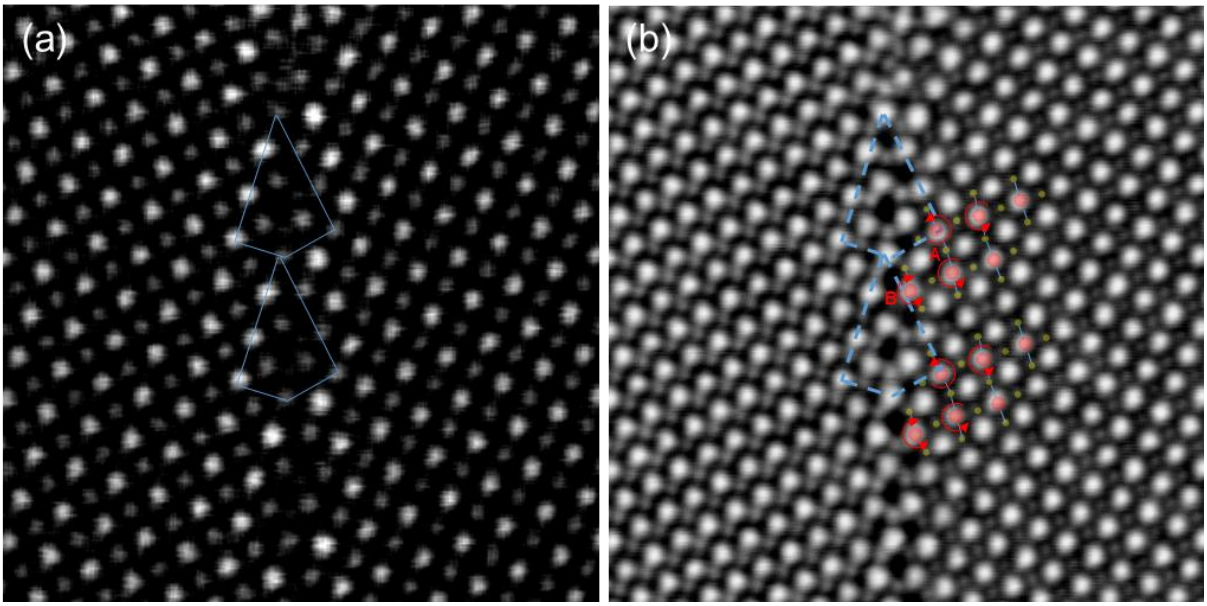

Figure 3.4 Structural distortion around the grain boundary of a $SrTiO_3$ bicrystal. (a) ADF image of the grain boundary. (b) Polar and antiferrodistortive distortions of oxygen octahedra around the grain boundary in regions A and B.

3.3.2 Elemental distribution at the grain boundary in a $SrTiO_3$ bicrystal

To determine the positions of the elements at the GB, we measured electron energy loss spectra (EELS) and extracted atomic resolution elemental maps to identify the different cations at the GB. Fig. 3.5a–c depicts the distribution of Ti and Sr. We find that the GB is rich in Ti, and the Ti columns marked with white arrows contain small amounts of Sr. Using the atomic information obtained from HAADF, ABF, and EELS mapping, we propose a possible structure of the GB core in Figure 3.5e. The red dots represent Sr, the blue dots represent O, and the green dots represent Ti. Compared to a perfect Σ5 GB core structure, the Sr sites are partially occupied by Ti atoms in the periodic GB core structure verified by EELS maps. The proposed GB core structure is stable under the electron probe, unlike the reported dislocation core structure.[86] In addition, we compared the relative signal intensities of Ti and O by tilting the grain boundary away from the zone axis and found that the Ti/O ratio shows an increase in the GB compared to that in the bulk, indicating excess Ti ions and oxygen vacancies in the GB, as shown in Fig. 3.6.

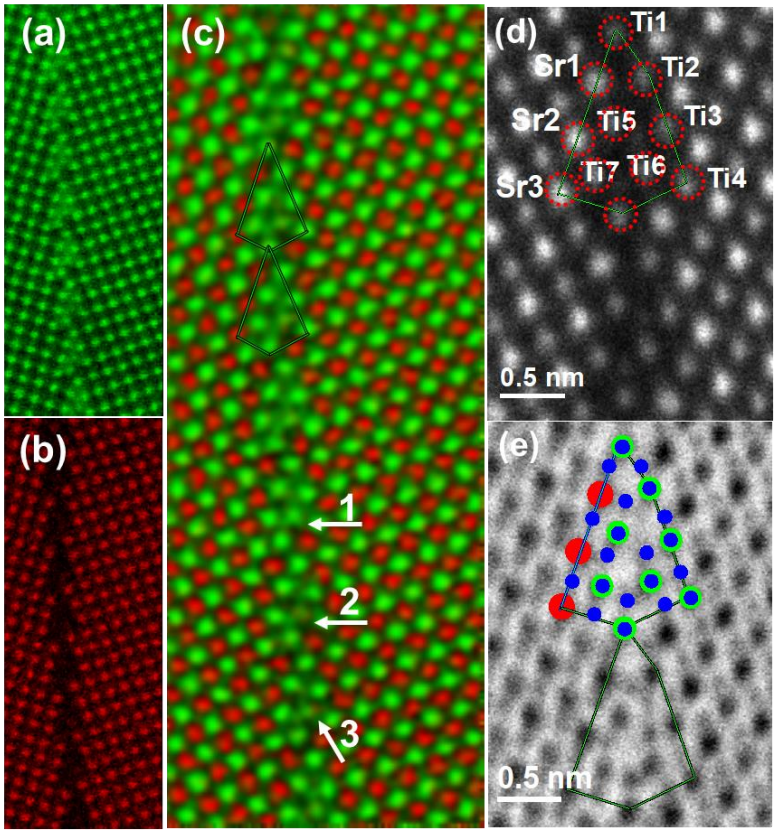

Figure 3.5 Elemental distribution at the Σ5 GB. EELS maps of Ti (a) and Sr (b). (c) Color-coded maps of Ti (green) and Sr (red). The white arrows indicate the atomic columns with intermixing of Sr and Ti. (d) ADF image of the GB. The cations of the GB core are marked with red dashed circles. (e) Experimental ABF image of the GB. Oxygen columns are marked with blue dots, Sr columns with red dots, and Ti columns with green dots.

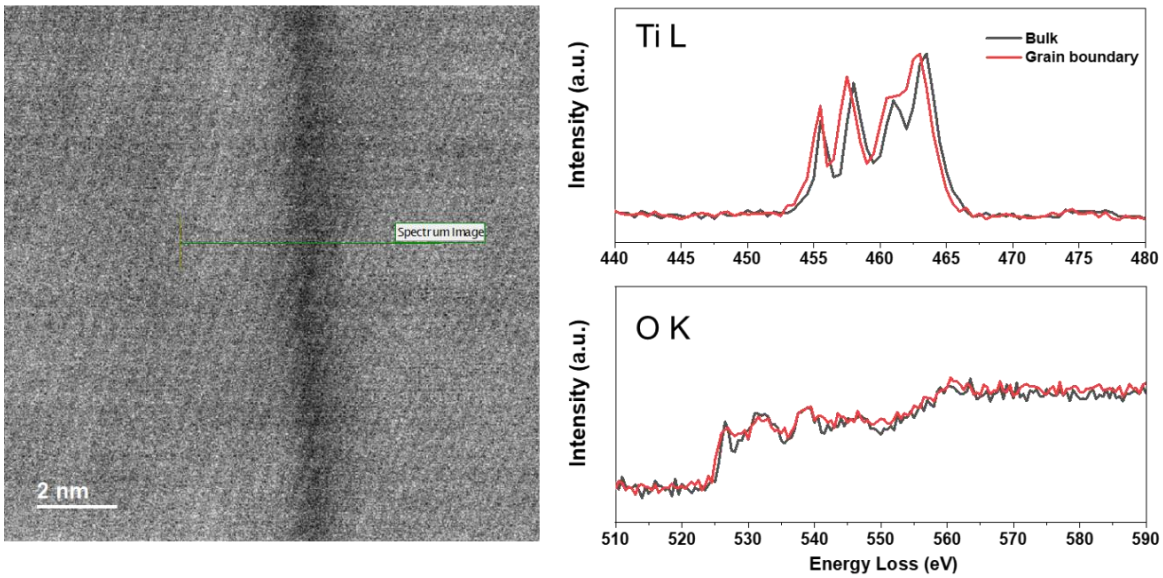

Figure 3.6 ADF image with off-axis tilt and corresponding Ti *L* and O *K* EELS spectra.

We explore the electronic structure by EELS fingerprint analysis as shown in Figure 3.7, and extract the Ti-$L_{2,3}$ white lines and O-K edge spectra separately from eight rectangular regions (Figure 3.7a). Using the bulk and GB spectra as references, a multiple linear least squares (MLLS) fit is shown in Figure 3.7b, c. We fit Ti-$L_{2,3}$ reference spectra for the lower valence state $Ti^{(4-\delta)+}$ and Ti (Ti^{4+}), respectively, to distinguish interfacial Ti (Figure 3.7b) from bulk Ti (Figure 3.7c). The energy shift of the Ti-$L_{2,3}$ peaks and the reduced peak splitting of the t_{2g} and e_g states at the GB (spectrum 5 in Figure 3.7d), compared to the spectra from regions 1-4 and 6-8 in Figure 3.7d, suggest an increased occupancy of the 3*d* orbitals, corresponding to a reduced Ti valence state at the GB.[87] Concurrently, the peak B of the O-K edge at the GB in Figure 3.7e decreases in intensity, which is associated with a reduction of the Ti valence, the presence of oxygen vacancies, or the absence of Sr columns.[88-90] In addition, we calculate the valence state of Ti using MLLS fitting, which yields a Ti valence state of around 3.75+ at the GB (Figure 3.7f). We use the Ti-$L_{2,3}$ spectra of $LaTiO_3$[91-92] and bulk $SrTiO_3$ as references for Ti^{3+} and Ti^{4+}, respectively.

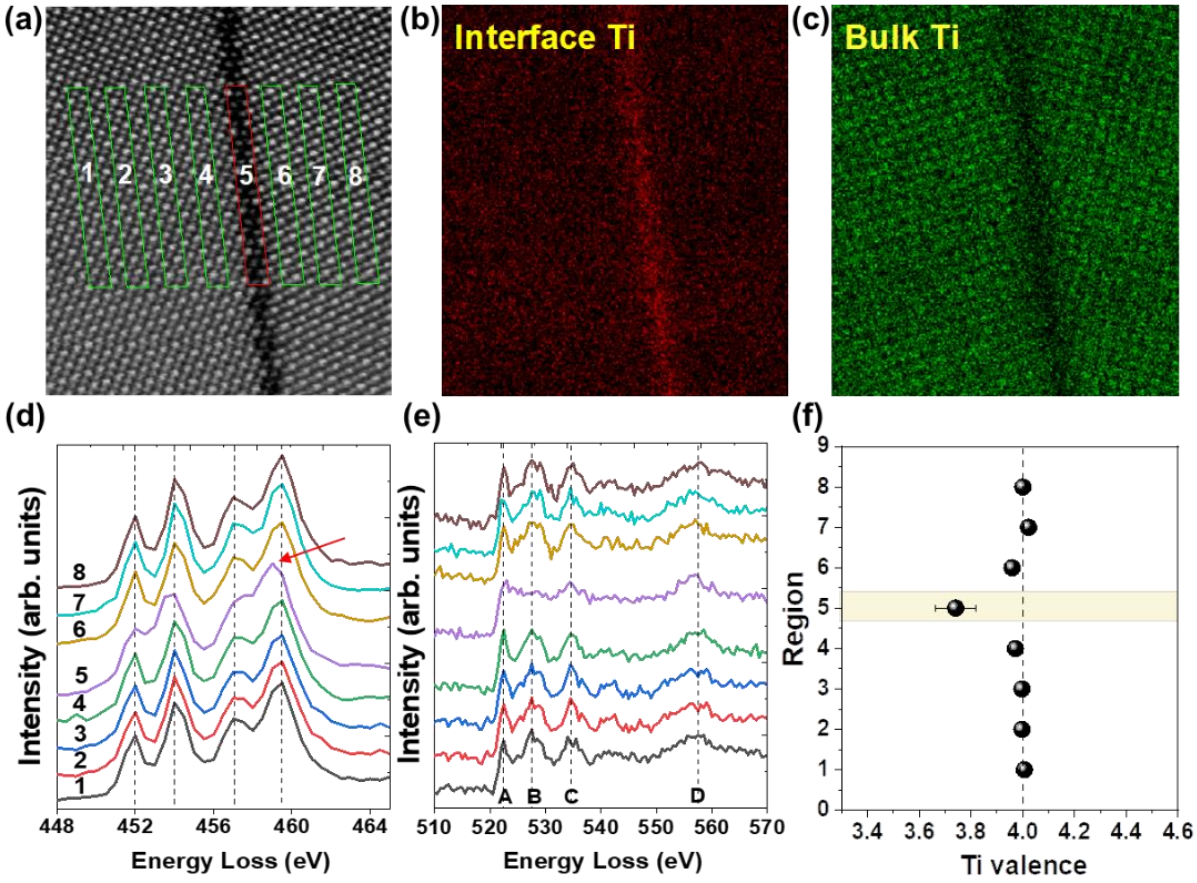

Figure 3.7 EELS measurements of the Ti-$L_{2,3}$ and O-*K* edges at the GB. (a) Assignment of areas in the ADF image for EELS data analysis. Mapping of (b) interfacial Ti and (c) Ti in the bulk. (d) Averaged Ti-$L_{2,3}$ white lines extracted from the regions marked in (a). (e) Averaged O-*K* edges extracted from the regions marked in (a). The letters A, B, C, and D assign the corresponding spectral features in the O-*K* spectra. The Ti-$L_{2,3}$ and O-*K* spectra extracted at position 5 are from the interface. (f) The valence states of Ti calculated by the multiple least-square fitting. The reference values for Ti^{3+} and Ti^{4+} are determined from bulk $LaTiO_3$ and bulk $SrTiO_3$, respectively.

3.3.3 The effects on the atomic electric field and charge characterization at the grain boundary

We conduct 4D-STEM experiments to further analyze the GB structure and electrostatic characteristics. For the 4D-STEM measurements, a pixelated detector records a 2D diffraction pattern at each probe position as the electron probe is scanned across the specimen, generating a 4D dataset. Fig. 3.8(a-c) shows the reconstructed ADF, BF, and ABF images, respectively. Therefore, we calculated the DPC image (Fig. 3.8(d)) using the py4DSTEM python library,[93] which shows higher contrast of the oxygen columns. It is sensitive to the beam deflection by detecting the center of mass of the electron intensity distribution. The atomic structure of the GB core in the reconstructed phase image is consistent with that in conventional ABF images (Fig. 3.5), but with better contrast of the oxygen columns. In addition to the missing oxygen columns, partial occupancy of the oxygen columns resulting in oxygen vacancies and structural distortions cause a slight decrease in contrast. Owing to the excess Ti and oxygen vacancies, the GB is positively charged, which is expected to induce negative space charge zones.[72]

To gain insight into the electric field in the GB region, we performed calculations based on the simplified quantum mechanical model of formula 2.20.[44, 66] Theoretical and simulation studies pointed out that the sample thickness should be less than 5 nm for quantitative atomic electric field measurements.[44, 94] However, due to sample preparation, such thin samples can hardly be regarded as bulk-like, since the regions near the surface (a few nanometers) are always non-stoichiometric. Therefore, we selected regions with a thickness of around 10-20 nm, which will give qualitative results of the electric field.[95] It would be more accurate to perform the measurements of atomic electric fields under the condition that the electron probe is focused on the midplane or below the midplane of the specimen.[95] We performed the experiments with different focusing conditions. First, the constructed images in Fig. 3.8 were recorded in an under-focus condition. The intensity bars in the atomic electric field maps indicate the relative intensity. From the magnitude of the average momentum transfer in Fig. 3.8c, we calculate the magnitude of the electric field (Fig. 3.8e) and the corresponding quiver plot (Fig. 3.8f), where the length and direction of the black arrows indicate the magnitude and direction of the electric field, respectively. From Fig. 3.9, the sample thickness for this region is about 16 nm by comparing the experimental and simulated CBED patterns. Generally, the electric field surrounding the cation columns points radially outward and appears approximately rotationally symmetric in the bulk region. At the GB, however, the fields are no longer radially symmetric and the field strength changes significantly compared to the bulk region.

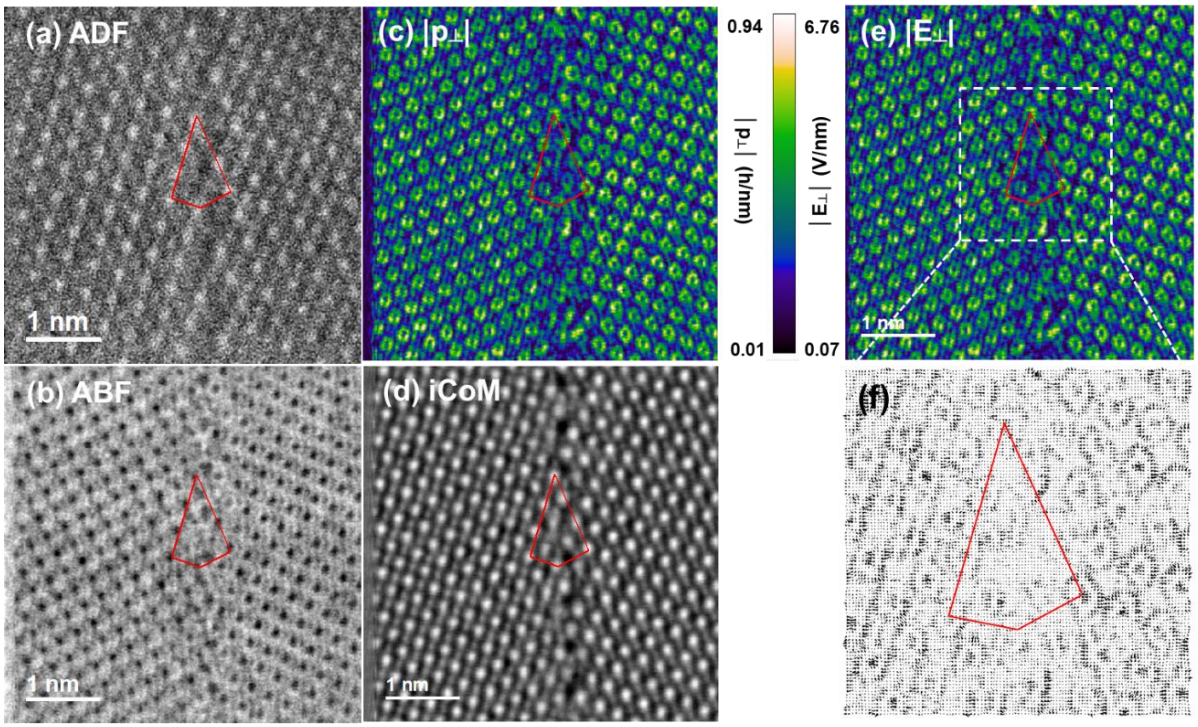

Figure 3.8 The extracted information from a 4D dataset of a Σ5 GB in STO. The electron probe is in an under-focus condition. Reconstructed atomic-column-resolved (a) ADF, and (b) ABF by virtual detectors. (c) The magnitude of the average momentum transfer around the GB. (d) The reconstructed iCoM image based on the py4DSTEM library. (e) Electric field derived from the average momentum transfer. (f) The corresponding quiver plot of the electric field from the region marked with a white dashed box in (e), characterizing its strength and rotational symmetry.

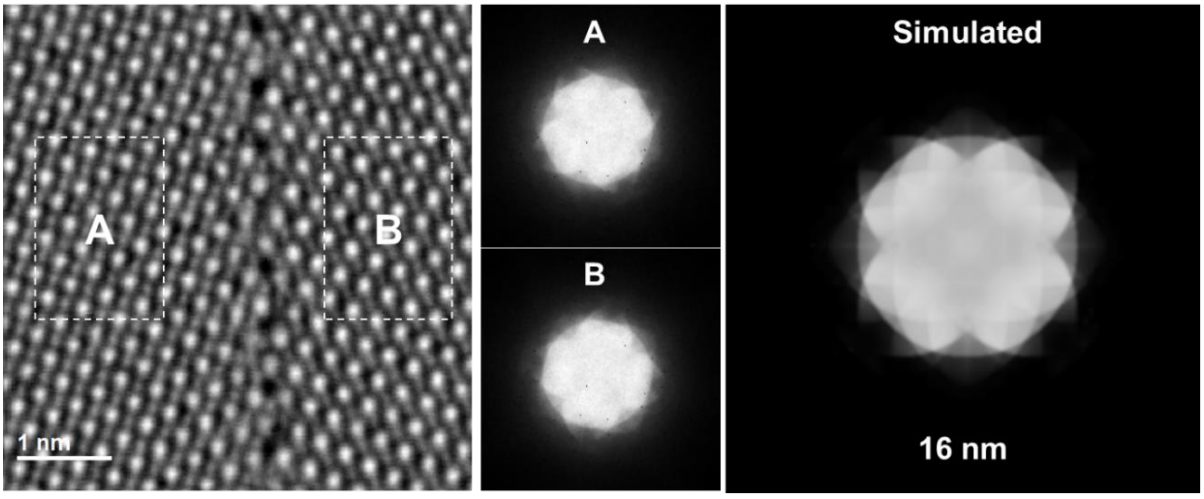

Figure 3.9 The experimental PACBED patterns extracted from the left and right grains in the area marked with white boxes in the iCoM image. The simulated CBED pattern calculated by the JEMS software.

As shown in Fig. 3.9, we find a very small tilt for the two adjacent grains by comparing the CBED pattern or the oxygen columns at the bulk region from the iCoM image, which would contribute to a change in the symmetry of the atomic electric fields at the grain boundary.

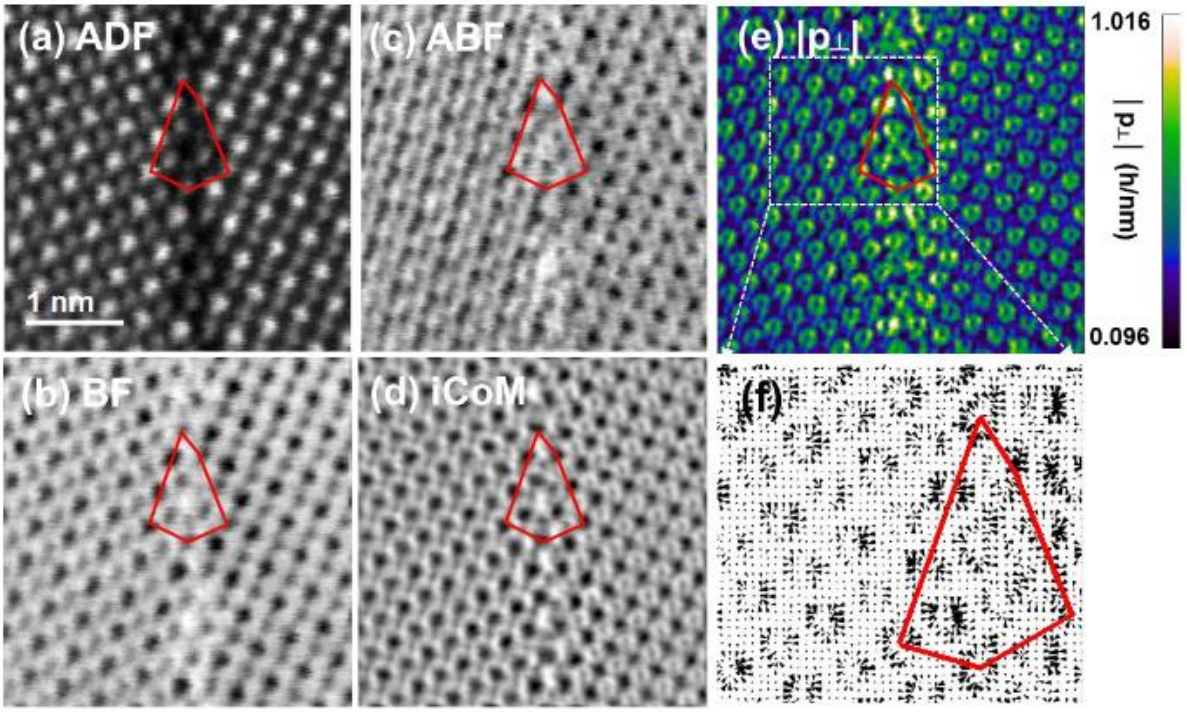

Figure 3.10 The extracted information from a 4D dataset of a Σ5 GB in STO. The electron probe is focused on the entrance surface of the sample. Reconstructed atomic-column-resolved (a) ADF, (b) BF, and (c) ABF by virtual detectors. (d) The reconstructed iCoM image based on the py4DSTEM library. (e) The magnitude of the average momentum transfer around the GB. (f) The corresponding quiver plot of the average momentum transfer from the region marked by the white dashed box in (e), characterizing its strength and rotational symmetry.

As shown in Fig. 3.10, we notice that the strength of momentum transfer at the grain boundary is much stronger than that in the bulk region when the electron probe is focused on the entrance surface of the sample. The obvious difference in the momentum transfer under different focusing conditions indicates the non-negligible effects of the diffraction contrast on the atomic electric field. Additionally, the simulated CoM images with different focusing conditions are shown in Fig. 3.11. Fig. 3.11b shows the supercell for a simulation obtained from the GB core structure proposed in Fig. 3.5. Fig. 3.11c, d, and e correspond to the CoM images for the conditions, where the electron probe is focused on the entrance surface, midplane and exit surface of a 16 nm sample, respectively. We found that the effect of the diffraction contrast on the magnitude of the CoM image at the grain boundary cannot be ignored, even without considering charge effects. When the probe is focused on the sample surface, the magnitude of the center of mass near the nucleus is weak and reverses direction compared to when the probe is in-focus or under-focus at the bulk region. This effect is more pronounced at the grain boundary. Therefore, we believe that it is difficult to distinguish the purely geometrical and charge effects by atomic electric field mapping at the grain boundary. However, the grain boundary is expected to be positively charged

considering the accumulation of positively charged defects, e.g., oxygen vacancies and reduced Ti atoms.

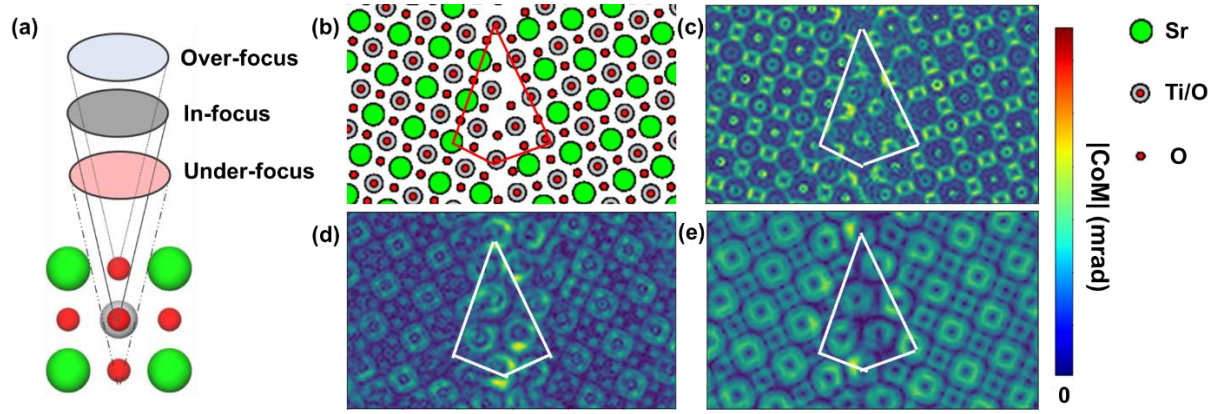

Figure 3.11 Simulation of COM imaging with different focus conditions. (a) Schematic representation of different focus conditions. (b) Supercell of the simulation where the electron probe is focused on the (c) entrance surface, (d) midplane, and (e) exit surface.

3.3.4 Nano-scale electrostatic field mapping across the grain boundary

According to the principle of electrical neutrality, the accumulation of positive charges at the GB should be compensated by a negative charge on both sides of the GB. According to the double Schottky barrier model of space charge formation, the negative charge formed in the bulk region can compensate for the positive charge at the GB core. In order to verify this, we analyze the electric field on a larger scale, as shown in Fig. 3.12, which shows an ADF image constructed from the 4D dataset (Fig. 3.12a) and the corresponding electric field image (Fig. 3.12b). Compared to the atomic electric field, the large scale electric field measurements are less sensitive to thickness, e.g., the momentum transfer can be averaged over a part of the crystal, where the momentum transfer derived from the atomic fields can be compensated due to symmetry.[94] The *x*-component of the electric field across the grain boundary in Fig. 3.12b shows a distinct difference, while the *y*-component of the electric field maintains almost homogeneous contrast of the whole region as shown in Fig. 3.12c. According to the double Schottky barrier model in Fig. 3.12e, the corresponding electric field (Fig. 3.12f) and charge density (Fig. 3.12g) line profiles can be obtained from the Poisson equation. The experimentally measured result in Fig. 3.12d is in good agreement with the double Schottky barrier model, suggesting that the positive charge accumulated at the GB core is compensated by a negative charge in the bulk region. In addition to the properties of the GB itself, the imaging of the electric field on a larger scale can be affected by other factors. Typically, a variation in sample thickness can cause a significant change in the measured electric field.[44] Therefore, we carefully selected an area of homogeneous thickness for our measurements.

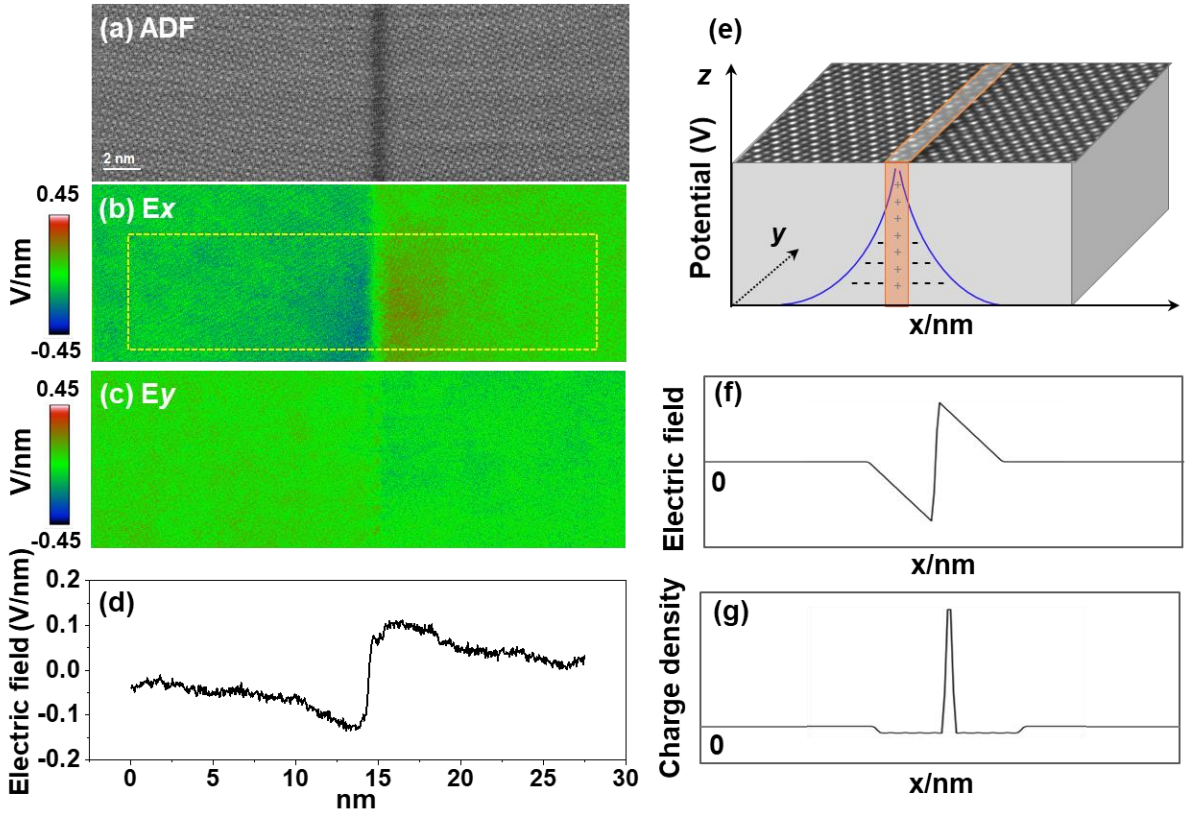

Figure 3.12 Electrostatic characteristics of the Σ5 GB at a larger scale. (a) ADF image of the GB. Corresponding (b) E*x* horizontal direction and (c) E*y* vertical direction of the electric field derived from the 4D data set. (d) Line profile of the electric field across the GB. (e) Schematic diagram of the double-Schottky-barrier model with a positive potential at the GB. (f) Corresponding electric field and (g) charge density profiles from the electrostatic potential in the double-Schottky-barrier model.

As shown in Fig. 3.13, the bulk region adjacent to the GB is almost flat from the line profile of the ADF image across the grain boundary. Besides, the weak contrast at the GB in the ADF image could in principle be due to a thickness difference between the GB and the bulk region. Therefore, we measured an EELS thickness map across the GB (Fig. 3.14), which confirms a uniform thickness across the GB.

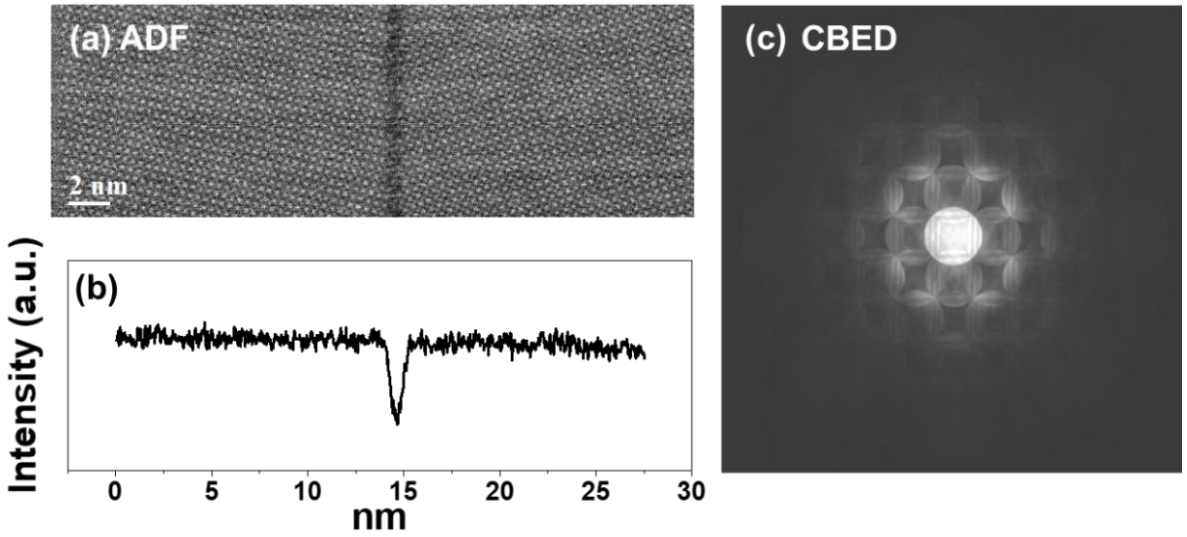

Figure 3.13 (a) ADF image contrast from the 4D-STEM dataset and the corresponding vertically averaged line profile (b). (c) CBED pattern averaged the entire region in the ADF image with a convergence angle about 6 mrad.

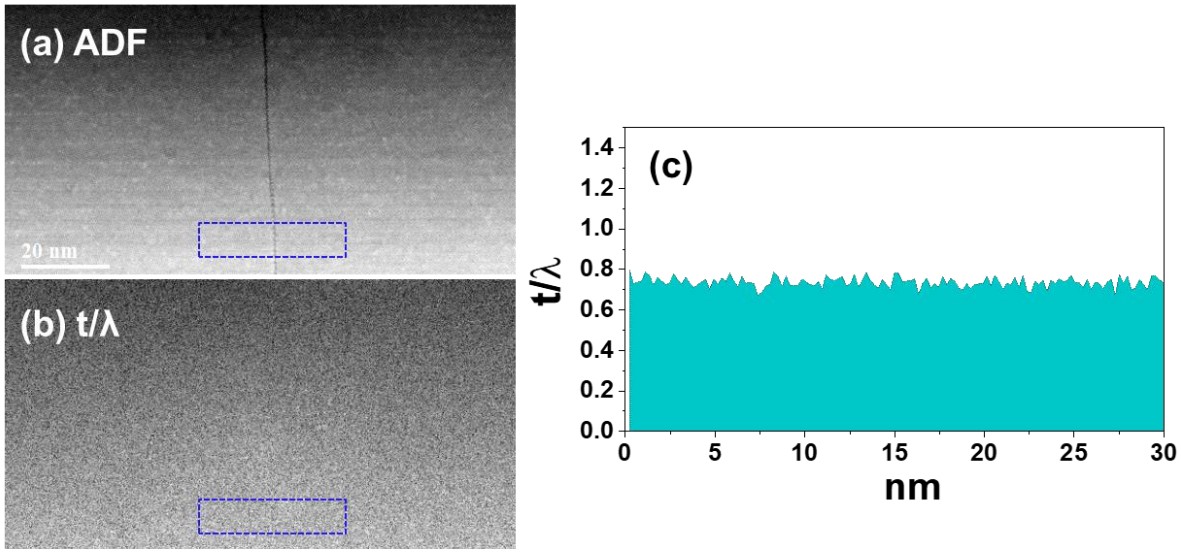

Figure 3.14 An EELS measurement across the GB. (a) The ADF image for the acquired EELS data. (b) Thickness map t/λ. (c) Vertically averaged thickness line profile of the region marked by the blue dashed box in (b).

3.3.5 Discussions

From the electric field maps, we can comprehensively identify the electrostatic characteristics of the GB. From the local atomic electric field maps, we observe a difference in electric field for the individual atomic columns around the GB core. The contributions to the measured electric field at the grain boundary include a decrease in Ti valence, accumulation of cations, charged defects, and a change in diffraction contrast. In principle, a decreased Ti valence at the GB can lead to a higher electric field due to an increase of electrons outside the nucleus. However, by changing the focusing condition, we find

that a variation of diffraction contrast due to structural disorder and lattice defects affects the measured atomic electric field, obscuring the information from charge effects. The observed asymmetric distribution of the measured electric field around the atoms is related to the atomic structure of the GB. On the one hand, the distorted and incomplete oxygen octahedra in the grain boundary core indicate a structural disorder along the *z*-direction, which easily leads to an asymmetric field distribution around cation atoms. The electrostatic discontinuity at the GB could drive the distortion of the adjacent oxygen octahedra, e.g., polar distortion, and antiferrodistortive distortion. The antiferrodistortive phase is normally stabilized at low temperatures in $SrTiO_3$, while it has been shown that it can be manipulated by GB engineering.[84] Furthermore, due to the close proximity of O atoms in the GB core, we observe a rigid body translation of 0.05 nm along the <310> GB plane, which contributes to the asymmetric field distribution. With respect to the nanometer-scale electric field, we can obtain more general information about the electrostatic properties of the GB by averaging over larger regions. We verify that a negative space charge in the bulk region compensates for a positive charge accumulated at the GB core, most likely caused by a reduced number of oxygen vacancies in this space charge region. This is in good agreement with the double Schottky barrier model. Thus, a simultaneous characterization of the atomic structure and the atomic and µm-scale electrostatic characteristics is beneficial to understand the relationship between the atomic structure and the electrostatic properties of the GB.

According to the double Schottky barrier model, the space charge layer width calculated from the impedance spectroscopy data is much wider than the GB width. For example, the space charge layer width of a $SrTiO_3$ bi-crystal doped with a few hundred ppm Fe is in the range of 30-70 nm with a space charge potential of about 0.6 V,[75, 96] whereas the space charge layer width should be even larger for undoped $SrTiO_3$.[72] In this work, we provide evidence for positive charge accumulation in the GB core and a space charge layer adjacent to the GB. The width of the space charge layer appears to be smaller than that measured by impedance spectroscopy. This could be related to the uncertainty of the doping level in our sample. Another reason for this discrepancy could be the limited sensitivity of the electric field measurements in the TEM. This could lead to the invisibility of the long tail of the space charge potential far from the GB, resulting in an apparently narrow zone.

3.4 Summary

In summary, we have systematically investigated the atomic structure and electrostatic characteristics of a high-angle Σ5 GB in a $SrTiO_3$ bicrystal by combining 4D-STEM and atomically resolved STEM-EELS. We show that mainly Ti occupies most of the atomic sites in the GB core with a small amount of Sr intermixing. The accumulation of cations and charged defects, e.g. oxygen vacancies, the reduction of Ti, and the structural distortion lead to the observed variation of the local electric field. The overall electrostatic properties of the GB are in agreement with the double Schottky barrier model, revealing that the negative charge originates from a space charge in the bulk to compensate for the positive charge in the GB core.

Contributions to this chapter:

Part of the chapter has been published in Ref.[97-98] Chao Yang designed and performed this work with the help of Yi Wang (MPI-FKF). Chao Yang wrote this chapter. Yi Wang (MPI-FKF) contributed to data processing. Wilfried Sigle (MPI-FKF) contributed to the theoretical discussion. Peter A. van Aken

(MPI-FKF) and Yi Wang (MPI-FKF) supervised this work. Rotraut Merkle (MPI-FKF) and Hongguang Wang (MPI-FKF) provided helpful discussions. Ute Salzberger (MPI-FKF) prepared the TEM samples. Samir Hammoud (MPI-FKF) carried out the ICP-OES measurements. Kersten Hahn (MPI-FKF) and Peter Kopold (MPI-FKF) helped with the TEM measurements. All authors discussed and contributed to the results.

Chapter 4 Ruddlesden-Popper fault in $NdNiO_3$ thin films

4.1 Introduction

The recent discovery of nickel-based superconductors fills the gap of nickel-based oxide materials in superconducting systems[16-17, 99-101]. The infinite layer phase $NdNiO_2$ (NNO2) can only be synthesized from the precursor ABO_3 perovskite structure by removing apical oxygen atoms from NiO_6 octahedra by topotactic reduction[102]. To stabilize the superconducting phase, chemical doping with divalent Sr replacing trivalent Nd is crucial. Optimal doping with the highest superconducting transition temperature around 15 K has been found in $Nd_{0.8}Sr_{0.2}NiO_2$ thin films[16]. During pulsed laser deposition growth of Sr-doped $NdNiO_3$ (NNO3) thin films, a strong tendency to form RP faults has been reported.[17] Besides, the epitaxial strain from the substrate can induce formation of Ruddlesden-Popper (RP) faults.[103-104] These RP faults exhibit an atomic structure, where the inclusion of an additional AO layer breaks the long-range order of the ABO_3 perovskite phase.[99, 103-112] Since the microstructure of the entire film determines its electrical properties, the investigation of the defect structure and associated variations in the local electronic structure in nickelates is essential. Moreover, RP structures are related to a variety of physical and chemical properties, e.g. electro-catalytic activities[112], microwave dielectric performance[113], magnetic[114] and ferroelectric properties[115].

Epitaxial strain and/or a cation non-stoichiometry, e.g. an excess of A or B in the ABO_3 structure, can induce the generation of different RP faults consisting of an intergrowth of rock-salt-type and perovskite-type building blocks[112, 116-118]. A single rock salt layer can be described as an $a/2\langle 111\rangle$ or $a/2\langle 110\rangle$ stacking fault, which exhibits a zigzag arrangement of cations.[110] The $(AO)(ABO_3)_n$ RP structure forms, when a rock salt layer separates the n-layer structure of $n(ABO_3)$.[105, 119-120] Detemple *et al.*[107] reported three-dimensionally arranged RP faults in $LaNiO_3$-$LaAlO_3$ superlattices, where the authors observed identical contrast of A and B columns in the ABO_3 structure in high-angle annular dark-field (HAADF) scanning transmission electron microscopy (STEM) investigations. Coll *et al*[119] identified multiple configurations of RP faults in a $LaNiO_3$ film based on atomistic modeling, experimental HAADF-STEM investigations, and HAADF image simulations. Bak *et al*[112] demonstrated a strong tetragonal Jahn-Teller distortion of the RP fault plane in $LaNiO_3$, proving a correlation between the octahedral distortion and the electrocatalytic performance of La-based perovskite oxides. However, to the best of our knowledge, the influence of different RP fault types on the variation of the electronic structure and especially the Ni valence state has not been reported for NNO3 thin films.

Here, we characterize the local atomic structure of different RP fault configurations and focus on the electronic properties around RP faults in the NNO3 film based on advanced aberration-corrected scanning transmission electron microscopy (STEM) and electron energy loss spectroscopy (EELS). RP-fault formation starts after a critical thickness of around two unit cells above the substrate-film interface, where different RP fault types are found to be inhomogeneously distributed throughout the film. We identify elemental intermixing in different RP-fault regions with different structural configurations. Besides, we show that the variation in Ni oxidation state around different RP faults is related to the change in chemical composition, possibly induced by epitaxial strain.

4.2 Specimen preparation

The NNO3 film was grown on a $SrTiO_3$ (001) single crystal substrate at 630 ^oC in an ozone-oxygen atmosphere at a pressure of 1.8×10^{-5} Torr by an atomic-layer-by-layer fashion in a custom-made ozone-assisted MBE setup. It was then cooled down after the growth in the same atmosphere. The fluxes of the effusion cells were calibrated with a quartz crystal microbalance prior to growth and monitored during growth by in-situ reflection high-energy electron diffraction.

The TEM sample was prepared by automated tripod polishing (Allied MultiPrep System) until the sample was thinner than ~15 μm, after which Ar ion milling was performed at liquid N_2 temperature using an ion polishing system (PIPS, Gatan, model 691). The milling step was performed at a voltage of 0.5 kV to reduce damage to the sample surface. We used a spherical aberration-corrected microscope (JEOL JEM-ARM200F, JEOL Co. Ltd.) equipped with a DCOR probe corrector (CEOS GmbH) and a Gatan GIF Quantum ERS with a Gatan K2 camera at 200 kV to acquire STEM images and EELS spectra. The convergence angle was set to 20.4 mrad and the collection semi-angles for high-angle annular dark-field (HAADF) and annular bright-field (ABF) imaging were set to 70-300 mrad and 10-20 mrad, respectively. The EELS spectra were acquired with a dispersion of 0.5 eV per channel (energy resolution of ~1 eV). The PCA method was utilized to optimize the signal and reduce the noise in the EELS maps.

4.3 Results and Discussion

4.3.1 Different types of Ruddlesden-Popper (RP) faults in $NdNiO_3$ thin films

As shown in the overview HAADF image in Fig. 4.1(a), the film thickness is around 9 nm, in good agreement with X-ray reflectometry, and a large number of RP faults are randomly distributed throughout the film. The critical thickness for RP-fault formation is around 2 to 3 unit cells. In this range, the film grows coherently with the substrate. Similar observations have been made and discussed in the reported result.[17] Above the critical thickness, defects are introduced to accommodate the strain. We note that this growth mode is similar to the Stranski-Krastanov mode, but differs in that it does not form islands on the coherent NNO3 layer, but instead forms a continuous film. According to the relation that brightness of the atomic columns is approximately proportional to $Z^{1.7}$ (Z: atomic number), a sufficient contrast difference allows us to distinguish the atomic columns.[121] For example, we observe a sharp interface between STO and NNO3. A high density of irregularly distributed RP faults generally forms three unit cells away from the substrate.

Although we cannot exclude non-stoichiometry during film growth as a reason for RP fault formation, a major driving force in our system is the reduction of lattice mismatch between STO (3.905 Å) and NNO3 (pseudocubic lattice constant: 3.807 Å), as we do not observe misfit dislocations that could alternatively reduce strain. In the enlarged HAADF image (Fig. 4.1(b)), several configurations of RP faults in the NNO3 layer are marked with red dashed boxes A, B and C, respectively. The apparent $a/2<110>$ shift for the RP fault A, where a is the lattice constant of the pseudocubic unit cell, is likely to be the component of the true displacement vector $a/2<111>$ projected along the beam direction.[120] The RP fault B shows a single intergrowth layer of $\{NdNiO_3\}$, forming a typical '214' structure of the RP phase (Nd_2NiO_4) by combining a rocksalt-type layer and a perovskite-type layer. In the case of the

RP fault C, the contrast difference between the A and B sites in NNO3 disappears due to the overlap of the A and B columns along the viewing direction[107, 119]. Additionally, the red dashed box D marks a fault-free region, displaying a perovskite structure of the NNO3 layer.

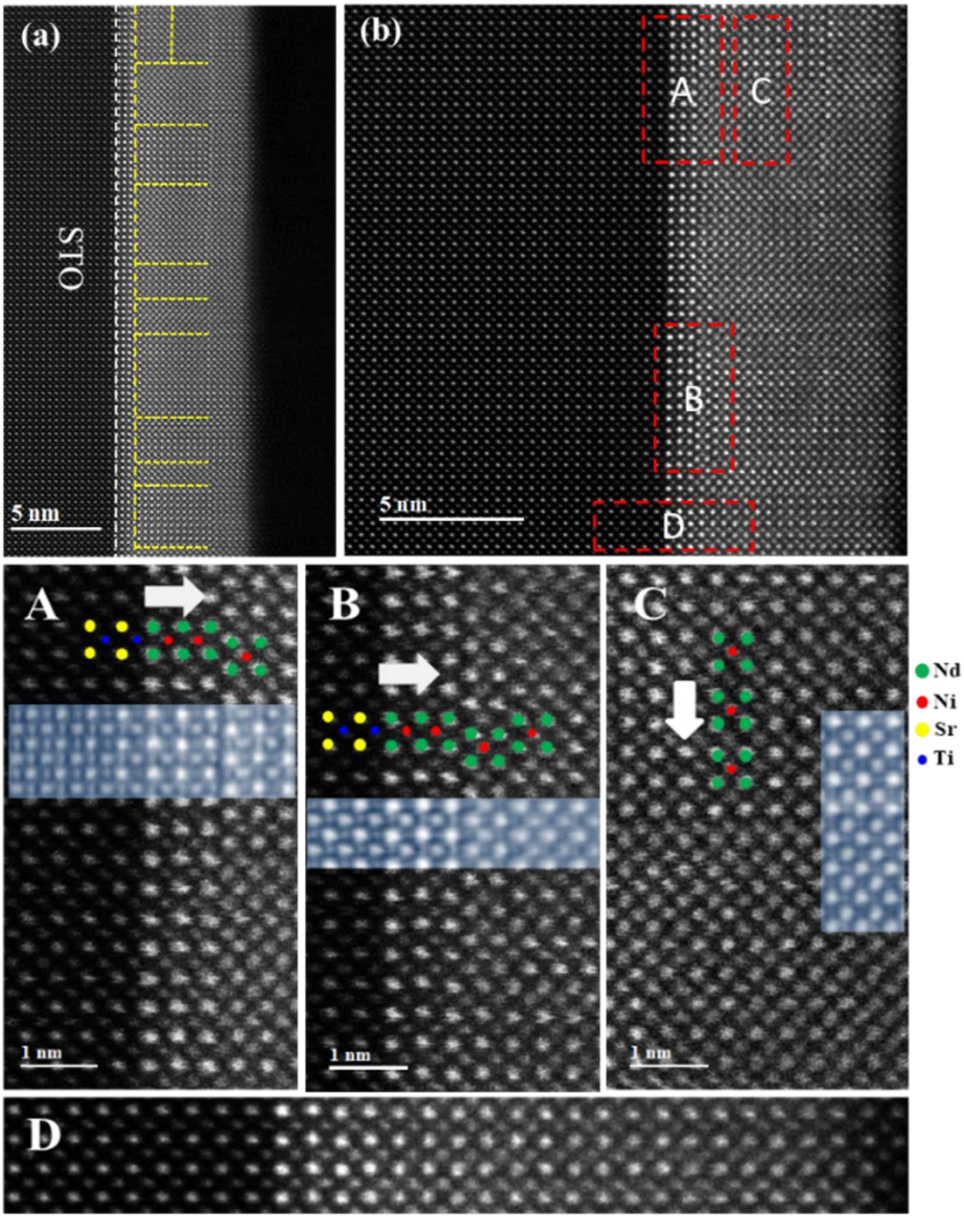

Figure 4.1 (a) An overview HAADF image of a $NdNiO_3$ film grown on a (001) $SrTiO_3$ single crystal substrate. (b) Enlarged image showing different types of RP faults and fault-free regions marked by red dashed boxes in the $NdNiO_3$ layer: (A) a/2 <111> shift; (B) single intergrowth layer of {$NdNiO_3$}; (C) identical contrast of A/B sites in $NdNiO_3$; (D) fault-free region. The contrast-inverted ABF images (shaded regions) show the oxygen columns around the RP faults.

Furthermore, we can observe the oxygen columns from the inverted ABF images (shaded in Fig. 4.1) around the edges of these RP faults. The slight elongation of Ni-O bonds along the *z*-axis at the plane of the RP fault A is evident (the enlarged inverted ABF images in Fig. 4.2b), which can lead to a

significant splitting of the e_g level of the Ni 3*d* orbital and a relative variation of the O 2*p* level based on the Jahn-Teller effect.[112] From a layer-by-layer structural perspective,[112] the distortion of oxygen anions toward the fault plane can reduce the strong repulsion between two $[NdO]^+$ layers and achieve an energetically favorable structure. Around the RP fault B, the elongation of Ni-O bonds is also visible, accompanied by a small distortion of $[NiO_6]$ octahedra (the enlarged inverted ABF images in Fig. 4.3b). The reduced contrast of the oxygen columns near the fault may be due to the presence of oxygen vacancies (Fig. 4.3b). Additionally, we observe distinct oxygen columns at the RP fault C without any obvious changes in the oxygen sub-structure. Owing to the overlapping of elements at the edge of the RP fault C, we observe a homogeneous distribution of oxygen.

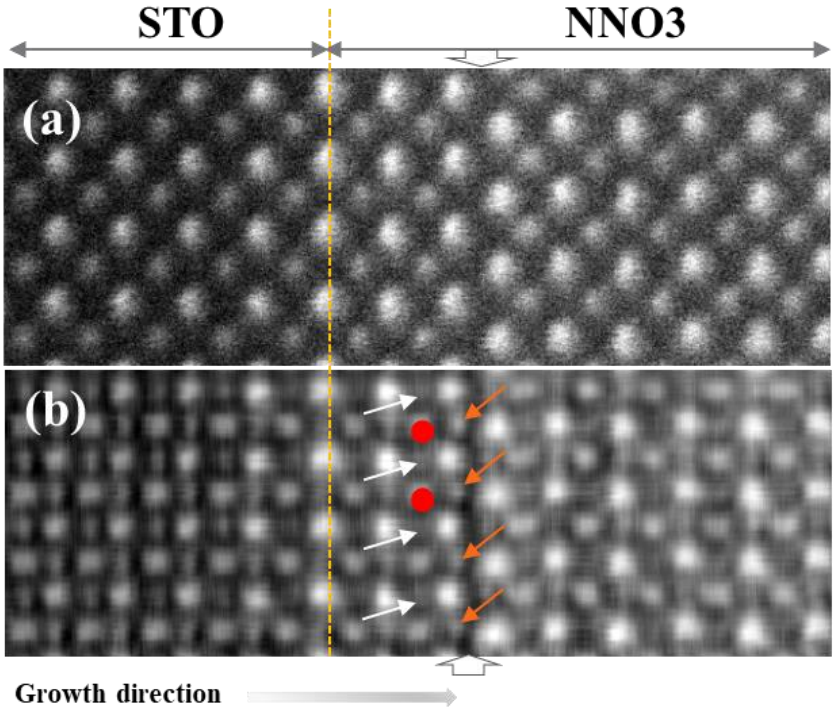

Figure 4.2 (a) HAADF and (b) inverted ABF images of RP fault A in a $NdNiO_3$ film grown on a (001) $SrTiO_3$ single crystal substrate. White arrows indicate basal O, and orange arrows represent apical O. Ni columns are marked by red circles.

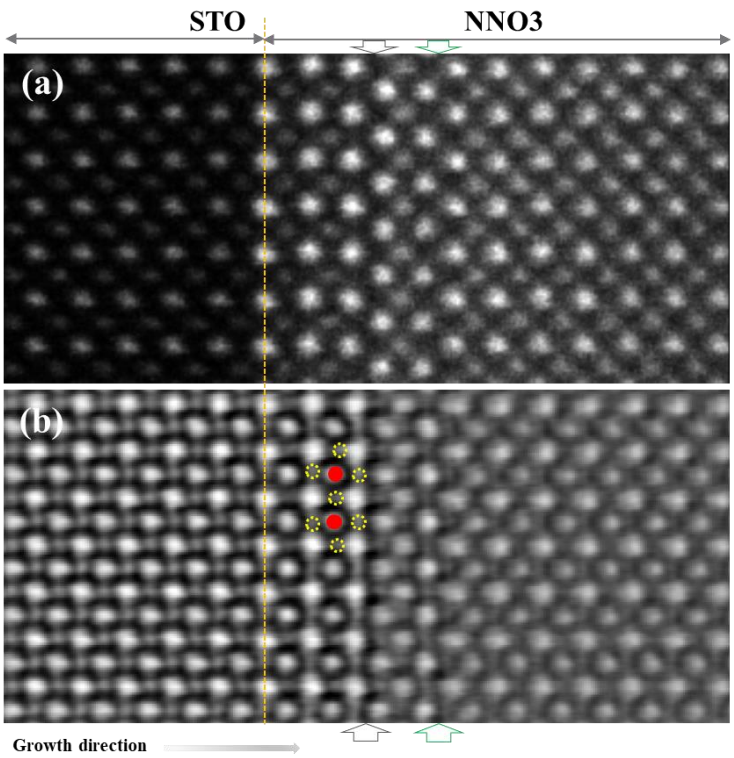

Figure 4.3 (a) HAADF and (b) inverted ABF images of RP fault B in a $NdNiO_3$ film grown on a (001) $SrTiO_3$ single crystal substrate. Yellow circles indicate O columns and red dots indicate Ni columns. White and green arrows indicate fault planes.

4.3.2 Elemental distribution at the RP faults

The atomically resolved EELS maps shown in Fig. 4.4 confirm the atomic arrangement around RP faults A and B in the NNO3 film. The distribution of cations from the color-coded EELS maps indicates elemental intermixing at the STO/NNO3 interface. In the RP fault regions, the zigzag arrangement of Nd atoms and the additional intergrowth of an NNO3 layer confirm the atomic structures visible in the ADF images. Fig. 4.4(a) shows the EELS maps of RP fault A, where Ni and Nd columns are clearly distinguishable. In the region of RP fault B, a small amount of Ni is intermixed with Nd. Owing to the random distribution of the RP faults, it is possible that the observed Nd/Ni signal intermixing is due to the partial overlap of Ni and Nd. Similarly, the apparent intermixing of Ni and Nd signals at RP fault C shown in Fig. 4.5(a) is due to Ni/Nd overlapping, which explains why the Ni and Nd columns have the same contrast in the ADF images. In addition, Ni $L_{2,3}$ and O K edges extracted from fault-free and Ni/Nd overlapping regions show the same shapes and peak positions.

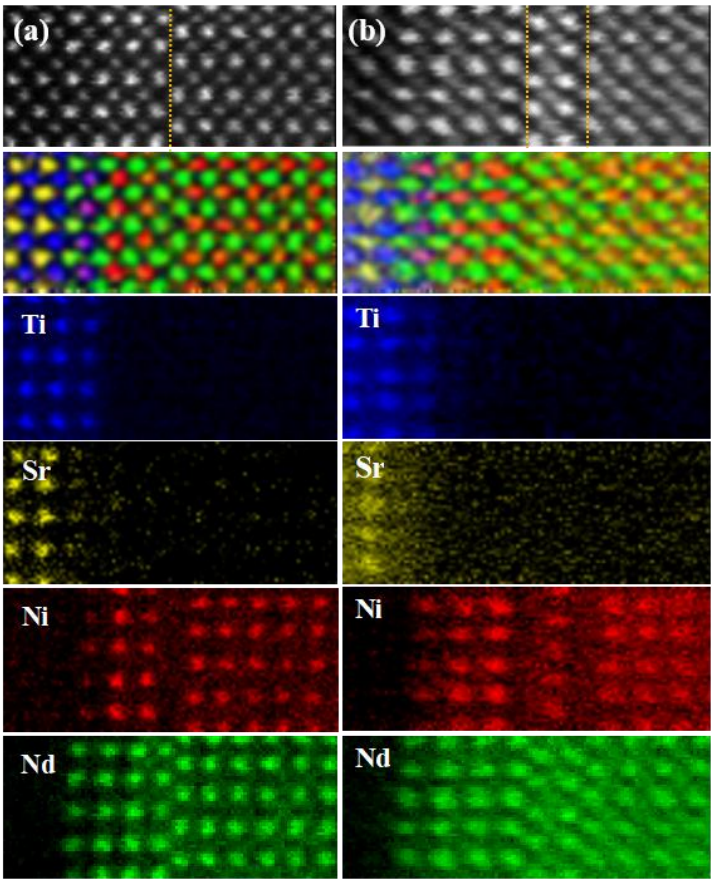

Figure 4.4 HAADF images of RP fault A (a) and B (b) in a $NdNiO_3$ film grown on a (001) $SrTiO_3$ single crystal substrate. Color-coded elemental maps of Ti (blue), Sr (yellow), Ni (red), and Nd (green) determined from an EELS spectrum image. The RP fault planes are marked with yellow dashed lines.

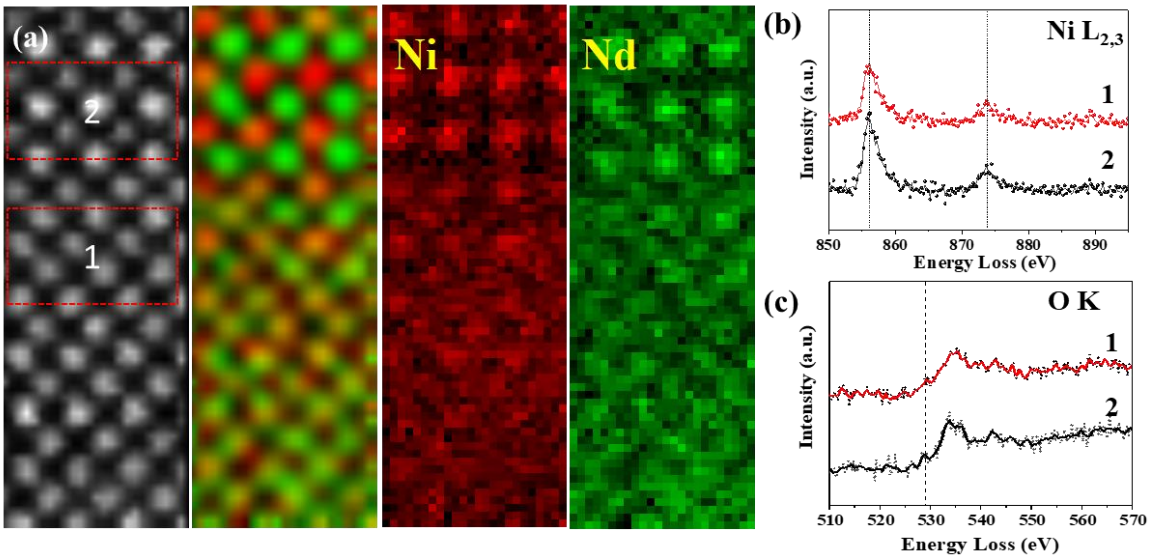

Figure 4.5 (a) HAADF image of RP fault C in a $NdNiO_3$ film grown on a (001) $SrTiO_3$ single crystal substrate and corresponding EELS maps of Ni (red) and Nd (green). (b) Ni $L_{2,3}$ edges and (c) O K edge extracted from regions marked by red dashed boxes in the HAADF image.

4.3.3 Electrostatic effects on the electronic structures in different RP faults

To investigate the effects of RP faults on the electronic character of the NNO3 film, we performed atomic resolution STEM-EELS measurements. Fig. 4.6(a) and (d) show the HAADF images of RP faults A and B, respectively. To improve the signal-to-noise ratio, the integrated O-K and Ni-$L_{2,3}$ edges were extracted from the red dashed boxes with 1-unit-cell-width as shown in Fig. 4.6(b) and (e). From the $NdNiO_3$ reference, we observe a strong pre-peak A at the O-K edge, which is associated with the hybridization of O 2*p* and Ni 3*d* orbitals, reflecting the covalency of Ni-O bonding and the oxidation state of Ni.[122-123] The pre-peak of the O-K edge is weak or even absent around the RP faults, which is related to the changes in local Ni-O distances due to epitaxial strain and RP faults.[122, 124] Besides, the strong Nd-O interaction in the rock salt layer results in a pronounced shoulder of peak C. Near the STO/NNO3 interface, the intermixing of Ti into Ni causes the appearance of peak B, which results from the Ti 3*d*-O 2*p* hybridized states. Peak B almost disappears in cells 4-7. Peak C corresponds to the O 2*p* states hybridized with Sr 4*d* in STO or Nd 5d in NNO3. Peak D is due to the O 2*p* states hybridized with Ni 4 *sp* and Nd 5*p* states.[125] The L_3 and L_2 peaks of Ni result from the excitation of electrons from the $2p_{3/2}$ and $2p_{1/2}$ core levels to the unoccupied 3*d* band, which is used to determine the valence state of the transition metal from the white-line ratio and chemical shift.[122] The slight variations in peak positions and crystal field splitting observed in Fig. 4.6(b) and (e) imply changes in the electronic structure of Ni for both types of RP faults. We quantified the white-line ratio, which is shown in Fig. 4.6(c) and (f). From the DigitalMicrograph database,[126] we calculated the Ni^{3+} and Ni^{2+} references corresponding to the fault-free NNO3 and NiO films. These are shown in Fig. 4.6(c) and (f) as black and blue dashed lines, respectively. We observe that the L_3/L_2 ratio increases near RP-fault planes and in the fault-free NNO3 layers near the STO substrate, indicating a decreased valence of Ni. In the fault-free NNO3 layer (7^{th} unit cell) away from the fault planes, the valence of Ni is close to 3+, as expected. The Ni L_3/L_2 intensity ratio in the RP fault B is slightly higher than that in the RP fault A, indicating a lower valence of Ni around the RP fault B.

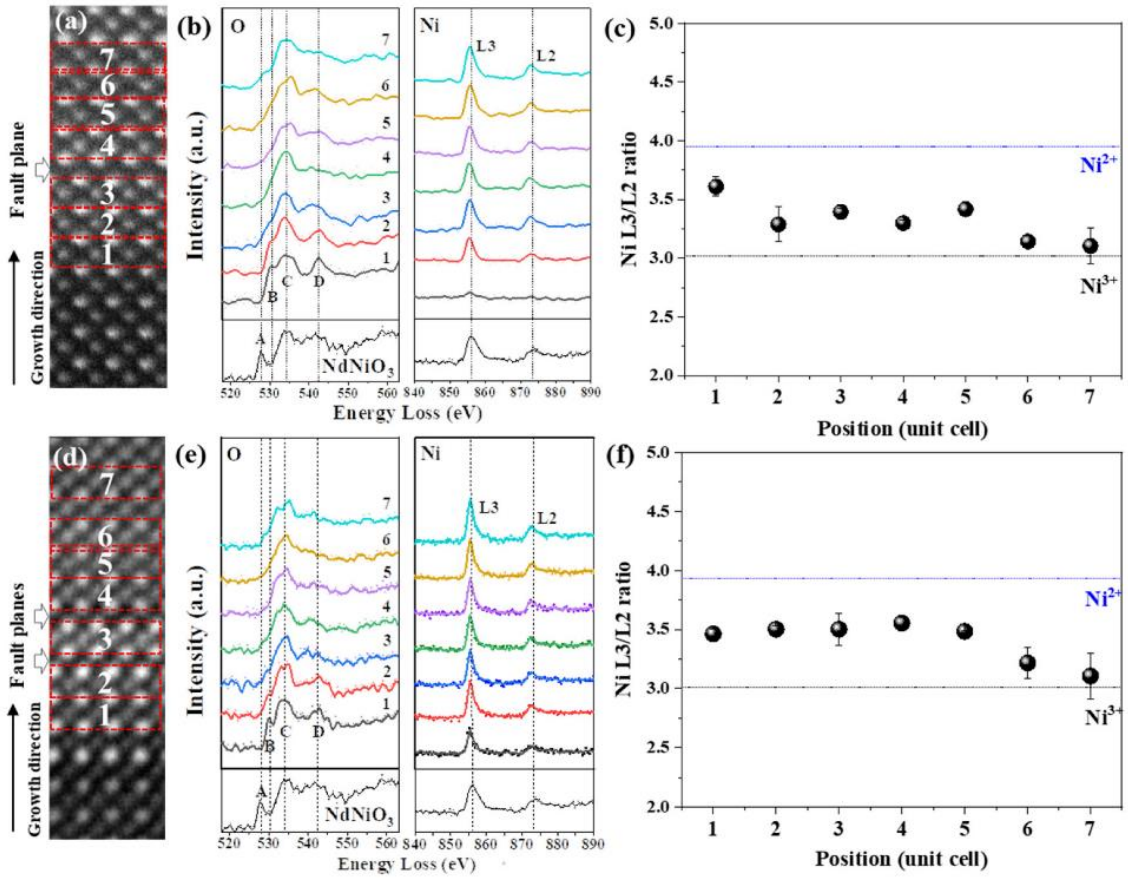

Figure 4.6 The HAADF images of (a) RP fault A and (d) RP fault B in a $NdNiO_3$ film grown on a (001) $SrTiO_3$ single crystal substrate used for EELS data acquisition. Atomic layers are numbered from 1 to 7. (b,e) O K and Ni $L_{2,3}$ spectra extracted from the red dashed boxes in the HAADF images of RP faults A and B, respectively. Spectral features are labeled with letters A-D (c,f) The calculated Ni L_3/L_2 white-line intensity ratios around RP fault A and RP fault B, respectively. The Ni^{3+} and Ni^{2+} references are from $NdNiO_3$ and NiO, respectively. The error bars were obtained by measuring different regions.

4.3.4 Strain effects at the RP faults

In order to explore the potential mechanism of the valence change of Ni, we quantitatively analyzed the variation of the lattice constant around RP faults A and B. Since the lattice constant of STO is slightly larger than that of NNO3, an in-plane tensile strain of ~2.5% is induced in the NNO3 film. From Fig. 4.7 (a) and (b), the critical thickness of the NNO3 layer is two unit cells. By calculating the Nd-Nd distance across the STO/NNO3 interface and across the RP fault plane from the HAADF images, we found that the in-plane tensile strain is maintained at ~2.5% for the first two-unit cells before the formation of RP faults. The in-plane Nd-Nd distance decreases to 3.85 ± 0.04 Å in the fault-free layers far away from the RP fault plane, as shown in Fig. 4.7(c) and (d). According to theoretical calculations, the O stoichiometry in NNO3 is sensitive to the in-plane tensile strain.[127] The formation energy of an oxygen vacancy becomes negative when the in-plane tensile strain is higher than 1.9%.[127] Therefore, the probability of oxygen vacancy formation near the interface is higher than that in the fault-free layers, where the in-plane strain is significantly released. Besides, oxygen vacancies are more easily formed in the NiO_2 plane, because their formation energy is about 1.7 eV lower in the NiO_2 plane than in the NdO

plane under tensile strain.[127] From the inverted ABF image in Fig. 4.2, we can clearly observe that the contrast of oxygen columns in the NiO_2 planes (marked with white arrows) is smaller than that in the NdO planes (marked with orange arrows), indicating the possible presence of oxygen vacancies in our sample. Thus, the strain-induced oxygen vacancies in the region near the STO/NNO3 interface may lead to a decrease in the Ni valence. In addition, the sharp decrease in the out-of-plane Nd-Nd distance to ~3.5 Å observed a few atomic columns away from the fault plane suggests a large out-of-plane contraction, which gradually increases to ~3.8 Å across the fault plane and into the fault-free region, as shown in Fig. 4.7(c) and (d). Therefore, the creation of RP faults effectively relaxes the epitaxial strain from the substrate, which is consistent with previous reports.[118]

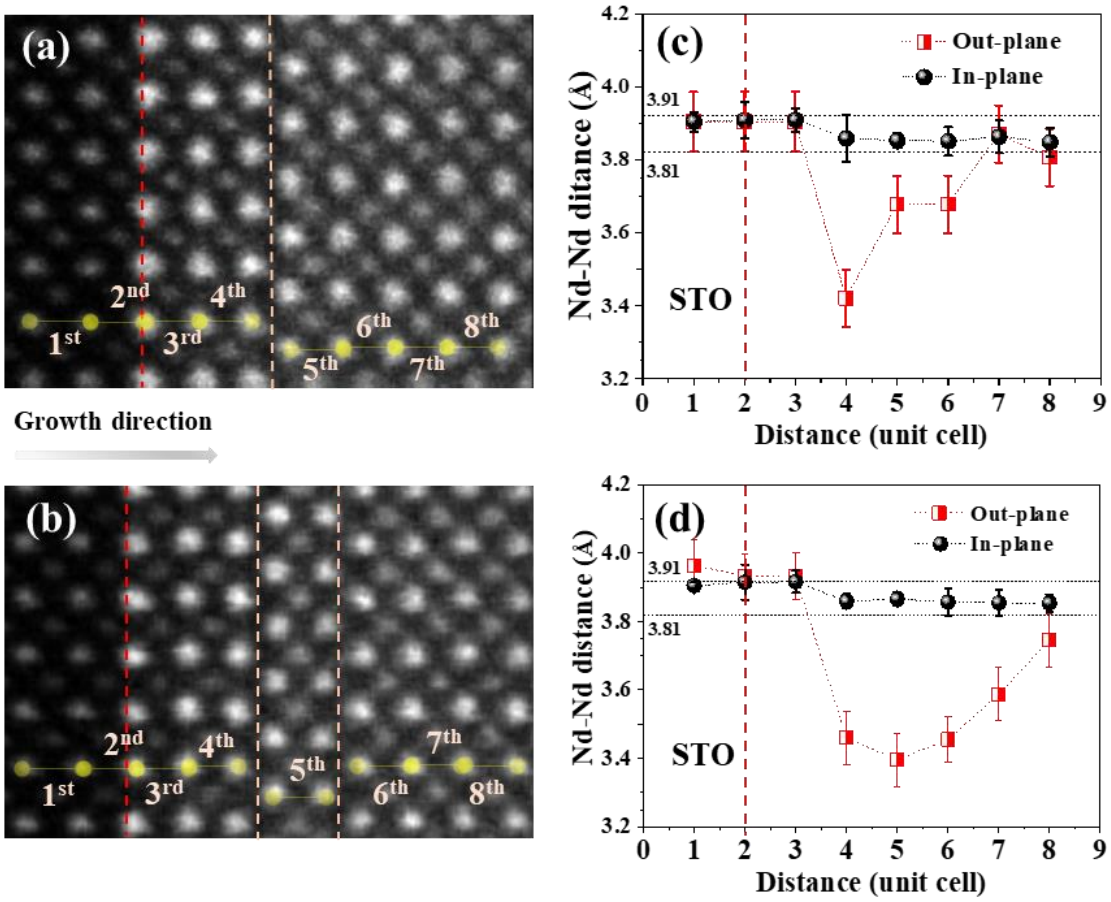

Figure 4.7 (a, b) HAADF images of RP fault A and B in the NNO3 film, respectively, used for quantitative analysis of Nd–Nd distances. The numbers indicate the positions of the unit cells. (c, d) The Nd–Nd distances along the in-plane and out-of-plane directions across RP fault A and B, respectively. The red dashed lines indicate the STO/NNO3 interface. The orange dashed lines mark the fault planes.

4.3.5 Discussion

The average oxidation state of nickel varies between 2+ and 3+ for different *n* in the RP structure ($Nd_{n+1}Ni_nO_{3n+1}$). In principle, Ni is divalent in the '214' end member of the RP structure (Nd_2NiO_4) as shown in Fig. 4.8a, where the $[NdO]^+$ layer donates an additional electron to the NNO3 layer.[128] However, the measured Ni valence in RP fault B shows a mixed valence between 2+ and 3+. The RP

fault B structure is similar to the Nd_2NiO_4 structure, but the $[NdO]^+$ layer is shared with adjacent NNO3 layers (Fig. 4.8b). The electrostatic discontinuity occurs at the fault plane, resulting in different structural and valence variations.

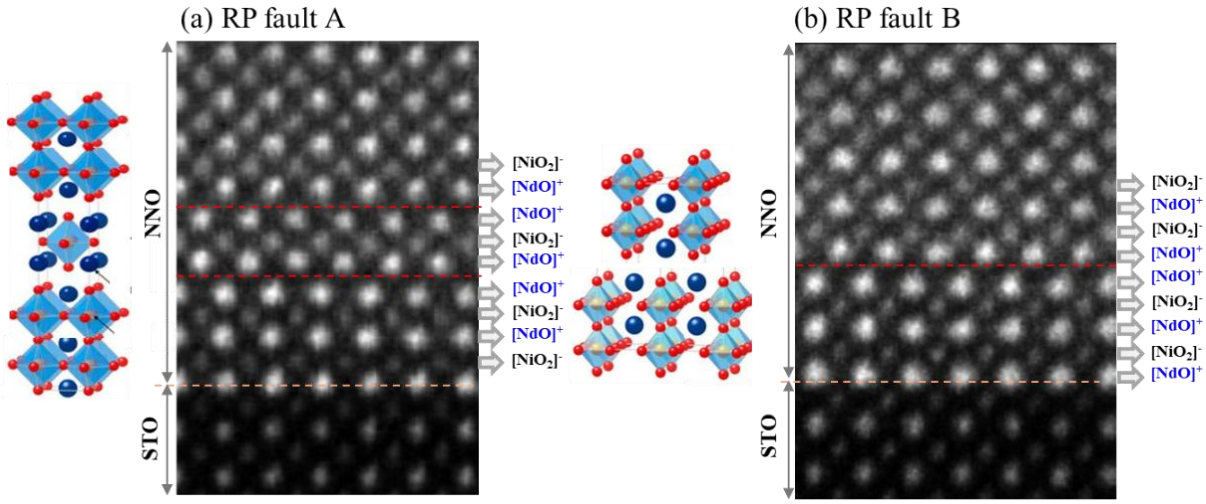

Figure 4.8 Electrostatic discontinuity at (a) RP fault A and (b) RP fault B, indicated by the red dashed lines. Yellow dashed lines indicate the $NdNiO_3$/STO interfaces.

We observe an irregular distribution of different types of RP faults and fault-free NNO3 layers in Fig. 4.1(b). As mentioned above, at the NNO3 layer close to the substrate, the tensile strain can induce the formation of oxygen vacancies, which means that the extra electron can be partially compensated by oxygen vacancies in the adjacent NNO3 layer. Thus, the Ni valence can be higher than 2+ in the intergrowth layer of NNO3. Given that the Ni/Nd signal intermixing occurs at the intergrown layer of NNO3, it is possible that the measured Ni signal partially arises from the fault-free NNO3 layer, which can also lead to a mixed Ni valence in RP fault B. With respect to RP fault A, there is no obvious elemental intermixing and the Ni ions show a higher valence (closer to 3+) than in RP fault B. The variation in Ni oxidation state is mainly attributed to the additional NdO layer and the possible oxygen vacancies.

4.4 Summary

Based on STEM and EELS measurements, we systematically studied the atomic structure of RP faults and the effects of RP faults on the local electronic configuration of Ni in a $NdNiO_3$ film. Several RP faults are detected, showing, e.g., $a/2<111>$ shifts, intergrowth layers of $NdNiO_3$, and overlapping Nd and Ni columns. The critical thickness for RP fault formation is around 2 unit cells and no misfit dislocations are visible. The generation of a high density of RP faults effectively relaxes the epitaxial strain from the substrate. We observed an elongation and distortion of the oxygen sublattice around the RP fault planes, which is theoretically beneficial to reduce the strong repulsion between two adjacent $[NdO]^+$ layers. We analyzed the variation of Ni oxidation state around RP faults in NNO3. The altered valence of Ni around RP fault planes is mainly related to the variations of strain and atomic structure. On the one hand, the tensile strain could induce oxygen vacancies in the fault-free layer of $NdNiO_3$ near the substrate. On the other hand, the additional $[NdO]^+$ layer may lead to a reduced valence of Ni at the

RP fault regions. This work demonstrates how the distribution of strain and atomic structure changes around RP faults, leading to a spatially varying electronic configuration in $NdNiO_3$.

Contributions to this chapter:

This chapter has been published in Ref.[129-130] Chao Yang conceived and performed this experiment with the help of Yi Wang (MPI-FKF). Chao Yang wrote this chapter. Yi Wang (MPI-FKF) contributed to data processing. Daniel Putzky (MPI-FKF) and Roberto A. Ortiz (MPI-FKF) grew the nickelate samples under the supervision of Gennady Logvenov (MPI-FKF), Bernhard Keimer (MPI-FKF), and Eva Benckiser (MPI-FKF). Wilfried Sigle (MPI-FKF) and Hongguang Wang (MPI-FKF) provided helpful discussions on the EELS measurements. Peter A. van Aken (MPI-FKF) and Yi Wang (MPI-FKF) supervised this work. The work in this chapter was supported in sample preparation by Ute Salzberger (MPI-FKF) and in TEM by Kersten Hahn (MPI-FKF) and Peter Kopold (MPI-FKF).

Chapter 5 Interface polarity in infinite layer nickelate superlattices

5.1 Introduction

Complex oxide superlattices provide a powerful platform for tuning the interactions between charge, spin, orbital and lattice degrees of freedom. By reducing the individual layer thicknesses to a few atomic layers and repeating them successively in a superlattice structure, structural and electronic interface reconstructions can dominate the macroscopic properties[131-133]. An effective approach to modify interfacial properties in complex oxide heterostructures is to tune the oxygen octahedral structure, charge transfer, electronic confinement, magnetic exchange interactions, and so on. For example, thickness-dependent oxygen octahedral rotations in $NdNiO_3/SrTiO_3$ superlattices significantly affect the metal-insulator transition and the antiferromagnetic transition[134]. This is also strongly influenced by the oxygen stoichiometry. A polar discontinuity at the $NdNiO_3/SrTiO_3$ interface can lead to interface reconstruction, which induces the formation of oxygen vacancies. Besides the above-mentioned reconstructions, layer-selective topotactic reduction is another very interesting way to modify the properties. In topotactic reduction,[135-136] the formal electronic configuration of Ni changes from $3d^7$ to $3d^9$ by successive apical oxygen removal. Unconventional superconductivity was first observed in an infinite layer Sr-doped $NdNiO_2$ film[16] and later reproduced in $A_{0.8}B_{0.2}NiO_2$ (A: La, Nd, Pr; B: Ca)[16, 137-138] and a $Nd_6Ni_5O_{12}$ film[26], but no superconductivity has been found in bulk samples[18]. Some studies have investigated the role of interfacial properties and film geometry in superconductivity. For example, theoretical calculations have predicted the formation of a two-dimensional electron gas (2DEG) as a result of interface reconstruction at the polar $NdNiO_2/SrTiO_3$ interface[21, 139], similar to the polar $LaAlO_3/SrTiO_3$ interface.[5, 140-143] In principle, an abrupt interface between $[Nd]^{3+}$ and $[TiO_2]^0$ layers can induce a polar discontinuity, leading to a built-in electrostatic field that would result in a polar catastrophe. However, the occurrence of electronic and/or atomic reconstruction can avoid such polar instabilities. He *et al*.[22] verified by DFT calculations that an atomic reconstruction is energetically more favorable than electronic reconstruction and predicted an interfacial configuration with residual apical oxygen atoms as well as Ni displacements. A single intermediate $Nd(Ti,Ni)O_3$ layer was observed by atomic resolution EELS in a $NdNiO_2$ single film grown on a (001)-oriented $SrTiO_3$ single crystal, indicating that an atomic reconstruction at the polar interface mitigates polar instability[144]. In addition, superlattice structures have been proposed to introduce hole doping into their infinite layer stacks by interface engineering[145], offering the possibility of achieving superconductivity in nickelates without a disorder introduced by alkaline earth doping. This so-called superlattice approach relies on the ability to tune the doping level through the thickness of the infinite layer stack. While a first realization with $LaNiO_{2+x}/LaGaO_3$ interfaces turned out to be non-superconducting because holes are trapped at the interface[23], different atomic or electronic reconstructions at the $NdNiO_2/SrTiO_3$ interfaces offer different possibilities to tune the properties of the superlattices. For this purpose, detailed experimental investigations of oxygen octahedra and the stoichiometry at interfaces of the superlattice with atomic precision are essential.

In this work, $NdNiO_2/SrTiO_3$ superlattices with different stacking thicknesses were synthesized in two steps: (i) growing the perovskite phase of $NdNiO_3/SrTiO_3$ superlattices on a (001)-oriented $SrTiO_3$ substrate by PLD and (ii) reducing the samples by soft-chemistry topotactic reduction. Using 4D-STEM and atomically resolved EELS, we provide a detailed characterization of the oxygen structure and

concentration distribution as well as the electronic structure in $NdNiO_2$ (NNO2)/$SrTiO_3$ (STO) superlattices. We directly image the thickness-dependent variation of the oxygen concentration, revealing the reduction process in the NNO2 layer. Moreover, we discuss the spatial variation of atomic and local electronic structures across the interfaces in NNO2/STO superlattices. We found a gradual variation of the oxygen content from the interface to the inner part of the nickelate layer stack. Our results provide a picture of the special extension of reconstructions related to the polar interfaces, which is instructive for understanding the thickness-dependent properties of infinite-layer superlattices.

5.2 Specimen preparation

The $NdNiO_3$/$SrTiO_3$ superlattice samples were grown on a (001)-oriented single crystal $SrTiO_3$ substrate by PLD under the conditions reported in Ref.[145], followed by oxygen deintercalation through a gas-phase reaction with CaH_2 powder in a vacuum-sealed Pyrex glass tube operated in an Ar-filled glove box. The sealed Pyrex glass was heated in a standard oven at 280°C for at least four days. To avoid differences in samples grown separately, the samples were cut into four pieces, one of which was kept pristine and the rest was chemically treated. The TEM lamellae were prepared using a focused ion beam (FIB Scios, FEI) under high vacuum. Around 8 nm of carbon was coated on the surface of the sample using a high-vacuum sputter coater (EM ACE 600, Leica) to prevent beam-induced charging effects during sample preparation. The quality of the TEM lamellae was optimized by low-energy milling and cleaning in a Fischione NanoMill® TEM sample preparation system. TEM measurements were performed in STEM mode using a JEOL JEM-ARM200F microscope (JEOL Co. Ltd.) equipped with a DCOR probe corrector and a Gatan GIF Quantum ERS with a K2 camera. A condenser aperture of 30 μm was used for STEM imaging, and the corresponding convergence semi-angle was 20.4 mrad. The collection semi-angle range for HAADF imaging was between 83 and 205 mrad for a camera length of 2 cm. The collection semi-angle for EELS measurements was 85 mrad for a 5 mm aperture. The EELS spectra used for elemental mapping were acquired at a dispersion of 0.5 eV/channel with an energy resolution of around 1 eV. The EELS spectra used for the white-line ratio calculation were acquired at a dispersion of 0.25 eV/channel with an energy resolution of around 0.75 eV. With respect to the white-line ratio, we first denoise the EELS data by carefully using PCA in the DigitalMicrograph software. Then, we removed the background using a power-law model and calculated the cross-sections based on the Hartree-Slater model. Afterwards, we calculated the white-line ratio from the extracted integral L_3 and L_2 white-line intensities. 4D-STEM images were acquired with a Merlin pixelated detector (256 × 256 pixels, Quantum Detectors) in 1-bit mode with continuous reading/writing at a pixel time of 48 μs. Data analysis of the 4D-STEM datasets is based on the Python libraries py4dstem[93] and fpd[146].

5.3 Results and Discussion

5.3.1 Thickness-dependent oxygen deintercalation in $NdNiO_2$/$SrTiO_3$ superlattices

To study the atomic structure of the interfaces, we used the latest advanced 4D-STEM technique to image the oxygen sublattice and distribution at the interfaces, which gives a clear oxygen phase contrast image[97]. In Fig. 5.1, we compare the atomic structure of the interfaces in superlattices $4NdNiO_2$/$2SrTiO_3$ (SL_4_2) and $8NdNiO_2$/$4SrTiO_3$ (SL_8_4). Figure 5.1a and 5.1g are sketches of the interface structures of SL_4_2 and SL_8_4, respectively. It is well accepted that the apical oxygen in {NiO_6} octahedra can

be deintercalated more easily than the basal oxygen during a topotactic reduction process due to its lower Ni-O binding energy[34]. This has also been demonstrated by TEM experiments[17, 26, 138]. STO and NNO2 layers can be identified in the HAADF images for SL_4_2 (Fig. 5.1b) and SL_8_4 (Fig. 5.1h) by their clearly different mean internal potentials. As shown in the iCoM images of SL_4_2 (Fig. 5.1c) and SL_8_4 (Fig. 5.1i), the apical oxygen positions in the NNO2 infinite layer have a significantly reduced contrast compared to those in the basal oxygen columns. Thus, the apical oxygen in the NNO2 layer is partially deintercalated. Compared to the NNO2 layer, the basal and apical oxygen columns in the STO layer maintain the same contrast.

To understand the deintercalation process of oxygen ions and the variation of oxygen concentration in the NNO2 layer, we determined all oxygen positions by Gaussian fitting and then extracted the oxygen intensity map as shown in Figure 5.1d for SL_4_2 and Figure 5.1j for SL_8_4, where the red color denotes reduced oxygen contrast. The corresponding integrated intensity profiles of apical and basal oxygen are presented in Figures 5.1e, f (SL_4_2) and Figures 5.1k, l (SL_8_4), respectively. A small difference in the contrast of the basal oxygen between the NNO2 and STO layers is due to the different channeling conditions of the fast electrons along the oxygen columns. The oxygen intensity maps are normalized to the oxygen intensity in the STO substrate. It is worth mentioning that the intensity of the apical oxygen in the NNO2 layer for SL_4_2 (Figure 5.1f) gradually decreases from ~90% near the STO substrate to ~30% near the surface, reflecting that the chemical reduction process occurs from the surface to the substrate. The locally formed infinite-layer structure near the surface region in the nickelate layer indicates the formation of at most two unit cells of an NNO2 layer in SL_4_2 (see Figure 5.2). The apical oxygen intensity profile for SL_8_4 (Figure 5.1l) shows the variation of the oxygen contrast, revealing a gradual decrease of the apical oxygen concentration from the interface to the center of the NNO2 layer. We observed at most six unit cells of fully reduced NNO2 layers in the nickelate layer stacks in the 8_4 SL sample. The residual apical oxygen atoms are visible in the first NdO_x layer at the interfaces, which is beneficial to mitigate the strong polar discontinuity at the NNO2/STO interfaces by providing an extra electron to compensate for the built-in electrostatic field according to theoretical calculations[22, 147]. The observed residual apical oxygen columns toward the center of the NdO_x layer may also contribute to the suppression of the polar instability. In addition, we note that there is an asymmetric distribution of residual oxygen at the bottom and top interfaces, which may be related to the extent of elemental intermixing, since Ti intermixing into Ni sites increases the binding energy and hinders the removal of apical oxygen[144].

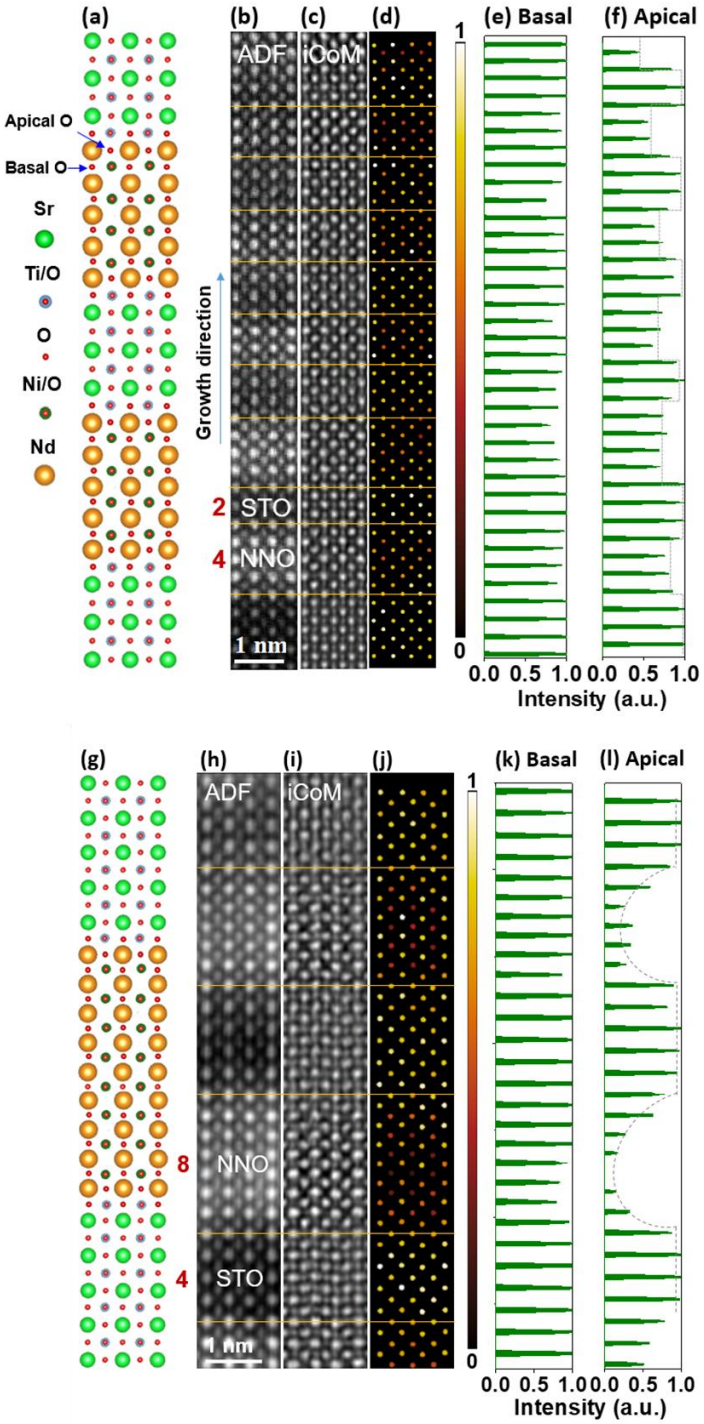

Figure 5.1 Oxygen distribution and occupancy in the $4NdNiO_2/2SrTiO_3$ (a-f) and $8NdNiO_2/4SrTiO_3$ (g-l) superlattices. (a) Schematic diagram of the atomic structure of the $4NdNiO_2/2SrTiO_3$ superlattice (b) ADF image and (c) iCoM image reconstructed from a 4D-STEM dataset for a $4NdNiO_2/2SrTiO_3$ superlattice. (d) Oxygen intensity map obtained from all oxygen columns in the iCoM image in (b) by Gaussian fitting. The corresponding integrated intensity profiles of (e) basal oxygen and (f) apical oxygen positions. (g) Schematic of the atomic structure of the $8NdNiO_2/4SrTiO_3$ superlattice. (h) ADF image and (i) iCoM image reconstructed from a 4D-STEM dataset for an $8NdNiO_2/4SrTiO_3$ superlattice. (j) Oxygen intensity map obtained from the iCoM image in (i). The corresponding integrated intensity profiles of (k) basal and (l) apical oxygen positions.

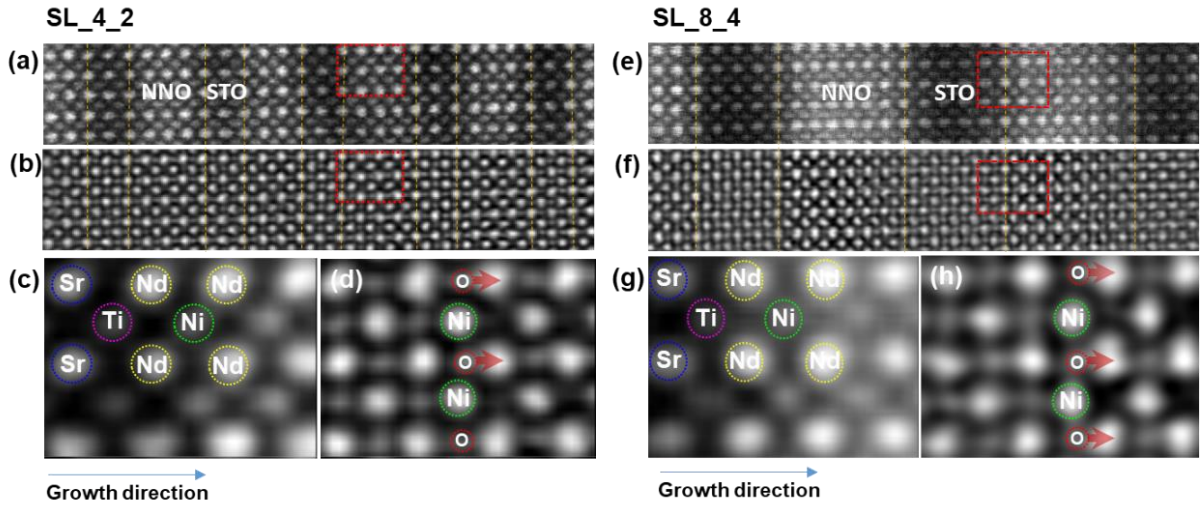

Figure 5.2 Distortion of oxygen octahedral at interfaces in $4NdNiO_2/2SrTiO_3$ and $8NdNiO_2/4SrTiO_3$ superlattices. (a) ADF image and (b) iCoM image reconstructed from a 4D-STEM dataset of a $4NdNiO_2/2SrTiO_3$ superlattice. The enlarged (c) ADF image and (d) iCoM image are from the region marked with red dashed boxes in (a) and (b), respectively. (e) ADF image and (f) iCoM image reconstructed from a 4D-STEM dataset of an $8NdNiO_2/4SrTiO_3$ superlattice. The enlarged (g) ADF image and (h) iCoM image are from the region marked with red dashed boxes in (e) and (f), respectively.

5.3.2 Elemental intermixing and residual oxygen distribution at the interface

In Figure 5.3, atomically resolved STEM-EELS chemical mapping identifies the chemical components and distributions across all interfaces in an 8 unit cell thick $NdNiO_2$ / 4 unit cell thick $SrTiO_3$ (8NNO2/4STO) superlattice (SL_8_4). The HAADF image in Fig. 5.3(a) shows the atomic structure of the NNO2 and STO layers. The corresponding elemental maps of the Sr-$L_{2,3}$ (b), Ti-$L_{2,3}$ (c), Nd-$L_{2,3}$ (d), and Ni-$L_{2,3}$ (e) edges and an RGB overlay (f) are shown in the right panel. Fig. 5.3(g) shows the enlarged HAADF image of the region marked by the white dashed box in Fig. 5.3(a) and the corresponding normalized intensity profiles of (h) Ni and Ti and (i) Nd and Sr, revealing the apparent elemental interdiffusion at the interfaces. The interdiffusion lengths of Ni/Ti and Nd/Sr amount to 1 ~ 2 unit cells on both sides of the interface. The cation intermixing is not homogeneous at different interfaces. For example, the Ni/Ti ratio is ~3 (Nd/Sr ratio of ~3) at interface A and ~1 (Nd/Sr ratio of ~0.95) at interface B in the NNO2 layer, indicating the instability of the interface structure. Nevertheless, the dominant interface configuration consists of a connection of a TiO_2-terminated STO surface and a NdO_x-terminated NNO2 surface, which is different from the reported single intermediate Nd(Ti, Ni)O_3 layer in the $NdNiO_2$-$SrTiO_3$ (substrate) interface, where the B-site cation is predominantly Ti with some Ni occupancy. From a layer-by-layer perspective, the former interface configuration of TiO_2-NdO_x-NiO_2-Nd is more polar.

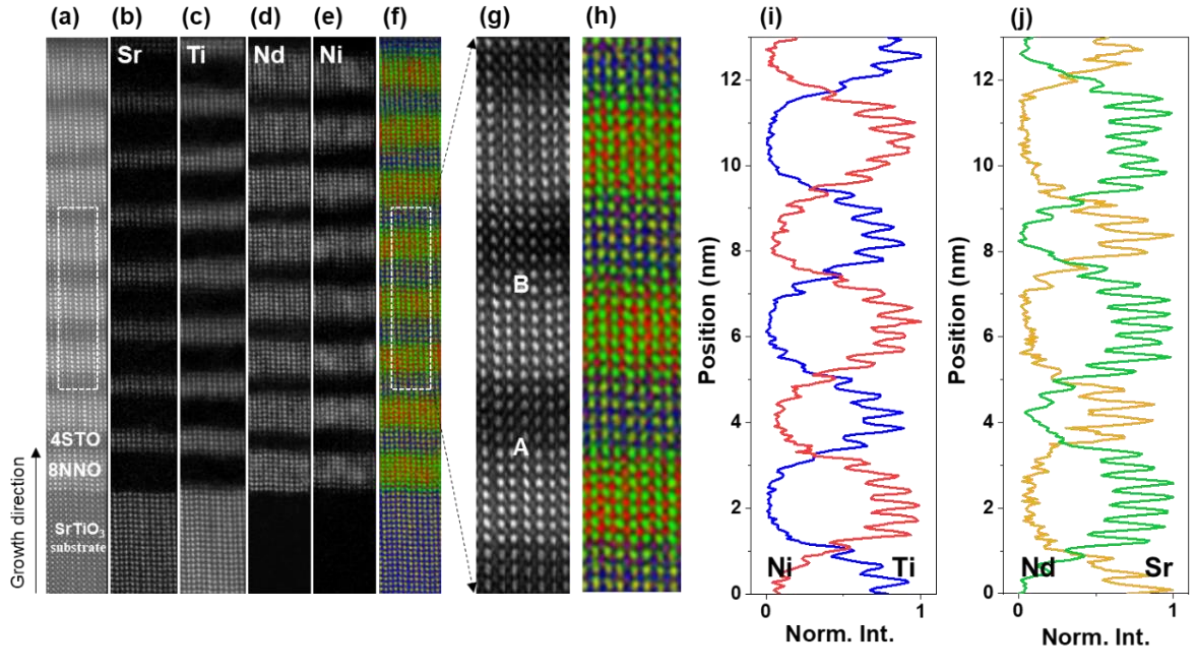

Figure 5.3 Elemental distribution across the interfaces of an $8NdNiO_2/4SrTiO_3$ superlattice. (a) An HAADF image for the acquisition of the EELS mapping across the film. EELS maps of (b) Sr $L_{2,3}$, (c) Ti $L_{2,3}$, (d) Nd $M_{4,5}$, and (e) Ni $L_{2,3}$ integral white-line intensities. (f) Color-coded map of Sr (yellow), Ti (blue), Nd (green), and Ni (red). (g) An enlarged HAADF image of the regions marked with a white dashed box in (a) and (f). (h) Color-coded map of Sr (yellow), Ti (blue), Nd (green), and Ni (red), and the corresponding normalized intensity line profiles of (i) Ni and Ti, and (j) Nd and Sr. Interfaces A and B marked in (g) show different degrees of elemental intermixing as shown in (i) and (j).

Similar interdiffusion lengths of cations and interface configurations occur in the short periodic 4NNO2/2STO superlattice (SL_4_2), as shown in Fig. 5.4. This results in the presence of Ni and Ti throughout the film and Nd in all STO stacking layers. In comparison, the interface between the substrate and the first NNO2 layer shows much less intermixing, indicating that the elemental intermixing forms during the growth of the perovskite phase. The cation intermixing is not affected by the chemical reduction process, which would mainly affect the oxygen ions. Since the reduction energy of Ti-O is higher than that of Ni-O[21, 148-149], the intermixing of Ti into Ni sites can promote oxygen intercalation in the NNO2 layer near the interfaces. A theoretical calculation predicted that the formation of residual oxygen in the first NdO layer can effectively avoid the polar instability resulting from the formation of a built-in electrostatic field at the polar interface[22].

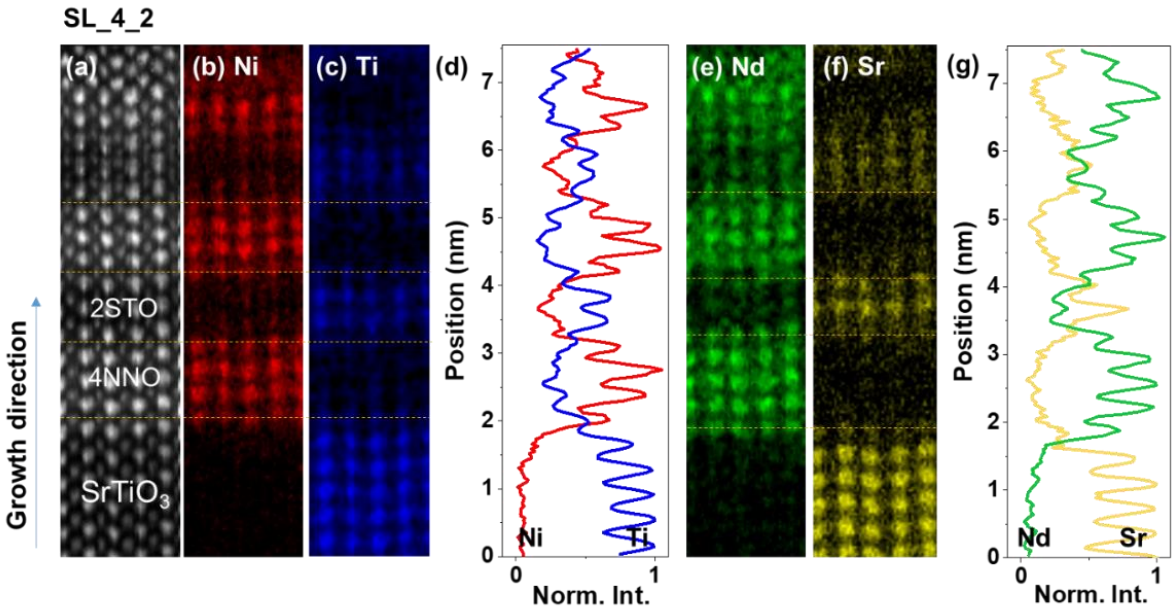

Figure 5.4 Elemental distribution across the interfaces of a $4NdNiO_2/2SrTiO_3$ superlattice. (a) An HAADF image for the acquisition of the EELS mapping. EELS maps of (b) Ni (red), (c) Ti (blue), (e) Nd (green), and (f) Sr (yellow). Normalized intensity line profiles of (d) Ni and Ti, and (g) Nd and Sr.

5.3.3 Thickness-dependent interface polarity and interface reconstruction

In order to study the evolution of the electronic structure affected by the residual oxygen atoms at the interfaces, we calculated the white-line ratios of Ni and Ti, respectively, resulting in their valence variation from the STO layer to the NNO2 layer, as displayed in Fig. 5.5. The detailed EELS spectra of the Ti-L, O-K, Ni-L and Nd-M edges are shown in Fig. 5.6 (SL_4_2) and Fig. 5.7 (SL_8_4). Figure 5.5a and 5.5d present the HAADF images of SL_4_2 and SL_8_4 regions used for the EELS measurements. The valence state of Ti intermixed into Ni sites in SL_4_2 tends to be 3+, while in SL_8_4 it is close to 4+ (Figure 5.5c and 5.5f). The valence of Ni varies between 1+ and 2+ as it depends on the extent of deintercalation of apical oxygen in the inner NNO2 layer. An apparent gradual variation of Ni valence is visible in the NNO2 layer for SL_8_4 as shown in Figure 5.5e, where the valence of Ni in the inner NNO2 layer tends to be 1+ and gradually increases to 2+ near the interfaces. The valence of Ni in SL_4_2 tends to be ~2+ in the NNO2 layer. The valence of Ni intermixed into the Ti sites in the STO layer is close to 3+.

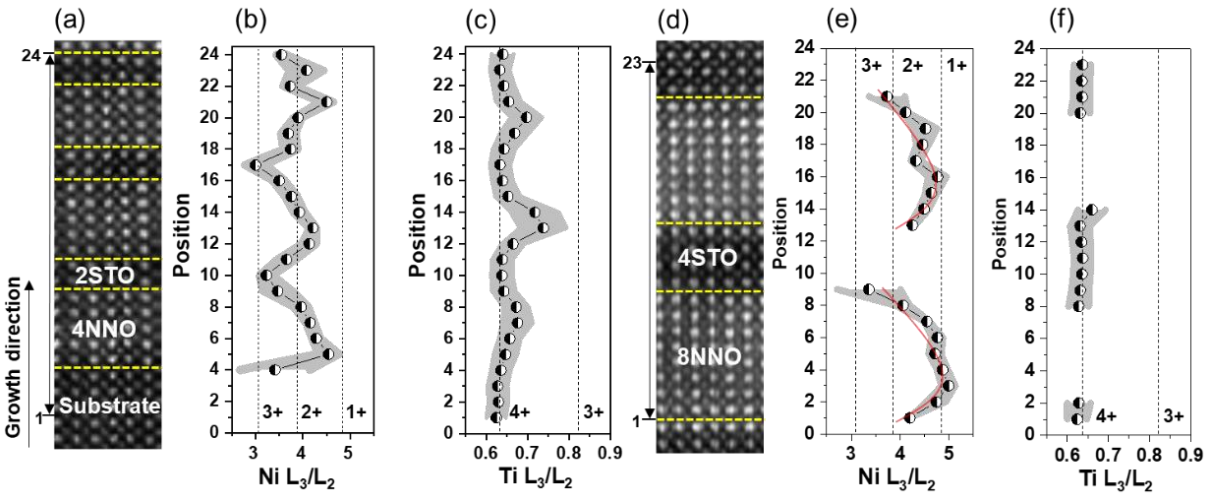

Figure 5.5 Valence variations of Ni and Ti ions across the interfaces in $4NdNiO_2/2SrTiO_3$ (a-c) and $8NdNiO_2/4SrTiO_3$ (d-f) superlattices. HAADF images of (a) $4NdNiO_2/2SrTiO_3$ and (d) $8NdNiO_2/4SrTiO_3$ superlattices. The L_3/L_2 white-line ratios of (b) Ni and (c) Ti in $4NdNiO_2/2SrTiO_3$ and of (e) Ni and (f) Ti in $8NdNiO_2/4SrTiO_3$ superlattices, respectively. The dashed reference lines for Ni^{3+}, Ni^{2+}, and Ni^{+} are determined from the L_3/L_2 white-line ratios of $NdNiO_3$, NiO, and $NdNiO_2$ films. The Ti^{4+}, and Ti^{3+} references are from $SrTiO_3$ and $LaTiO_3$[91-92], respectively.

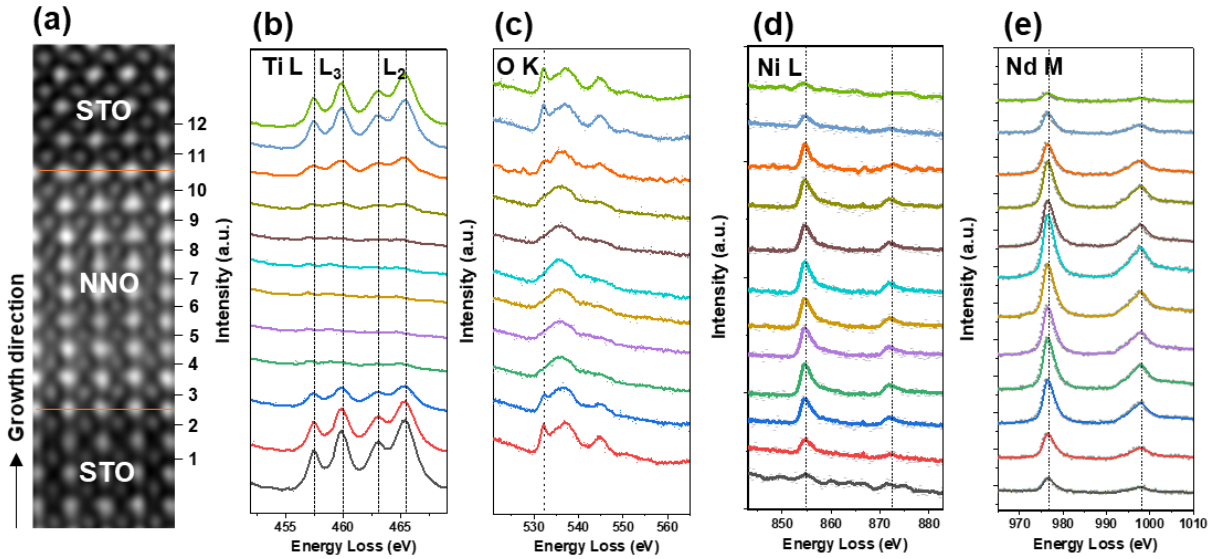

Figure 5.6 (a) An ADF image for EELS data analysis of the 8_4 SL sample. Corresponding EELS spectra of the (b) Ti-$L_{2,3}$ edge, (c) O-K edge, (d) Ni-$L_{2,3}$ edge, and (e) Nd-$M_{4,5}$ edge.

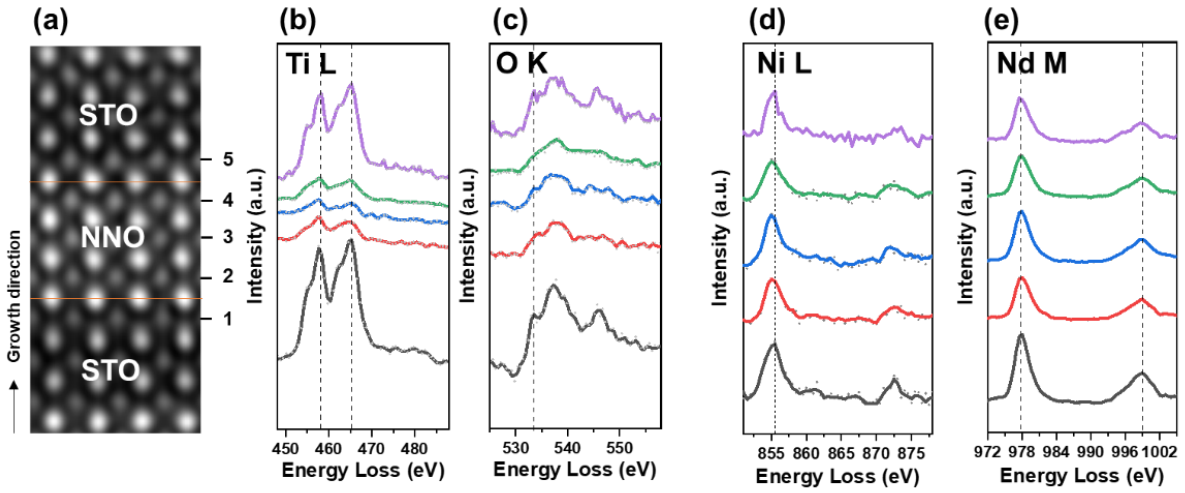

Figure 5.7 (a) An ADF image for EELS data analysis of the 4_2 SL sample. Corresponding EELS spectra for the (b) Ti-$L_{2,3}$ edges, (c) O-K edges, (d) Ni-$L_{2,3}$ edges, and (e) Nd-$M_{4,5}$ edges.

The reference value of the Ni-$L_{2,3}$ white-line ratio of Ni^{3+} is determined from a $NdNiO_3$ sample[129]. The Ni^{2+} reference is from a NiO film in the Gatan EELS database[126]. The Ni^{1+} reference is obtained from SL_8_4, because we can confirm that the infinite layer is formed in the NNO2 inner layer in the SL_8_4 sample according to the iCoM image in Fig. 5.1h. The EELS spectra of Ni-L references and the corresponding O *K* edges are shown in Fig. 5.8. According to the variations of the oxygen contrast in the iCoM images and the white-line ratios of Ni, we demonstrate that the oxygen distribution and occupancy are closely related to the valence variation of Ni ions.

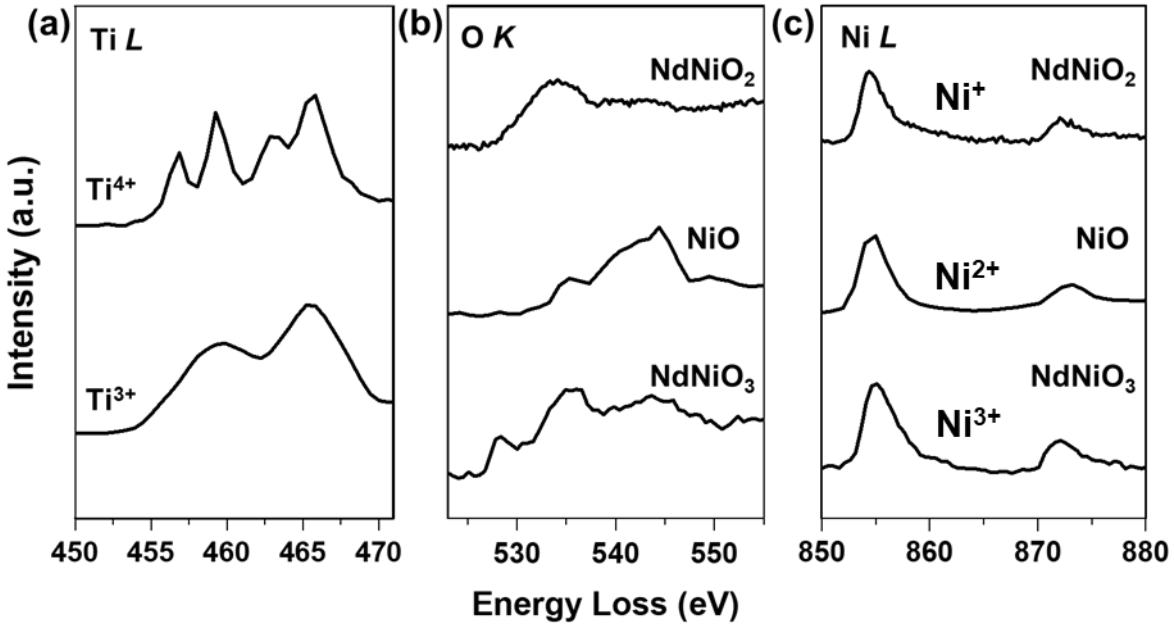

Figure 5.8 The reference EELS spectra for (a) Ti-$L_{2,3}$ of Ti^{3+} and Ti^{4+} (b) O-K, and (c) Ni-$L_{2,3}$ edges for Ni^{+}, Ni^{2+}, and Ni^{3+}.

Furthermore, we quantify the variations of the cation lattice spacings in SL_8_4 and SL_4_2 as shown in Figure 5.9. Figure 5.9a presents an HAADF image of SL_4_2 optimized by a multi-frame ADF-STEM method. Using Gaussian fitting and center-of-mass fitting based on a Python library of atomap[55], we calculate the in-plane and out-plane cation lattice spacings. In SL_4_2, the in-plane Nd-Nd spacing is around 0.391 nm, which is almost the same as in the STO substrate. In principle, the $NdNiO_3$ film (lattice spacing: 0.381 nm for a pseudo-cubic unit cell) grown on a STO (a = 0.3905 nm) substrate is under epitaxial tensile strain. The in-plane lattice spacing of the bulk $NdNiO_2$ is 0.392 nm and the c-axis lattice parameter is 0.331 nm[135]. The $NdNiO_2$ film is reported to experience epitaxial compressive strain from the STO substrate[16]. The out-of-plane lattice spacing in a $Nd_{0.8}Sr_{0.2}NiO_2$ film is about 0.334 nm from XRD measurements, which has a larger c-axis lattice parameter than the $NdNiO_2$ film due to partial substitution of Nd by the larger Sr ion[17]. This implies a possible smaller out-of-plane lattice spacing than 0.334 nm in a $NdNiO_2$ film. A smaller decrease to ~0.376 nm of the out-of-plane Nd-Nd spacing occurs in SL_4_2 than the above value after the chemical reduction. The observed residual oxygen and elemental intermixing in the NNO2 layer can suppress the decrease of the out-of-plane lattice spacing. As depicted in Figure 5.9b, there is a sharp decrease in the out-of-plane Nd-Nd spacing to ~0.330 nm in SL_8_4, which is slightly smaller than the value reported from XRD measurements in a $Nd_{0.8}Sr_{0.2}NiO_2$ film[17], suggesting the formation of an NNO2 infinite-layer structure. Additionally, a gradual decrease in the out-of-plane Nd-Nd spacing is related to the variation of oxygen occupancies from the interface to the NNO2 inner layer. Since the interdiffusion length between STO and NNO2 layers is only within 2 unit cells, the variation of out-of-plane lattice spacing is mainly attributed to the variation of the residual oxygen concentration. Besides, the in-plane Nd-Nd spacing remains the same as that of the STO substrate. Due to the residual oxygen near the interfaces, there may be no compressive strain at the STO/NNO2 interfaces, while the NNO2 inner layers are likely to be under a small compressive strain. Another point is that there is a significant extension of the out-of-plane lattice spacing to about 0.4 nm between the last SrO layer and the first NdO layer at partial interfaces, which is in agreement with a reported NNO2 single film grown on a STO substrate[144]. This is related to the proportion of Ni/Ti intermixing according to DFT calculations[144].

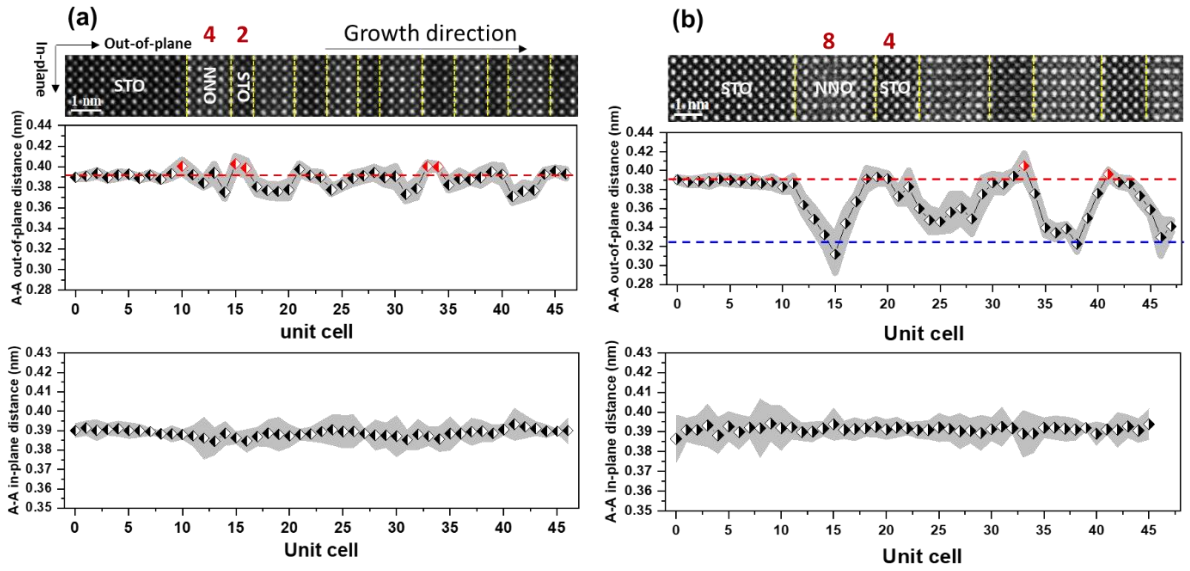

Figure 5.9 Variation of the Nd-Nd lattice spacing across the NNO2/STO interfaces. HAADF image of (a) $4NdNiO_2/2SrTiO_3$ and (b) $8NdNiO_2/4SrTiO_3$ superlattices aligned by a multi-frame method and corresponding variations of in-plane and out-of-plane Nd-Nd distances, respectively. The red and blue dashed lines indicate the references of the A-A out-of-plane distances from the $SrTiO_3$ substrate and bulk $NdNiO_2$, respectively. The red dots show larger A-A out-of-plane distances than the $SrTiO_3$ substrate.

Except for the difference in the variation of lattice spacing in SL_8_4 and SL_4_2, we quantify the Ni and Ti atom displacements across the STO/NNO2 interfaces as shown in Figure 5.10. Figure 5.10a presents an HAADF image and a corresponding atom displacement vector map for SL_4_2. The direction and length of the red arrows indicate the direction and distance of the atom displacements. A small displacement (below a mean value of 0.01 nm) of Ni atoms points to the NNO2 inner layer. In contrast, a larger Ni displacement occurs for SL_8_4 in Fig. 5.10b. The largest Ni displacement is ~0.05 nm and the average Ni displacement is about 0.025 nm. According to the reported DFT calculations[22], a Ni displacement of ~0.018 nm occurs at the $NiO_2/NdO/TiO_2$ interface due to the residual apical oxygen at the interfaces, without considering elemental intermixing. The value of the Ni displacement varies for different interface configurations[22]. The displacements of the Ni atoms imply a distortion of the Ni-O bonds at the interfaces[22], indicating a stronger distortion of the Ni-O bond at the interfaces in SL_8_4 than in SL_4_2. In addition, the atomic displacements could extend to several unit cells of the NNO2 inner layer in SL_8_4 due to a larger interface polarity, while it is not present in SL_4_2, which would be more pronounced in a NiO_2-terminated surface layer[14]. It should be noted that the displacements of Ni atoms at the interfaces in our samples are inhomogeneous, which is influenced by the inhomogeneous distribution of residual oxygen. There is evidence of an inhomogeneous distribution of local distortions of the oxygen sublattice at the interfaces, as shown in the enlarged iCoM images in Fig. 5.2. There is also a slight displacement of the interfacial Ti in both SL_8_4 and SL_4_2.

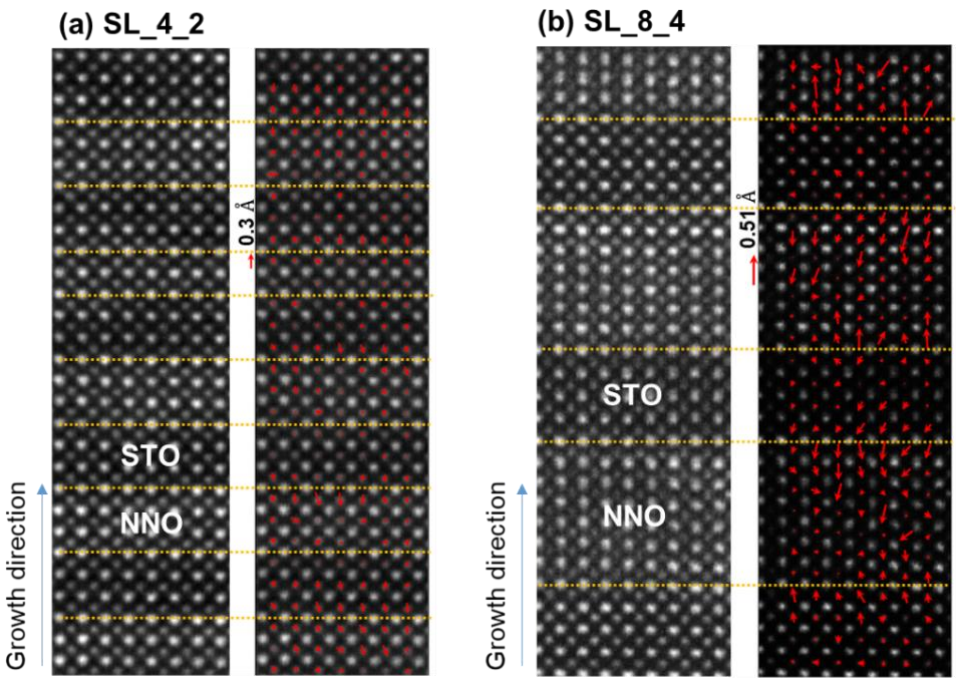

Figure 5.10 HAADF images and displacement vector maps of B atoms (B: Ni, and Ti) for (a) $4NdNiO_2/2SrTiO_3$ and (b) $8NdNiO_2/4SrTiO_3$ superlattices.

In addition, we calculated the Ni displacement map from the HAADF image in the $8NdNiO_3/4SrTiO_3$ superlattice as shown in Fig. 5.11, where the largest Ni shift is ~0.025 nm, which is half of that in the reduced sample. This indirectly indicates the interface reconstruction induced by the enhanced polar discontinuity during topotactic reduction.

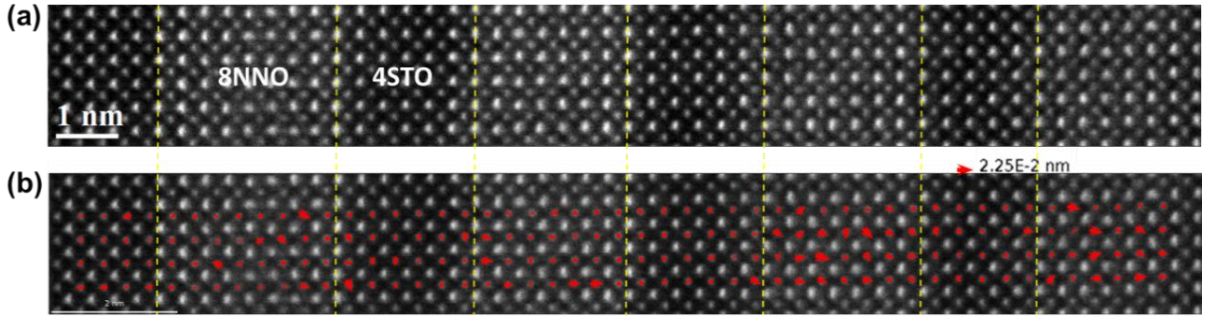

Figure 5.11 HAADF image (a) and displacement vector map (b) of B atoms (B: Ni, and Ti) for the $8NdNiO_3/4SrTiO_3$ superlattice.

5.3.4 Artifacts at the interface during the reconstruction of the electric field via 4D-STEM

Strong interface polarity drives the formation of a 2DEG by the occupation of the interfacial Ti 3*d* state in a $LaAlO_3/SrTiO_3$ (001) interface, accompanied by superconductivity.[21, 141] In the case of infinite layer nickelate films, the theoretical calculation showed that electronic reconstruction drives a 2DEG at the NNO2/STO interface. In our superlattice sample, we observed two types of interface configurations

that depend significantly on the Ti/Ni intermixing at the interface. Here, we used 4D-STEM to reconstruct the electrostatic field across the interfaces as shown in Fig. 5.12. The HAADF image of the 8NNO2/4STO superlattice shows the region where we performed the 4D-STEM measurements. There is no change in the *x*-direction electric field, E*x*, in Fig. 5.12b, while there is a clear difference in the *y*-direction electric field, E*y*, at the interfaces in Fig. 5.12c. Fig. 5.12d shows the line profile of E*y*, where we can see the negative and positive fields at the interfaces. However, there is an artifact in the reconstructed field, because the mean inner potential of STO and NNO2 is different. The mean inner potential is related to the composition of the material, which can be seen in the HAADF image. We have extracted the line profile of the HAADF image in Fig. 5.12e and calculated its gradient in Fig. 5.12f (Note: the calculation is physically meaningless), which shows a similar figure to the measured field in Fig. 5.12f. The small difference could be due to the electrostatic field.

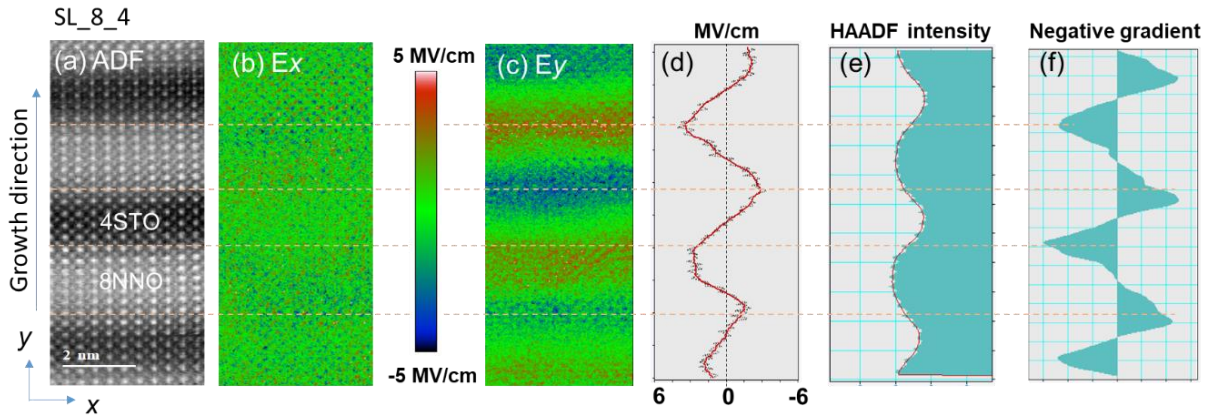

Figure 5.12 Electric field reconstruction at 8NNO2/4STO interfaces. (a) ADF image of the interface. (b) The reconstructed electric field maps in (b) *x*-direction and (c) *y*-direction. (d) The averaged line profile of Ey. (e) Line profile of HAADF intensity across the interface. (f) Negative gradient of the line profile of HAADF intensity in (e).

In order to identify artifacts from the difference of the mean inner potential, we performed a 4D-STEM simulation and reconstructed the field using the same method by quantifying the beam shift. Figure 5.13a shows the ADF image of the NNO2/STO interface and the corresponding E*x* and E*y* are shown in Figure 5.13b and c, respectively. We integrated the field at each atomic column, where the net field should be zero. As shown in Fig. 5.13d, the net field is zero in the NNO2 and STO bulk regions, while there is an obvious contrast at the interface. From the extracted line profile in Fig.13e, there is a field resulting from the difference in the mean inner potential of NNO2 and STO. The intensity and width of the artificial field peak are also affected by the beam broadening. In our sample, the interface is not as sharp as in the structural model for the simulation due to elemental intermixing, which leads to a wider field peak. The charge information may be obscured by this artifact.

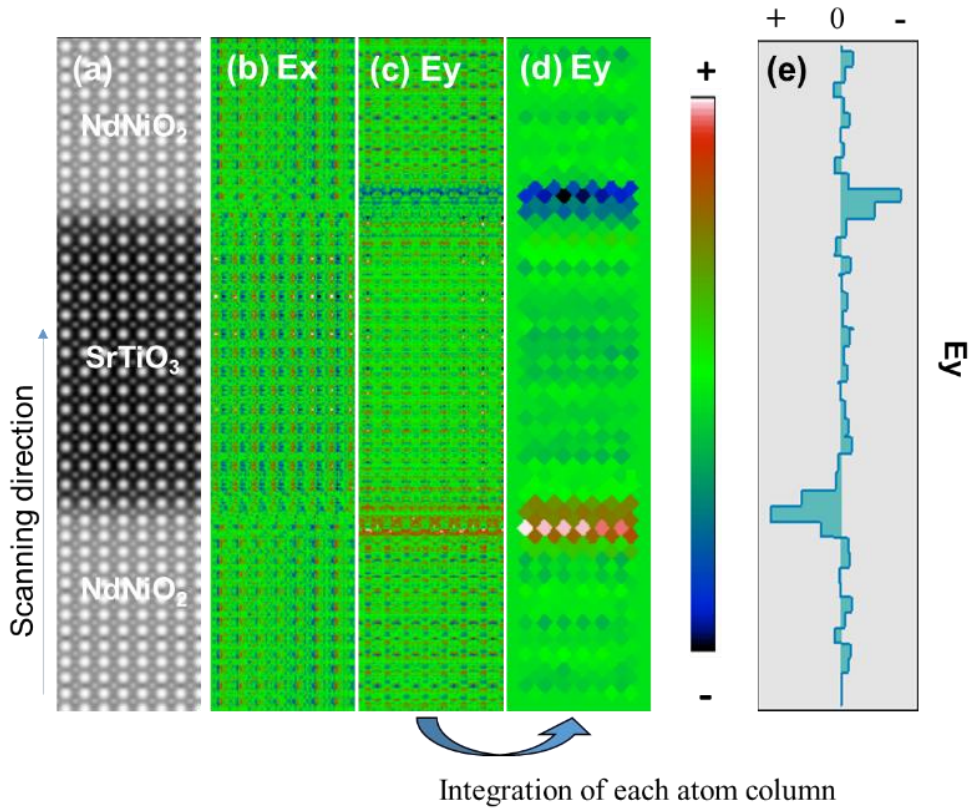

Figure 5.13 Simulated electric field at NNO2/STO interfaces. (a) ADF image of the interface. (b) The reconstructed electric field maps in (b) *x*-direction and (c) *y*-direction. (e) The averaged line profile of Ey.

5.3.5 Discussion

Atomic and electronic structures are closely related to the interface polarity, which plays a critical role in the interface properties. It can be easily influenced by elemental intermixing, oxygen sublattice occupancy, and transition metal valence variations. The interface configuration is dominated by a $NiO_2/NdO_x/TiO_2$ interface in both SL_4_2 and SL_8_4 samples, where *x* is affected by the proportion of Ti intermixed into Ni sites. The EELS maps show inhomogeneous Ni/Ti intermixing at STO/NNO2 interfaces. Ti intermixing in Ni sites suppresses the reduction of apical oxygen at interfaces. The iCoM images provide direct evidence of residual oxygen at interfaces. The residual oxygen can contribute additional electrons to decrease the interface polarity by hindering the formation of a strong built-in electric field. On the other hand, the presence of residual oxygen can cause a change in the atomic structure near the interfaces. From the quantification of cation displacements, a strong Ni displacement occurs in SL_8_4. In principle, the out-of-plane Nd-Nd distance is larger in a $NdNiO_3$ film than in a $NdNiO_2$ film. As the chemical composition varies from $\{NdNiO_2\}$ in the NNO2 inner layer towards $\{NdNiO_3\}$ near the interfaces, the out-of-plane Nd-Nd distance gradually increases accordingly. Meanwhile, the asymmetric distribution of the chemical composition at each unit cell leads to a Ni displacement towards the NNO2 inner layer, which is in agreement with a gradual decrease of the oxygen concentration from the interface to the NNO2 inner layer. In contrast, the concentration variation of the residual oxygen is within two unit cells and a relatively weaker asymmetric distribution

of the chemical composition in SL_4_2 leads to a smaller Ni displacement. Furthermore, the atomic displacements extend to several unit cells of the NNO2 inner layer in the SL_8_4 sample, while it is not visible in the SL_4_2 sample due to a smaller interface polarity and the lower number of NNO2 layers. These differences in the atomic reconstruction at the interfaces lead to a difference of the electronic structure at the interfaces. Specifically, the larger out-of-plane shift of Ni ions in the SL_8_4 sample indicates an increase in the distance between the apical oxygen and Ni, which increases the orbital polarization compared to that in SL_4_2. This might enhance the electronic transport of the SL_8_4 sample[150]. Moreover, the excess charges can be accommodated by Ni-3*d* orbital due to Jahn-Teller distortions at interfaces, which is a possible reason why the Ti valence tends to be 4+[144]. In addition, we find that atomic steps were formed at the interfaces in both SL_8_4 and SL_4_2 samples, as the areas marked with yellow arrows in Fig. 5.14, accompanied by a step distribution of apical oxygen at the interfaces, as displayed in Fig. 5.15. That leads to a local change of the chemical composition, inhibiting the formation of a strong built-in electric field across the interfaces to a certain extent. It is worth noting that the sharp decrease of the out-of-plane lattice spacing in 8_4 SL (Fig. 5.10) during the reduction process could lead to a lattice deformation more easily than in 4_2 SL, especially at the interfaces with steps. As shown in the overview HAADF images in Fig. 5.14, there is a decrease in the stability of the infinite-layer phase from 4_2 SL to 8_4 SL. In addition, the microstrain from the unit cell adjacent to the step-like interface causes local distortion of the NiO_5 pyramidal structure. Furthermore, the valence change of Ni is verified by calculating the Ni-$L_{2,3}$ white-line ratio, which is related to the electron occupancy in the Ni 3*d* orbital. The increase of the Ni valence at interfaces helps to screen the polar instability according to the charge transfer self-consistent model[22, 151]. The gradual variation of the valence change of Ni gradually reduces the built-in electric field between the adjacent two layers in the layer-by-layer structure. Moreover, the observed lattice expansion between the first NdO layer and the last TiO_2 layer allows to lower the electrostatic potential energy in a point-charge lattice model[22, 152]. Thus, we demonstrated the thickness-dependent interface polarity in NNO2/STO superlattices and systematically analyzed the effects of the reconstruction of the atomic and electronic structures on the interface polarity.

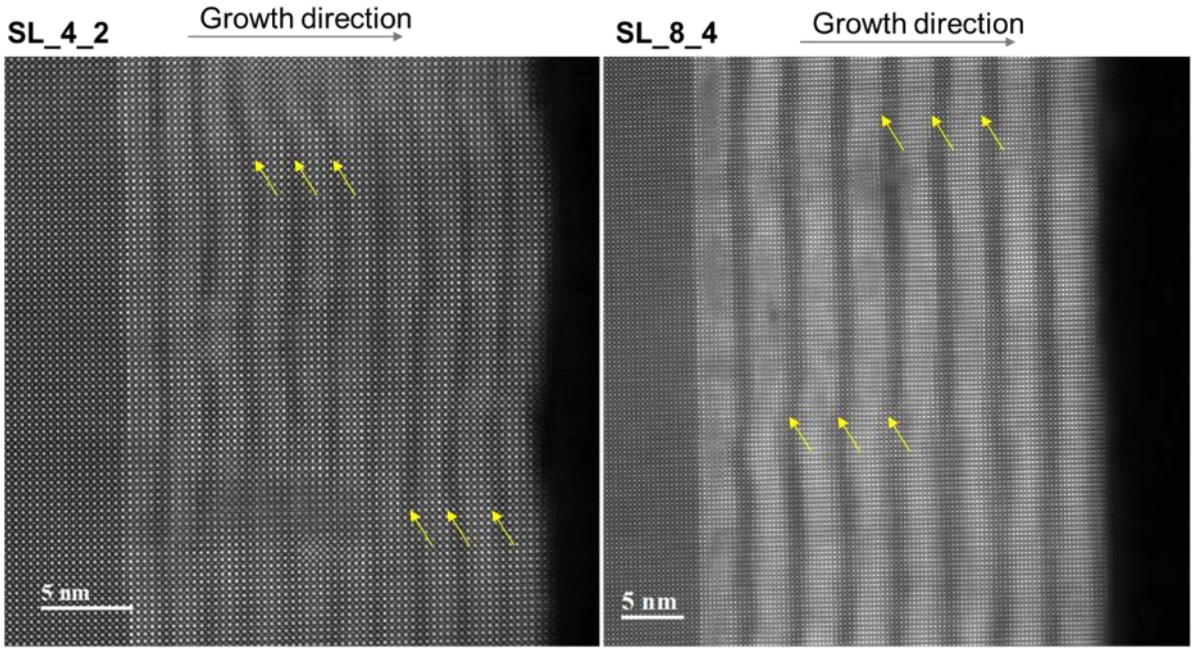

Figure 5.14 Overview HAADF images of $4NdNiO_2/2SrTiO_3$ and $8NdNiO_2/4SrTiO_3$ superlattices. Yellow arrows marked some steps at interfaces in both samples.

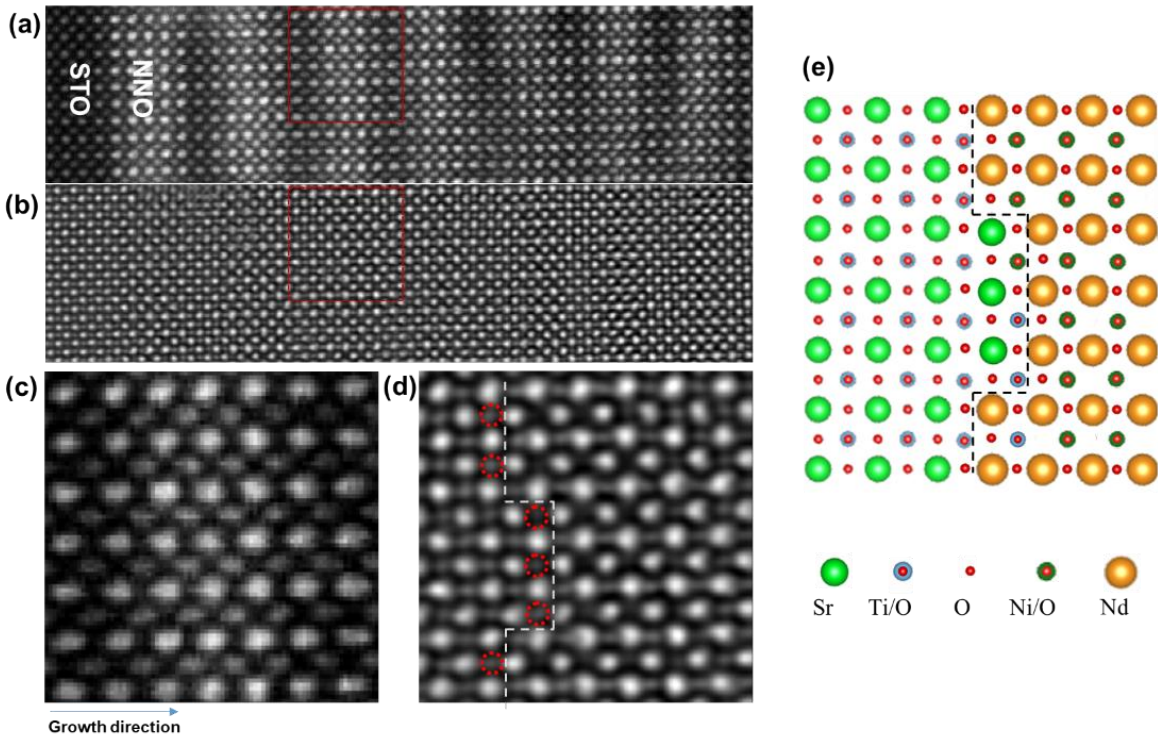

Figure 5.15 (a) ADF image and (b) iCoM image reconstructed from a 4D-STEM dataset of a $4NdNiO_2/2SrTiO_3$ superlattice. (c) The enlarged ADF image and (d) iCoM image are from the regions marked with red dashed boxes in (a) and (b), respectively. The red circles indicate the presence of apical oxygen atoms. (e) A schematic diagram of the interface structure with steps.

5.4 Summary

In combination with atomic-resolution STEM-EELS and 4D-STEM, we systematically investigated the effects of oxygen distribution and occupancy, elemental intermixing, cation distortion, and layer-stack thickness on the interface polarity in NNO2/STO superlattices. We directly imaged that the reduction process leads to different local oxygen ligand field variations and a gradual variation of oxygen content in the nickelate layers by 4D-STEM. The valence variation of Ni is closely related to the local concentration of residual oxygen. The residual oxygen, the valence change of Ni, the formation of atomic steps at the interfaces, and the lattice distortion contribute to the release of the polar instability at the STO/NNO2 interfaces. Additionally, we found a thickness-controlled interface structure and a corresponding tunable interface polarity. When reconstructing the electric field and charge density at the interfaces, artifacts due to the difference in the mean internal potential should be considered. The 4D-STEM simulation is necessary as a reference to properly interpret experimental observations.

Contributions to this chapter:

Part of this chapter has been published in Ref.[153-154] Chao Yang conceived and performed this work and wrote this chapter. Roberto A. Ortiz (MPI-FKF) grew the nickelate samples under the supervision of Bernhard Keimer (MPI-FKF) and Eva Benckiser (MPI-FKF). Yi Wang (MPI-FKF), Wilfried Sigle (MPI-FKF) and Hongguang Wang (MPI-FKF) contributed to the discussions on the EELS measurements and data analysis. Yi Wang (MPI-FKF) helped with data processing. Peter A. van Aken (MPI-FKF) and Wilfried Sigle (MPI-FKF) supervised this work. The work in this chapter was supported in sample preparation by Ute Salzberger (MPI-FKF) and Julia Deuschle (MPI-FKF) and in TEM by Kersten Hahn (MPI-FKF) and Peter Kopold (MPI-FKF).

Chapter 6 Atomic insights of the surface reconstruction and structural ordering in partially reduced nickelate films

6.1 Introduction

Polarity at interfaces and surfaces in complex oxide thin films plays a critical role in their physical and chemical properties such as ferroelectricity[155-161], superconductivity[140], magnetism[162], and catalysis[163]. By controlling the orientation and termination of the crystal plane during film growth, polar surfaces and interfaces can be obtained, where structural distortions form due to the interaction of short-range covalency and long-range electrostatic effects[154, 164-166]. At surfaces, the abruptly reduced coordination significantly alters the lattice and electronic structures, potentially affecting the overall physical and chemical properties of the thin oxide material. For example, polar distortions and octahedral rotations at the polar surface of a $LaNiO_3$ single-crystal film weaken the hybridization of Ni 3*d* and O 2*p* orbitals[166], resulting in reduced metallicity and thickness-dependent transport behavior[167-169]. Capping with an insulating $LaAlO_3$ layer[169] or changing the surface termination[166] can reduce or eliminate the polar distortion, and thus recover the metallic conductivity of the $LaNiO_3$ film again. Furthermore, the excess charges on the polar surfaces lead to the emergence of different electronic states such as charge density waves and localized electron polarons[2]. Recently, a charge density wave state has been observed in the infinite layer (R, Sr)NiO_2 (R = La, Nd)[170] where the presence of a $SrTiO_3$ top layer can lead to controversial results[171-172], possibly indicating the potentially critical influence of polarity on the surface or interface electronic state. Additionally, surface polarization can effectively boost electro- and photocatalytic performance by tuning adsorption intensity and charge separation at catalyst surfaces[163]. Therefore, exploration and control of surface polarity is essential for engineering functionalities of electronic devices and surface catalysts.

Exploiting and controlling surface polarity in complex oxide thin films is a challenging task due to the difficulty of growing precisely controlled single atomic layer terminated crystal film surfaces and probing their local atomic and electronic structures[159]. However, theoretical studies have demonstrated that electronic orbitals can be modified by polar surface distortions. For example, the NiO_2-terminated negatively charged surface in $LaNiO_3$ thin films has been found to have a large orbital polarization, which is a promising approach to mimic the electronic configuration of high-temperature cuprate superconductors[173-174]. Additionally, the surface termination can also influence the polar distortions in $LaNiO_3$ thin films, as determined from the analysis of crystal truncation rods (CTR) measured by synchrotron X-ray diffraction, thereby altering the electronic conduction[166]. Other experimental observations have revealed different phases at polar surfaces, such as polarization-controlled surface reconstruction in a $Pb(Zr_{0.2}Ti_{0.8})O_3$ film[164] and competing electronic states, e.g. charge-density waves and localized electron polarons, at a TaO_2-terminated polar surface in a $KTaO_3$ film[2].

The infinite-layer structure of nickelates, which becomes superconducting upon appropriate cation doping[16-17, 26, 137-138], can only be synthesized by oxygen deintercalation via topochemical reduction. In the latter process, the compositional and structural changes can lead to modifications in polarity at interfaces or surfaces due to the removal of the apical oxygen ions[21-22, 175]. In this study, we aimed to control the extent of oxygen deintercalation to modify the surface polarity in a $Pr_{0.8}Sr_{0.2}NiO_{2+x}$ film and used a combination of atomic resolution electrostatic field imaging via a combination of 4D-STEM and

STEM-EELS to directly image the variation of atomic and electronic structures at the surface layer. Our results provide direct evidence for the homogeneous Sr doping in the $Pr_{0.8}Sr_{0.2}NiO_3$ film and how the polar distortion and oxygen octahedra rotation in the surface layer are connected. A distinct and even stronger surface reconstruction is found in a $Pr_{0.8}Sr_{0.2}NiO_{2+x}$ film, synthesized by topochemical reduction from the same piece of a $Pr_{0.8}Sr_{0.2}NiO_3$ sample, which is associated with thickness-dependent oxygen deintercalation.

6.2 Specimen preparation

The pristine $Pr_{0.8}Sr_{0.2}NiO_3$ film was grown on a $NdGaO_3$ (110) single crystal of size 1×1 cm^2 using ozone-assisted layer-by-layer MBE with a substrate temperature of ~600°C and a pressure of 2.4×10^{-7} bar under ozone flow. The samples were cut into four pieces of size 5×5 mm^2 and then two of them were reduced by a topochemical reduction process involving heating the samples at 230°C for 6 and 18 hours with 0.1 g of CaH_2 powder. The sample and powder were separated by aluminum foil in a vacuum-sealed glass tube.

The TEM samples were prepared using a focused ion beam in a high vacuum and further cleaned using a Fischione NanoMill system. STEM imaging and EELS spectral imaging were performed with a probe-corrected electron microscope (JEOL ARM200F, JEOL Co. Ltd.) at 200 kV. The STEM-ABF and HAADF images were acquired with collection semi-angles in the range of 10-20 mrad and 70-300 mrad, respectively. A Gatan K2 camera provides an energy resolution of ~1 eV with a dispersion of 0.5 eV per channel. The collection semi-angle for EELS was 85 mrad. A PCA method[80] was used to denoise the spectral images. 4D-STEM experiments were performed in 1-bit mode with continuous reading and writing at a frame time of 4.8×10^{-5} s using a Merlin direct electron detector (256 × 256 pixels, Quantum Detectors). The 4D-STEM results were optimized by multi-frame acquisition. The electrostatic field maps were calculated using a simplified quantum mechanical model of the formula 2.20.[44, 66, 97]

6.3 Results and Discussions

6.3.1 Polarity-induced surface reconstruction in nickelates films

Fig. 6.1 illustrates the use of STEM imaging to study polar surfaces of $Pr_{0.8}Sr_{0.2}NiO_3$ and $Pr_{0.8}Sr_{0.2}NiO_{2+x}$ films. The cations in these films (Pr, Nd, Ga, and Ni) can be easily distinguished in the HAADF images due to their different atomic numbers. In Fig. 6.1a, the displacement map of the B atoms (B: Ni and Ga) shows a Ni displacement of ~0.27 Å at the surface layer, which gradually decreases to zero within ~3 unit cells below the surface. This displacement is consistent with previous studies on $LaNiO_3$ films using CTR[166, 176]. In topotactically reduced $Pr_{0.8}Sr_{0.2}NiO_{2+x}$ films, we observe an increase in the magnitude of the Ni displacement to ~0.37 Å for a reduction time of 6 h (see Fig. 6.1c) and to ~0.45 Å for a reduction time of 18 h (see Fig. 6.2). Fig. 6.3 shows the overview HAADF images of the pristine and reduced samples, where there are no obvious defects in the inner layer of these films. To quantify these structural changes, we use Gaussian fitting and center-of-mass refinement techniques based on the Atomap python package[55]. We define the atomic positions from the HAADF images and quantify the structural parameters, including in-plane and out-of-plane lattice spacings, and the A–A–A (A: Pr and Nd) zigzag angle, as shown in Fig. 6.1b and d. The difference between the A–A and B–B out-of-plane lattice spacings shows the Ni displacement. There is no visible change in the B–B in-plane lattice

spacing, suggesting tensile strain in the $Pr_{0.8}Sr_{0.2}NiO_3$ film. The A–A in-plane lattice spacing decreases slightly from the substrate to the film due to the larger zigzag angle of Nd–Nd in bulk $NdGaO_3$ compared to that of Pr–Pr in bulk $PrNiO_3$. Another possible reason is that adjusting the zigzag angle can relieve the tensile strain to some extent, where the decrease in zigzag angle is shown in Fig. 6.1b and d. Enlarged HAADF images and corresponding schematic structure models in Fig. 6.1e clearly show the evolution of the atomic structures from a zigzag structure at the substrate interface to a polar distortion at the film surface.

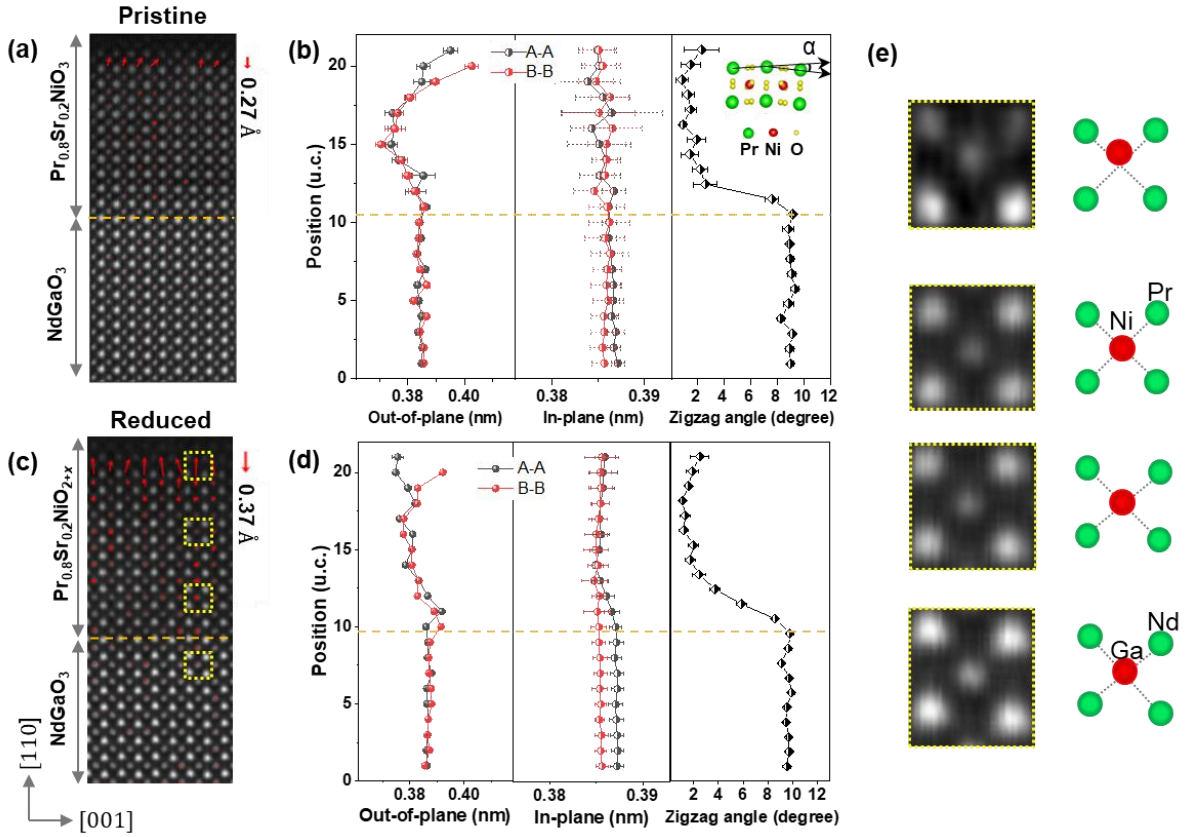

Figure 6.1 Atomic structures in pristine $Pr_{0.8}Sr_{0.2}NiO_3$ and topochemically reduced $Pr_{0.8}Sr_{0.2}NiO_{2+x}$ films. HAADF images and corresponding Ni displacement maps at the surfaces of (a) $Pr_{0.8}Sr_{0.2}NiO_3$ and (c) $Pr_{0.8}Sr_{0.2}NiO_{2+x}$ films. Variations of lattice distances (in out-of-plane and in-plane lattice directions) and A–A–A (A: Nd, and Pr) zigzag angle in (b) $Pr_{0.8}Sr_{0.2}NiO_3$ and (d) $Pr_{0.8}Sr_{0.2}NiO_{2+x}$ films. The yellow dashed lines indicate the film/substrate interfaces. α indicates the zigzag angle. (e) Enlarged HAADF images from the yellow dashed boxes in (c) and corresponding schematic structures for the atomic structure evolution from the $NdGaO_3$ substrate to the film surface. Red spots represent atom columns of Ni or Ga, and green spots are Nd or Pr atom columns.

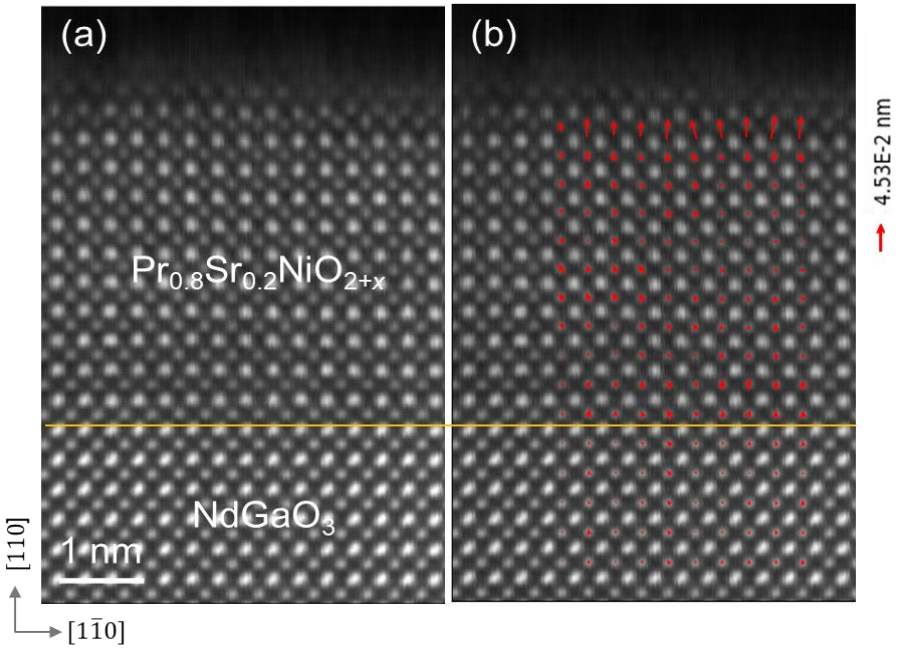

Figure 6.2 (a) HAADF image and (b) corresponding Ni displacement vector map of a $Pr_{0.8}Sr_{0.2}NiO_{2+x}$ sample with a topochemical reduction time of 18 h. The red arrows indicate the direction and magnitude of B (B: Ni, and Ga) displacements. The largest displacement of Ni is 0.453 Å.

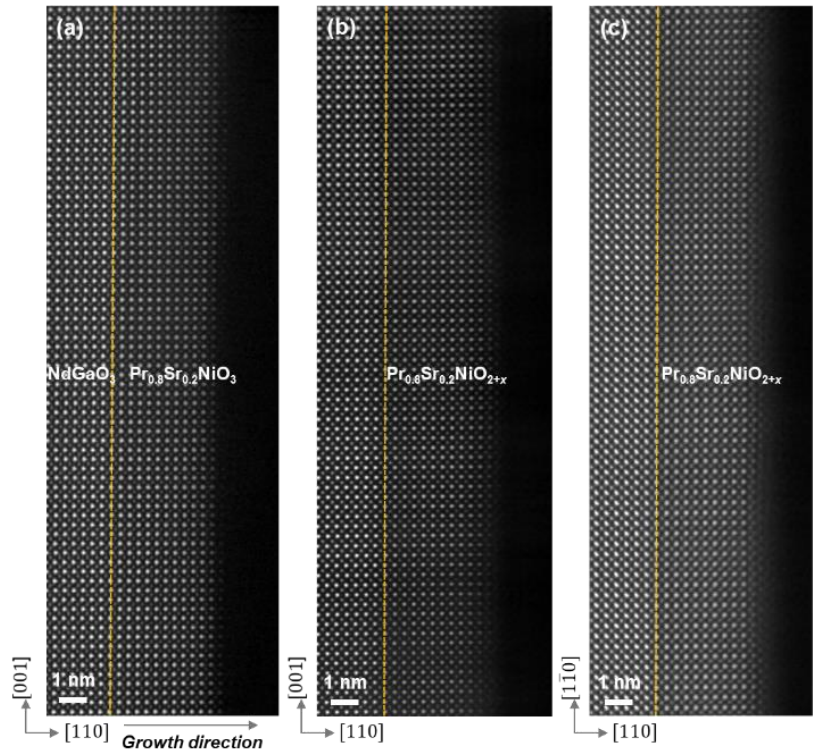

Figure 6.3 HAADF images of (a) a fully oxide $Pr_{0.8}Sr_{0.2}NiO_3$ film, $Pr_{0.8}Sr_{0.2}NiO_{2+x}$ films reduced for (b) 6 h and (c) 18 h.

To determine the polar structure at the surface layer, we identified oxygen atomic columns and quantified the relative displacement of oxygen and B cations at the BO_2 plane. Figures 6.4a and 6.4c show the experimental high-resolution ABF images at surface regions in $Pr_{0.8}Sr_{0.2}NiO_3$ and $Pr_{0.8}Sr_{0.2}NiO_{2+x}$ films, respectively. The figures reveal the coexistence of oxygen octahedra rotation and polar distortion at the subsurface of the pristine sample, consistent with that in the $LaNiO_3$ film measured by synchrotron X-ray surface diffraction[176]. The polar distortion dominates the structural changes in the surface region. Notably, a stronger polar distortion occurs at the subsurface of the reduced $Pr_{0.8}Sr_{0.2}NiO_{2+x}$ film, and a nonpolar rotation is not detected, as shown in Figure 6.4c. The enlarged ABF images and corresponding schematic structures in Figure 6.4d highlight the variations of the oxygen octahedra. The terminating NiO_2 layer shows obvious Ni–O–Ni buckling and there is strong polarization in the adjacent unit cell. Figure 6.4e quantitatively compares the relative displacements of the Ni and O columns at the NiO_2 plane in the out-of-plane direction between the pristine and reduced samples. The largest polar displacement is ~0.32 Å in the pristine sample and ~0.56 Å in the reduced one, indicating a significantly enhanced polar state at the surface region of the $Pr_{0.8}Sr_{0.2}NiO_{2+x}$ film. Such a large polar distortion strongly affects the electronic transport by modifying the orbital overlap between Ni 3*d* and O 2*p*, possibly inducing competition between local structures at the surface, interior and interface, and modifying the conductivity of the entire film[176]. The polarization decays within ~3 unit cells in both pristine and reduced samples, in agreement with the observed decay of polarization in a $LaNiO_3$ film[176].

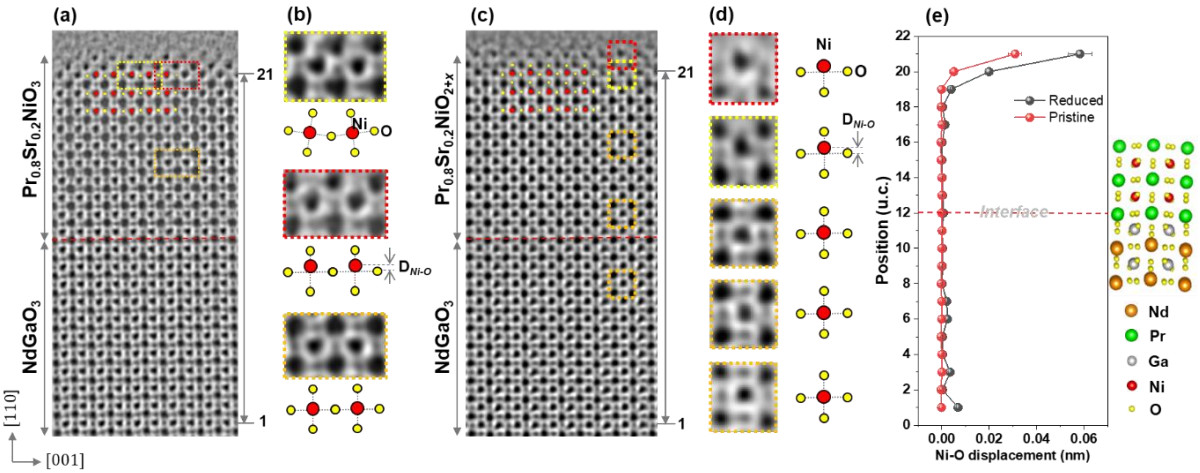

Figure 6.4 Oxygen sublattices in $Pr_{0.8}Sr_{0.2}NiO_3$ and $Pr_{0.8}Sr_{0.2}NiO_{2+x}$ films. HAADF images and corresponding Ni displacement vectors at surfaces of (a) $Pr_{0.8}Sr_{0.2}NiO_3$ and (c) $Pr_{0.8}Sr_{0.2}NiO_{2+x}$ films. (b) Enlarged ABF images and the corresponding schematic structural models (below) show the variation of oxygen octahedra in the pristine sample. (d) Enlarged ABF images and the corresponding schematic structural models (right) show the variation of oxygen octahedra in the reduced sample. (e) The relative displacement of Ni and O at the NiO_2 plane in the out-of-plane direction. The schematic atomic structure at the $PrNiO_3/NdGaO_3$ interface.

6.3.2 Thickness-dependent oxygen distribution in partially reduced nickelate films

Next, we investigate the electronic structure of the reduced $Pr_{0.8}Sr_{0.2}NiO_{2+x}$ film using EELS fine-structure analysis of the Ni-$L_{2,3}$ and O-K edges near the surface. Figure 6.5a shows the ADF image for

the EELS data analysis, with spectra extracted layer by layer from the regions marked with red dashed boxes. Layers 1-12 belong to the film. The extracted O-*K* edge spectra in Figure 6.5b identify the film, with a pronounced pre-peak indicating hybridization of O-2*p* and Ni-3*d* orbitals in the NiO_6 octahedra, which is sensitive to changes in Ni valence and Ni-O bond length. Figure 6.5c shows a gradual decrease in the maximum intensity ratio of peaks A and B of the O-*K* edge, indicating a decrease in the hybridization of Ni 3*d* and O 2*p*. This can decrease the metallicity[166-167]. Figure 6.5d shows a shift of the Ni-L_3 edge to lower energies, suggesting a change in Ni valence. Analysis of the white-line ratio of the Ni-$L_{2,3}$ edges in Figure 6.5e reveals that the Ni valence decreases from the inner layer to the surface of the film, where the references of Ni^{3+} and Ni^{2+} are taken from $NdNiO_3$[129] and NiO films[126] respectively. This is consistent with changes in the atomic electric fields surrounding Ni atomic columns measured by 4D-STEM. In contrast, the Ni valence remains almost constant around Ni^{3+}, except for a small decrease in the last unit cell in the pristine sample (see Figure 6.6), due to possible oxygen vacancies at the surface to compensate for a surface charge. However, it is worth noting that besides the electronic structure reconstruction induced by the polar distortion, oxygen vacancies are further important factors influencing both the Ni valences and the polar state.

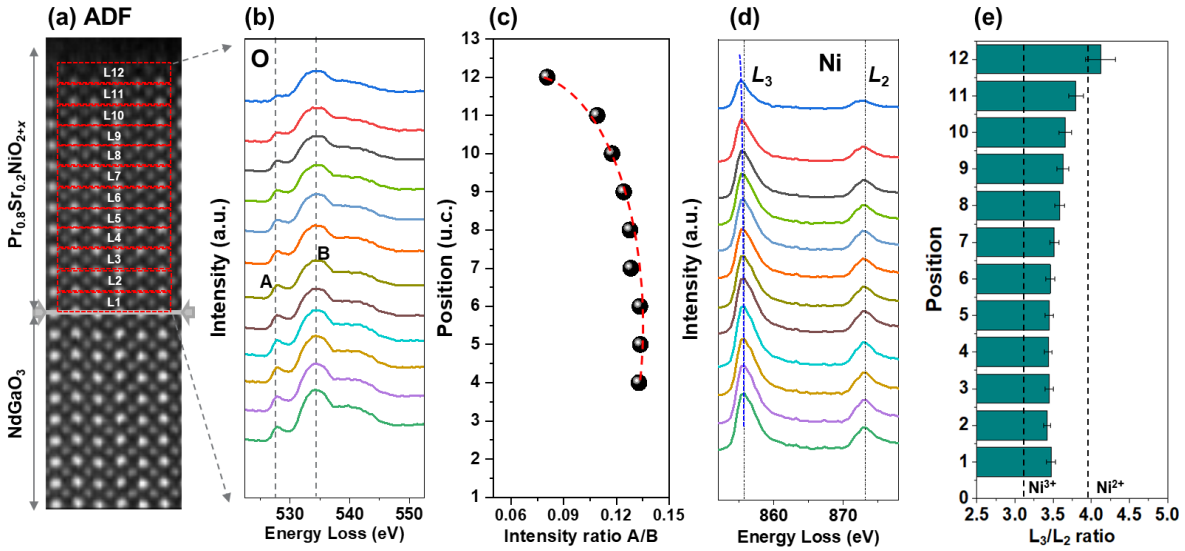

Figure 6.5 EELS measurements of the Ni-$L_{2,3}$ and O-*K* edges in the reduced $Pr_{0.8}Sr_{0.2}NiO_{2+x}$ film. (a) ADF image for EELS data analysis. (b) O-K edges and (d) Ni-$L_{2,3}$ edges extracted from the regions marked in (a). (c) Calculated intensity ratios of peaks A and B from O-*K* edges. (e) Ni-$L_{2,3}$ white-line ratios extracted from the regions marked in (a).

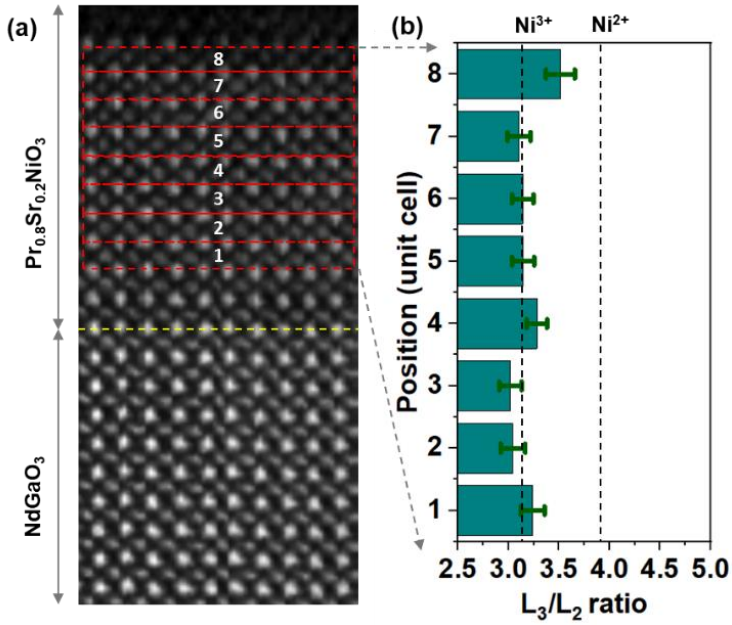

Figure 6.6 EELS measurement of the Ni-$L_{2,3}$ edges in the pristine $Pr_{0.8}Sr_{0.2}NiO_3$ film. (a) ADF image for EELS data analysis. (b) Ni-$L_{2,3}$ white-line ratios extracted from the regions marked in (a).

To gain insight into the distribution of oxygen, we analyzed the elemental distribution from O-*K* EELS maps resolved layer-by-layer (see Figure. 6.7). We identified the cation atom columns in both pristine and reduced samples using the Ga-$L_{2,3}$, Nd-$M_{4,5}$, Pr-$M_{4,5}$, and Ni-$L_{2,3}$ edges. The composite map in Figure 6.7b and e shows the elemental distribution from the substrate to the film surface. Due to the high energy loss of the Sr-$L_{2,3}$ edge and the low Sr doping concentration, the Sr signal was hardly measurable by STEM-EELS. Therefore, we employed atomic resolution STEM-EDX, which showed that the Sr signal was homogenous throughout the film (Figure 6.8). We determined the oxygen content by integrating the O *K* edges and normalizing them to the Ni-$L_{2,3}$ edges in Figures 6.7c and f. In the pristine sample (Figure 6.7c), we observed a decrease in both Ni and O content within a unit cell at the surface. Since the stoichiometry was still maintained, this was likely a result of the sample thickness. In contrast, the reduced sample had a significant decrease in O signal intensity, with an estimated O/Ni ratio of ~2.5 at the surface. The Ni signal remained approximately the same throughout the area, consistent with the change in Ni valence mentioned above. In addition, the gradual decrease in oxygen concentration suggests a thickness-dependent deintercalation of oxygen.

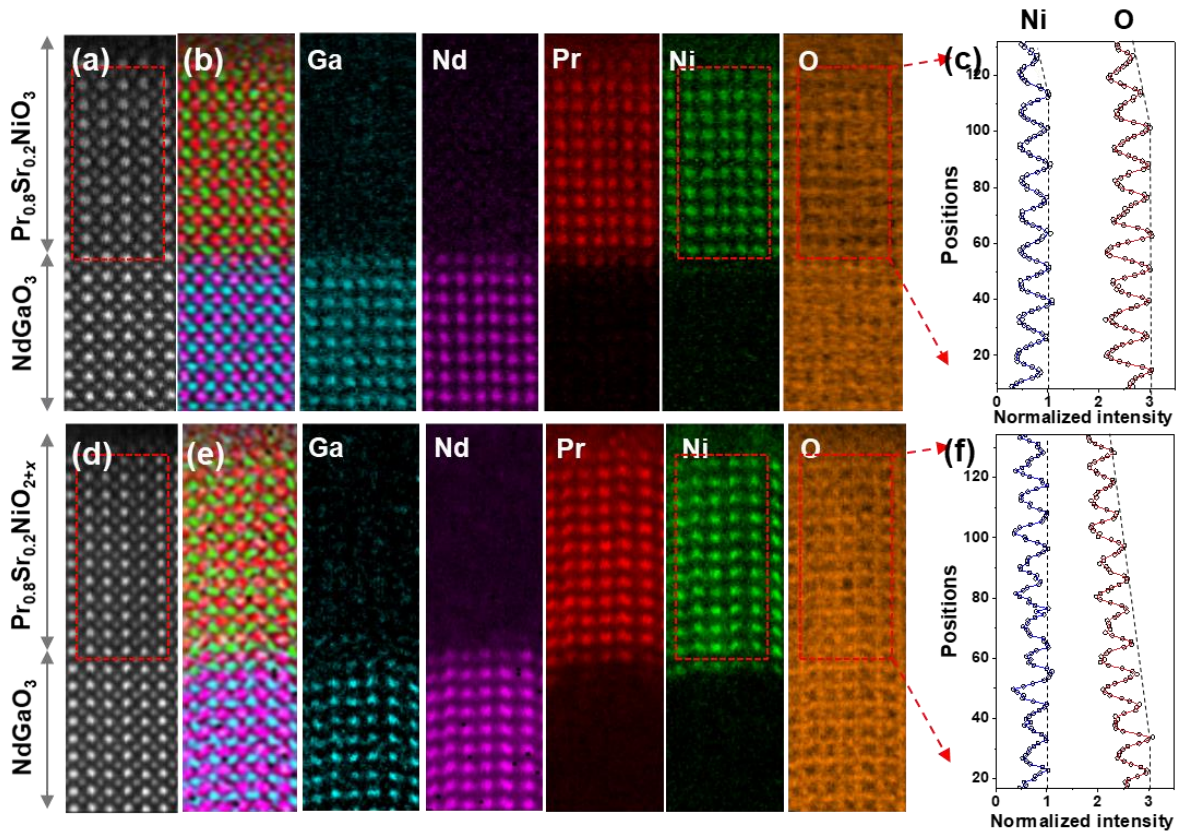

Figure 6.7 Elemental distribution and variation of oxygen concentration in $Pr_{0.8}Sr_{0.2}NiO_3$ and $Pr_{0.8}Sr_{0.2}NiO_{2+x}$ films. HAADF images of (a) $Pr_{0.8}Sr_{0.2}NiO_3$ and (d) $Pr_{0.8}Sr_{0.2}NiO_{2+x}$ films for EELS analysis. EELS maps of Ga, Nd, Pr, Ni, and O. (b, e) Color-coded mapping of Ga (blue), Nd (purple), Pr (red), Ni(green), and O (yellow). The normalized signal intensity of Ni and O in (c) $Pr_{0.8}Sr_{0.2}NiO_3$ and (f) $Pr_{0.8}Sr_{0.2}NiO_{2+x}$ films.

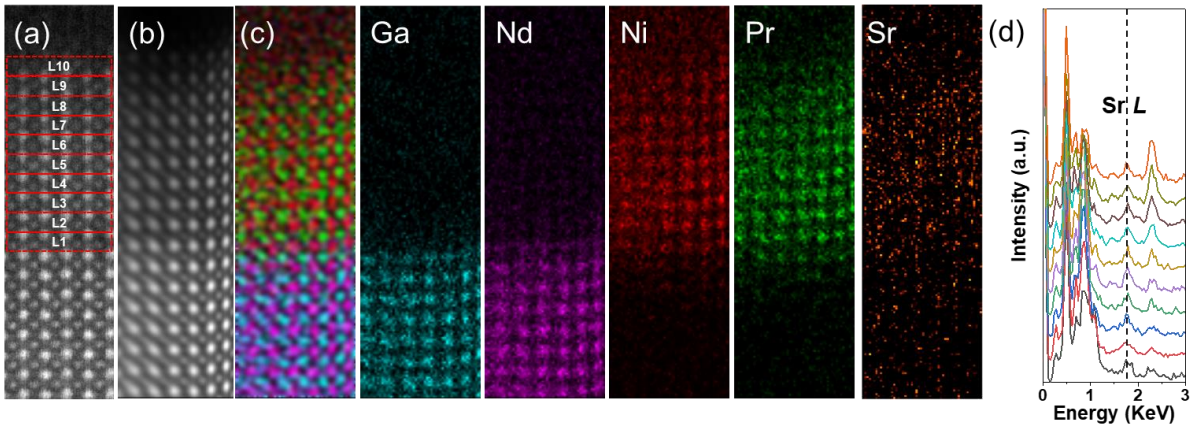

Figure 6.8 Elemental distribution measured by STEM-EDX. (a, b) HAADF images for the STEM-EDX measurements. (c) Color-coded mapping of Ga (blue), Nd (purple), Ni (red), Pr (green), and Sr (orange). (d) Extracted layer-by-layer STEM-EDX spectra in the $Pr_{0.8}Sr_{0.2}NiO_3$ film, showing a constant Sr L signal for all layers.

6.3.3 Atomic electric field mapping in partially reduced nickelate films

In order to understand the mechanism of electrostatic screening of the charged surface, we performed 4D-STEM experiments to measure the atomic-scale electrostatic fields and charge distribution at the surface of a reduced sample with a strong polar state. To minimize the scanning distortion and improve the signal-to-noise ratio, we optimized the reconstructed images in Figure 6.9 by aligning and summing four consecutive frames. We carefully prepared and measured the sample, which has a thickness of around 5.2 nm, as determined from position-averaged convergent beam electron diffraction (PACBED) patterns (see Figure 6.10b-e), to ensure a quantitative understanding of the atomic electric field[44, 66]. We also identified no tilt of the sample, as confirmed by the PACBED patterns and the oxygen octahedral structure from the ABF image in Figure 6.4. Figure 6.9b shows the modulus of the atomic electric field map. The electric fields surrounding Pr and Nd atoms are stronger than those around the Ni and Ga atoms due to their larger atomic numbers, and exhibit an approximately rotationally symmetric distribution. In particular, the magnitude and symmetry of the fields surrounding Ni atomic columns show a pronounced change near the surface, as shown in Figure 6.9d. We have extracted the line profile of the field strength surrounding the B (Ni and Ga) atomic columns marked with a black dashed line in Figure 6.9c, which shows that the magnitude increases in several unit cells near the surface. What is the relationship between polar distortions and electric field variations near the surface? To clarify this, we performed electric field simulations with different sample thicknesses, as shown in Figure 6.9e–g and Figure 6.10f–k. We created a supercell for 4D-STEM simulations without considering the Sr doping, as shown in Figure 6.9e, but including polar distortions in the surface region corresponding to the atomic structure in the ABF image of the reduced sample. Figure 6.9f shows the simulated electric field map for a sample thickness of 5.2 nm. According to the line profile in Figure 6.9g, there is no clear difference in the strength of the atomic electric field surrounding the Ni atoms. This suggests that the field variations in our experimental results are mainly due to valence change or charge redistribution rather than diffraction contrast induced by structural changes. The strong polar state in the reduced sample could induce electronic and atomic reconstructions, and oxygen vacancies can modify the surface polarization and Ni valence. Therefore, the observed stronger electric field surrounding Ni atoms at the surface region may mainly result from the valence change of Ni atoms. Additionally, we compared the simulated electric field maps for different sample thicknesses in Figure 6.10h–k. In samples with thicknesses of 8.3 nm and 9.9 nm, the reconstruction of the electric field from momentum transfer is no longer reliable due to the artifacts of the diffraction contrast caused by multiple scattering. The rotationally symmetric distribution of the atomic electric field around the atoms is broken. It is worth noting that the field strength of Ni atoms decreases from ~0.7 V/pm to 0.23 V/pm as the sample thickness increases from 5.2 nm to 9.9 nm. This magnitude of the atomic electric field surrounding Ni atoms from the simulation is consistent with the value (~0.7 V/pm, see Figure 6.9c) of the experimental result at the region far from the surface, further supporting the estimated sample thickness of around 5 nm measured by the PACBED patterns.

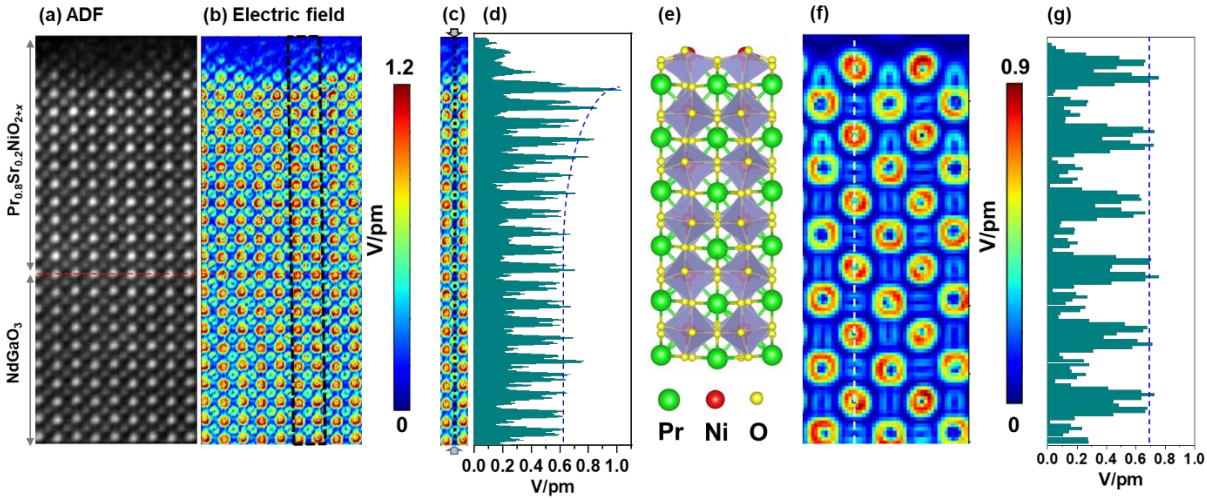

Figure 6.9 Extracted information from a 4D-data set of the reduced $Pr_{0.8}Sr_{0.2}NiO_{2+x}$ film. Reconstructed atomic-column-resolved (a) ADF, and (b) electric field images. (c) The electric-field map extracted from the region marked with a black dashed box in (b). (d) The line profile extracted from the region marked with a black dashed line in (c) indicates the changes in the magnitude of the electric field around B (B: Ni, and Ga) atoms. (e) A $PrNiO_3$ supercell created from the ABF image of a reduced sample with polar distortions at the upper surface. (f) Simulated electric field map. (g) The corresponding line profile of the electric field map marked with a white dashed line in (f).

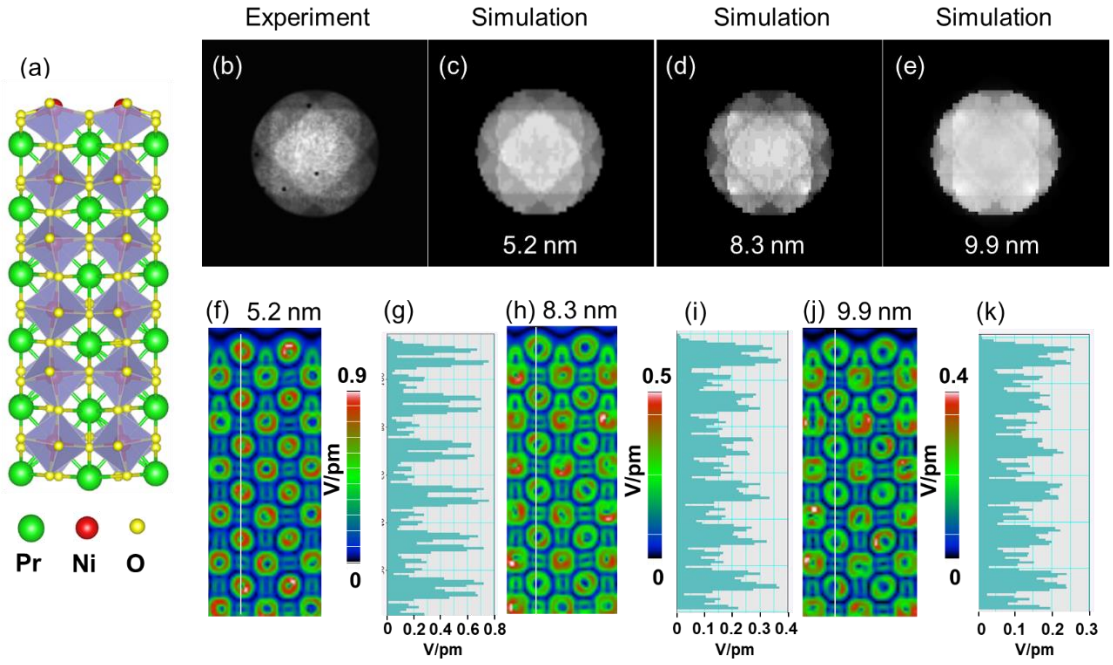

Figure 6.10 PACBED patterns and electric field maps with different sample thicknesses extracted from the simulated 4D-STEM. (a) A $PrNiO_3$ supercell created from the ABF image of a reduced sample with polar distortions at the upper surface. (b) The PACBED pattern extracted from the experimental 4D-STEM. Simulated PACBED patterns for sample thicknesses of (c) 5.2 nm, (d) 8.3 nm, and (e) 9.9 nm. Simulated electric field maps for sample thicknesses of (f) 5.2 nm, (h) 8.3 nm, and (j) 9.9 nm, and their corresponding line profiles of the electric field maps marked with white lines are in (g), (i), and (k), respectively.

6.3.4 Discussion

The presence of surface polarity can cause structural distortion, electronic reconstruction, and charge redistribution to screen the bound charges at the surface[164]. In the pristine sample, we observed cooperative coupling of polar distortion and octahedral rotation underneath the negatively charged NiO_2 surface, which is consistent with similar systems such as the NiO_2-terminated surface in a $LaNiO_3$ film[176] and a $PbTiO_3$ ferroelectric film[177]. The decay of polarization occurred within around three unit cells and there was no apparent oxygen deficiency to screen the surface field. Notably, in the reduced sample, a stronger polar distortion is formed at the surface due to oxygen deintercalation. Similarly, the polarization decayed within around three unit cells. Interestingly, the thickness-dependent oxygen deintercalation resulted in a gradually decreasing oxygen concentration from the substrate/film interface to the surface.

The removal of apical oxygen from NiO_6 octahedra is easier than that of basal oxygen[144], leading to an asymmetric distribution of the missing oxygen in the PrO layers in the out-of-plane direction, which strengthens the electrostatic field from a layer-by-layer structural perspective. This effect is particularly pronounced in the unit cells near the surface, where the polarity is significantly enhanced. The oxygen vacancies in the reduced sample also alter the valence of Ni, as evidenced by atomic electric field mapping and white-line-ratio calculations of Ni-$L_{2,3}$ edges. These maps reveal an enhanced field strength surrounding Ni atomic columns near the surface compared to the inner layer of the film and the substrate. This enhancement is primarily due to the increased valence charge of the Ni as determined by EELS. Electric field simulations of the stoichiometric phase $PrNiO_3$ also show comparable field magnitudes to the experimental values for the inner layer of the film. Thus, real-space imaging of atomic electric fields provides direct and reliable information for measuring valence variations. The lower formation energy of oxygen vacancies at the surface of the perovskite oxide[164] also allows the formation of oxygen vacancies at the NiO_2 surface layer, which can compensate for the surface electrostatic field due to its asymmetric bonding. Other factors such as absorption of atoms and faceting at the surface may also contribute to depolarization. However, obvious surface reconstructions are observed to screen the polar field and have been systematically analyzed at the atomic scale. In this system, a secondary phase can form under stronger surface polarity. This could be a reason for the instability of the infinite layer phase, which cannot be directly synthesized.

6.3.5 Observation of oxygen vacancy ordering in the reduced nickelates

In addition to the structural reconstruction at surfaces or interfaces mentioned above, the geometry effect plays an essential role in the inner region, which is the main component of the film. As shown in Figure 6.11, we observed a Pr distortion resulting from the formation of oxygen vacancy ordering. The direction of the formed oxygen vacancy ordering exhibited a 45 degree angle with respect to the substrate, which corresponds to a brownmillerite phase of nickelate. Figures 6.11f and h present structural models illustrating the two types of oxygen vacancy ordering observed. The presence of oxygen vacancies induced rotation of adjacent NiO_5 pyramids and Pr displacements. A similar structural ordering was previously observed in a $LaCoO_{2.5}$ film subjected to compressive strain. The case of the $PrNiO_3$ film, which is characterized by a pseudocubic lattice with a lattice constant of 3.83 Å, was deposited on a $NdGaO_3$ substrate with a pseudocubic lattice constant of 3.85 Å, resulting in tensile strain. In Figure 6.11b and 6.11d, we observed oxygen vacancies located at the basal sites near the

interface. This observation suggests that the ordering of oxygen vacancies is primarily influenced by the stoichiometry following the oxygen deintercalation process.

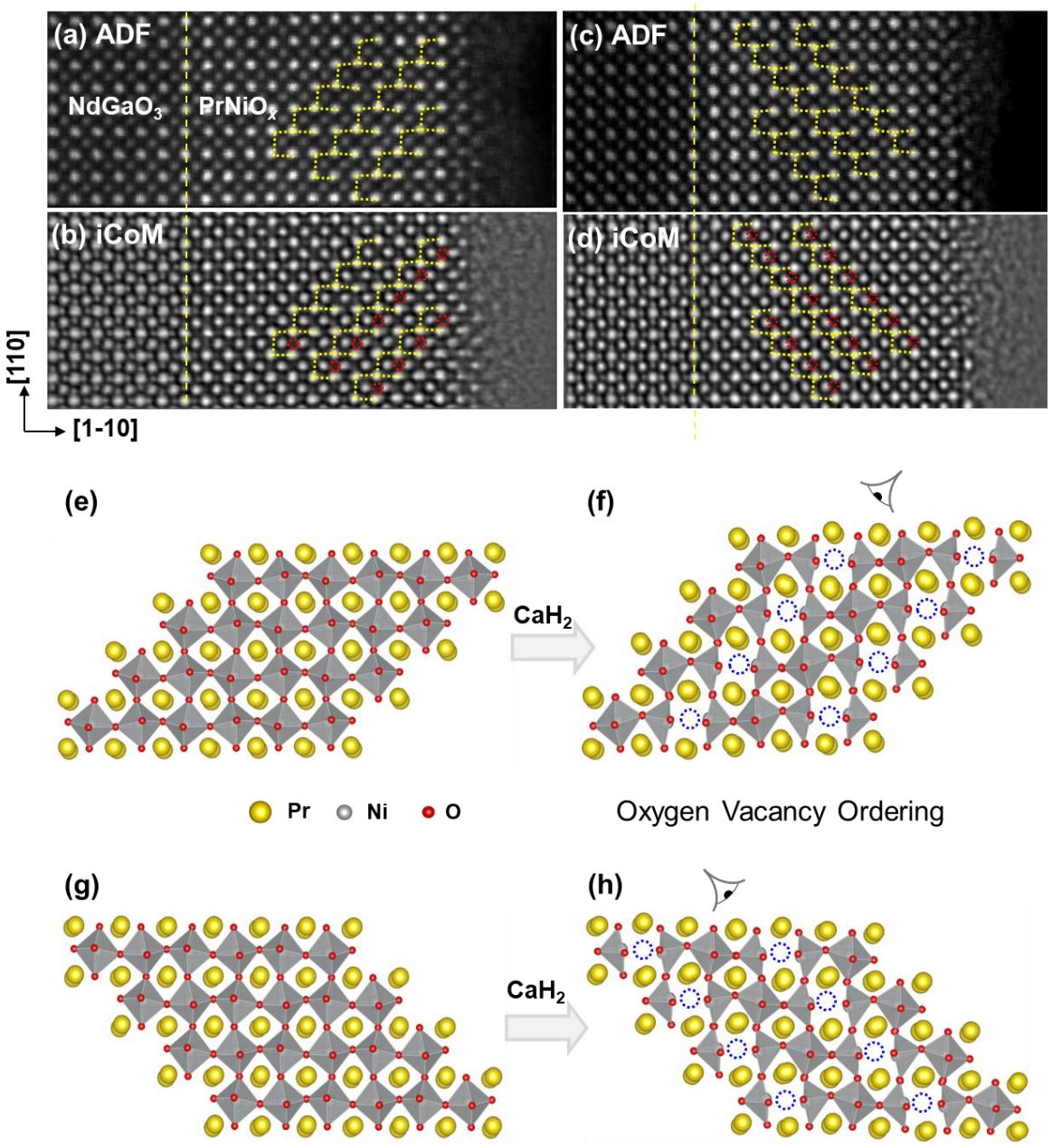

Figure 6.11 Observation of oxygen vacancy ordering and cation distortion in the reduced $PrNiO_x$ single crystal film. (a, c) ADF and (b, d) iCoM images reconstructed from the 4D dataset. The structure models of (e, g) the pristine sample and (f, h) the reduced sample with oxygen vacancy ordering. The direction of oxygen vacancy ordering is vertical in f and h. The images reconstructed from the 4D datasets are optimized by summarizing four frames.

6.4 Summary

In summary, our study provides a real-space picture of the structural distortion and electronic reconstruction induced by electrostatic effects at negatively charged polar surfaces. These different surface structures are expected to affect the electronic transport properties. The surface reconstruction varies in the pristine and partially reduced samples. Octahedral rotations and polar distortions coexist in the pristine sample, while stronger polar distortions occur in the partially reduced samples, which are closely related to the presence of oxygen vacancies. The screening lengths of the depolarization field in both pristine and reduced samples are about three unit cells. Atomic electric field mapping allows us to directly image the evolution of the electronic structure, and we observe a gradual increase in the field strength surrounding Ni atoms, indicating corresponding changes in the Ni valence state. This is in agreement with our EELS analysis. Our results demonstrate the ability of experimental methods by combining STEM-ABF, 4D-STEM, and EELS to simultaneously probe local structure and charge information, providing guidance for understanding and engineering atomic-scale polarity in functional materials.

Contributions to this chapter:

Chao Yang conceived and carried out this work and wrote this chapter. Rebecca Pons (MPI-FKF) grew the nickelate samples under the supervision of Bernhard Keimer (MPI-FKF), Eva Benckiser (MPI-FKF), and Gennady Logvenov (MPI-FKF). Hongguang Wang (MPI-FKF) contributed to the discussions on the EELS measurements, data analysis and processing. Peter A. van Aken (MPI-FKF) and Wilfried Sigle (MPI-FKF) supervised this work. The work in this chapter was supported in sample preparation by Julia Deuschle (MPI-FKF) and Marion Kelsch (MPI-FKF) and in TEM techniques by Tobias Heil (MPI-FKF), Kersten Hahn (MPI-FKF) and Peter Kopold (MPI-FKF).

Chapter 7 Summary and Outlook

In this thesis, I summarize the studies and characterizations of atomic structures and electrostatic characteristics in complex oxides and present an outlook on future developments and trends in this field of research. The research focuses primarily on the investigation of the microscopic physical and chemical properties of $SrTiO_3$ bicrystals and nickelate films. Several techniques have been used to gain insight into these materials. Nickelate samples are grown by PLD and MBE techniques with atomic layer precision. In addition, a topological method has been used to reduce the films to different phases, including the brownmillerite phase and the infinite layer phase. To study the atomic structure and electrostatic characteristics, 4D-STEM techniques were applied, allowing precise imaging of the oxygen sublattice and direct mapping of the electric field and charge density. Furthermore, STEM-EELS was used to measure the electronic structure and chemical distribution in the samples. Based on these techniques, I have gained insight into the relationship between the atomic structure and the behavior of the perovskite oxides studied in this thesis. The results and discussions contribute to the understanding of the intricate relationships between atomic arrangements and properties of these materials.

In Chapter 1, I briefly introduced the motivation for the research in this thesis and emphasized the importance of studying atomic structures and electrostatic behavior in complex oxides. The specific regions of interest highlighted include defects, interfaces, surfaces, and grain boundaries. The variations in atomic arrangements around these specific regions alter the electronic structure and influence the properties of the materials. I discussed the role of charge distribution and atomic structure on grain boundary behavior in $SrTiO_3$ bicrystals. I also discussed the relationship between atomic bonding, electronic structure, and the corresponding transport behavior in nickelates. A summary of this work is presented at the end.

In Chapter 2, the related experimental methods have been introduced, including film growth, topological reduction, STEM imaging and spectra, sample preparation, and STEM image simulations. The schematic illustrations of PLD and MBE for film growth were presented. The principle of electrostatic field and charge density mapping by 4D-STEM was introduced in detail. Other related techniques such as virtual imaging, DPC imaging, CoM imaging, and ptychographic imaging were also briefly introduced. I have also discussed the data processing software for image quantification. Quantitative analysis of STEM images is essential to determine lattice distortions and vacancy sites.

In Chapter 3, the atomic structure and electrostatic characteristics at the grain boundary in a $\Sigma 5$ $SrTiO_3$ bicrystal were investigated. Grain boundary structure and charge distribution are essential for understanding the electrical properties of many electroceramics. However, the atomic arrangement and charge measurement at the grain boundary are complicated. With the development of STEM techniques, I applied 4D-STEM techniques to image the grain boundary structure and charge distribution. By determining the oxygen sublattice, I directly reveal the polar distortion and antiferrodistortion of oxygen octahedra, which contribute to the different electrical behaviors of the ceramic. I also present the rigid body translation along the grain boundary, which is closely related to the oxygen distribution. If both cations and anions are mirror symmetric with respect to the GB plane, the strong Coulomb force between oxygen would lead to an unstable structure. Oxygen vacancy formation and rigid body

translation are effective ways to stabilize the grain boundary structure. Furthermore, I applied atomic resolution STEM-EELS to determine the elemental distribution, which showed rich Ti^{3+}, poor Sr, and less oxygen at the grain boundary.

In addition, I discussed the artifacts in the mapping of the atomic electric field and the charge density at the grain boundary. For a sample thickness of around 10-20 nm, the reconstruction of the electric field map by 4D-STEM gives qualitative results. By adjusting the focusing conditions, I observe an obvious change in the strength of momentum transfer at the grain boundary. I have simulated the electric field map for the conditions where the electron probe is focused on the entrance surface, midplane, and exit surface of a 16 nm sample, respectively. From the simulation results, I extract only the structure effects on the electric field map. When the probe is focused on the surface of the sample, the magnitude of the center of mass near the nucleus is weak and reverses direction compared to that when the probe is in-focus or under-focus at the bulk region. This effect is more pronounced at the grain boundary. Therefore, it is difficult to distinguish the pure geometry and charge effects by atomic electric field mapping at the grain boundary. For a thin sample below 5 nm, these artifacts can be minimized. However, sample preparation of such a thin sample is difficult, which depends on further optimization of FIB and other sample preparation methods in the future.

In order to obtain the space charge information at the nanoscale, it is crucial to eliminate the contribution of the atomic electric field during the reconstruction process. One approach to reduce the influence of the atomic electric field is to use a large electron beam or a thick sample. These factors help to minimize the influence of the atomic electric field and allow a more accurate reconstruction of the electric field distribution. In addition, beam tilt and sample orientation can affect the diffraction contrast, which can introduce artifacts in the electric field reconstruction. Careful consideration and control of these factors is necessary to ensure accurate results. By carefully addressing these potential effects, I was able to directly image the electric field and charge distribution at the nanoscale.

In Chapter 4, I studied the RP faults in an $NdNiO_3$ film, which was considered as a potential superconducting system. The high-resolution HAADF imaging technique was used to image different types of RP faults, consisting of $a/2<110>$ shift for RP fault A and a single intergrowth layer of $\{NdNiO_3\}$ for RP fault B. I identified the oxygen sublattice and observed the elongation of Ni-O bonds along the *z*-axis at the fault A plane. From a layer-by-layer structural perspective, the distortion of oxygen anions toward the fault plane can reduce the strong repulsion between two $[NdO]^+$ layers and achieve an energetically favorable structure. Around the RP fault B, there is no clear elongation of the Ni-O bonds, but accompanied by a visible distortion of $[NiO_6]$ octahedra. The atomically resolved EELS maps confirm the distribution of cations around the RP faults A and B. By quantitatively calculating the white line ratio, I find a decreased valence of Ni near the RP fault planes and in the fault-free NNO3 layers near the STO substrate. In the fault-free NNO3 layer far from the fault planes, the valence of Ni is close to 3+. The valence of Ni around RP fault B is lower than that around RP fault A. Moreover, I found that the in-plane tensile strain is maintained at ~2.5% for the first two unit cells before the formation of RP faults. I find that the altered valence of Ni around RP fault planes is mainly related to the variations of strain and atomic structure. On the one hand, the tensile strain might induce oxygen vacancies in the fault-free layer of $NdNiO_3$ near the substrate. On the other hand, the additional $[NdO]^+$ layer can lead to the reduced valence of Ni at RP fault regions. The particular modification of

electronic structure and stoichiometry by the RP structure can be used to tune the physical and chemical properties in other similar systems. A notable example is the achievement of superconductivity in square planar nickelates.

In Chapter 5, I have systematically investigated oxygen deintercalation and interface effects in NNO2/STO superlattices. Interface polarity plays an important role in the physical properties of oxide heterointerfaces, because it can cause specific modifications of the electronic and atomic structure. Reconstruction due to the strong polarity of the NNO2/STO interface in recently discovered superconducting nickelate films may play an important role, since no bulk superconductivity has been observed.

Using atomic resolution STEM-EELS and 4D-STEM, I have investigated the effects of oxygen distribution, polyhedral distortion, elemental intermixing, and dimensionality on the interface polarity in NNO2/STO superlattices grown on STO (001) substrates. There is a gradual variation of the oxygen content in the nickelate layer. The oxygen deintercalation process starts from the surface to the substrate. I demonstrate thickness-dependent interface reconstruction due to a polar discontinuity. An average cation displacement of ~0.025 nm at interfaces in 8NNO2/4STO superlattices is twice larger than that in 4NNO2/2STO superlattices. My results provide insight into the understanding of reconstructions at $NdNiO_2/SrTiO_3$ polar interfaces.

There are some other interesting aspects for future studies. One aspect of future studies could be to optimize the interface configuration to induce a superconducting phase in this system, where the study of the atomic arrangement at the interfaces is essential to manipulate the layers to promote superconductivity. Besides, understanding the presence and position of hydrogen atoms in the infinite layer material is crucial for explaining superconductivity and other related physical phenomena, such as charge ordering. However, the detection of hydrogen atoms by STEM is difficult due to the low concentration level and low signal intensity. The combination of multislice ptychography and STEM-EELS can help to study H atoms. In addition, the introduction of fluorine (F) into the infinite layer is another way to achieve superconductivity. The F atom is easier to detect than H atoms in STEM, and the role of F dopants in structural modifications can be resolved. Studying the effects of fluorine doping can enrich the nickelate superconducting system. These research directions highlight potential areas of exploration to further investigate the properties and behavior of the infinite layer material and its connection to superconductivity.

In Chapter 6, I focused on the surface polarity of reduced nickelates. The polarity of a surface can affect the electronic and structural properties of oxide thin films through electrostatic effects. Understanding the mechanism behind these effects requires knowledge of the atomic structure and electrostatic characteristics at the surface. In this study, I used annular bright field (ABF) imaging to investigate the surface structure of a $Pr_{0.8}Sr_{0.2}NiO_{2+x}$ ($0 < x < 1$) film. I observed a polar distortion coupled with octahedral rotations in a fully oxidized $Pr_{0.8}Sr_{0.2}NiO_3$ sample, and a stronger polar distortion in a partially reduced sample. The spatial depth extension is about three unit cells from the surface. In addition, I used four-dimensional scanning transmission electron microscopy (4D-STEM) to directly image the local atomic electric field surrounding Ni atoms near the surface and discovered distinct valence variations of Ni atoms, which were confirmed by atomic resolution electron energy loss

spectroscopy (EELS). My results suggest that the strong surface reconstruction in the reduced sample is closely related to the formation of oxygen vacancies by topochemical reduction. These results provide insight into the understanding and evolution of surface polarity at the atomic level.

An interesting extension of this project is the phase translation during topological reduction. I have observed oxygen vacancy ordering in the reduced $PrNiO_x$. However, there are more structural configurations as I discussed in the introduction in Chapter 1. In addition, the effects of strain and Sr doping on the formation of oxygen vacancy ordering may be important to explore the geometry effect in nickelates.

M.Sc. Chao Yang
Heisenbergstr. 1,
70569 Stuttgart

Declaration

Hereby I declare that this thesis titled, “Characterization of Atomic Structure and Electrostatic Characteristic in Complex Oxides by 4D-STEM and STEM-EELS” has been carried out independently by myself at the Stuttgart Center for Electron Microscopy (StEM), Max Planck Institute for Solid State Research in partial fulfillment of the requirements for the degree of Doctor of Natural Science (Dr. rer. nat.) in Materials Science from the Technical University of Darmstadt (TU Darmstadt). I certify that the work presented in this thesis is, to the best of my knowledge and belief, original and does not contain material previously published or written by anyone else, except where proper reference and permission is given.

Stuttgart

Chao Yang

MAX-PLANCK-GESELLSCHAFT

TECHNISCHE UNIVERSITÄT DARMSTADT

References

1. Ohtomo, A.; Hwang, H. Y., A high-mobility electron gas at the $LaAlO_3/SrTiO_3$ heterointerface. *Nature* **2004,** *427* (6973), 423-426.
2. Reticcioli, M.; Wang, Z.; Schmid, M.; Wrana, D.; Boatner, L. A.; Diebold, U.; Setvin, M.; Franchini, C., Competing electronic states emerging on polar surfaces. *Nat. Commun.* **2022,** *13* (1), 4311.
3. Li, L.; Richter, C.; Mannhart, J.; Ashoori, R. C., Coexistence of magnetic order and two-dimensional superconductivity at $LaAlO_3/SrTiO_3$ interfaces. *Nat. Phy.* **2011,** *7* (10), 762-766.
4. Monteiro, A. M. R. V. L.; Groenendijk, D. J.; Groen, I.; de Bruijckere, J.; Gaudenzi, R.; van der Zant, H. S. J.; Caviglia, A. D., Two-dimensional superconductivity at the (111) $LaAlO_3/SrTiO_3$ interface. *Phy. Rev. B* **2017,** *96* (2), 020504.
5. Annadi, A.; Zhang, Q.; Renshaw Wang, X.; Tuzla, N.; Gopinadhan, K.; Lu, W. M.; Roy Barman, A.; Liu, Z. Q.; Srivastava, A.; Saha, S.; Zhao, Y. L.; Zeng, S. W.; Dhar, S.; Olsson, E.; Gu, B.; Yunoki, S.; Maekawa, S.; Hilgenkamp, H.; Venkatesan, T.; Ariando, Anisotropic two-dimensional electron gas at the $LaAlO_3/SrTiO_3$ (110) interface. *Nat. Commun.* **2013,** *4*, 1838.
6. Alfthan, S. v.; Benedek, N. A.; Chen, L.; Chua, A.; Cockayne, D.; Dudeck, K. J.; Elsässer, C.; Finnis, M. W.; Koch, C. T.; Rahmati, B.; Rühle, M.; Shih, S.-J.; Sutton, A. P., The Structure of Grain Boundaries in Strontium Titanate: Theory, Simulation, and Electron Microscopy. *Annu. Rev. Mater. Res.* **2010,** *40* (1), 557-599.
7. Mercy, A.; Bieder, J.; Íñiguez, J.; Ghosez, P., Structurally triggered metal-insulator transition in rare-earth nickelates. *Nat. Commun.* **2017,** *8* (1), 1677.
8. Cohen, N.; Diéguez, O., Two types of charge ordering in bismuth nickelate. *Phy. Rev. B* **2021,** *104* (6), 064111.
9. Hepting, M.; Green, R. J.; Zhong, Z.; Bluschke, M.; Suyolcu, Y. E.; Macke, S.; Frano, A.; Catalano, S.; Gibert, M.; Sutarto, R.; He, F.; Cristiani, G.; Logvenov, G.; Wang, Y.; van Aken, P. A.; Hansmann, P.; Le Tacon, M.; Triscone, J. M.; Sawatzky, G. A.; Keimer, B.; Benckiser, E., Complex magnetic order in nickelate slabs. *Nat. Phy.* **2018,** *14* (11), 1097-1102.
10. Demazeau, G.; Marbeuf, A.; Pouchard, M.; Hagenmuller, P., Sur une série de composés oxygènes du nickel trivalent derivés de la perovskite. *J. Solid State Chem.* **1971,** *3* (4), 582-589.
11. Alonso, J. A.; Martínez-Lope, M. J.; Hidalgo, M. A., Hole and Electron Doping of $RNiO_3$ (R = La, Nd). *J. Solid State Chem.* **1995,** *116* (1), 146-156.
12. García-Muñoz, J. L.; Aranda, M. A. G.; Alonso, J. A.; Martínez-Lope, M. J., Structure and charge order in the antiferromagnetic band-insulating phase of $NdNiO_3$. *Phy. Rev. B* **2009,** *79* (13), 134432.
13. Goldschmidt, V. M., Die Gesetze der Krystallochemie. *Naturwissenschaften* **1926,** *14* (21), 477-485.
14. Catalano, S.; Gibert, M.; Fowlie, J.; Íñiguez, J.; Triscone, J. M.; Kreisel, J., Rare-earth nickelates $RNiO_3$: thin films and heterostructures. *Rep. Prog. Phys.* **2018,** *81* (4), 046501.
15. Jahn, H. A.; Teller, E.; Donnan, F. G., Stability of polyatomic molecules in degenerate electronic states - I—Orbital degeneracy. *Proc. R. Soc. A: Math. Phys. Eng.* **1937,** *161* (905), 220-235.
16. Li, D.; Lee, K.; Wang, B. Y.; Osada, M.; Crossley, S.; Lee, H. R.; Cui, Y.; Hikita, Y.; Hwang, H. Y., Superconductivity in an infinite-layer nickelate. *Nature* **2019,** *572* (7771), 624-627.
17. Lee, K.; Goodge, B. H.; Li, D.; Osada, M.; Wang, B. Y.; Cui, Y.; Kourkoutis, L. F.; Hwang, H. Y., Aspects of the synthesis of thin film superconducting infinite-layer nickelates. *APL Mater.* **2020,** *8* (4), 041107.
18. Li, Q.; He, C.; Si, J.; Zhu, X.; Zhang, Y.; Wen, H.-H., Absence of superconductivity in bulk $Nd_{1-x}Sr_xNiO_2$. *Commun. Mater.* **2020,** 1 (1), 16.
19. Hong, Y.; Byeon, P.; Bak, J.; Heo, Y.; Kim, H. S.; Bae, H. B.; Chung, S. Y., Local-electrostatics-induced oxygen octahedral distortion in perovskite oxides and insight into the structure of Ruddlesden-Popper phases. *Nat. Commun.* **2021,** *12* (1), 5527.
20. Zhang, Y.; Lin, L.-F.; Hu, W.; Moreo, A.; Dong, S.; Dagotto, E., Similarities and differences between nickelate and cuprate films grown on a $SrTiO_3$ substrate. *Phy. Rev. B* **2020,** *102* (19), 195117.

21. Geisler, B.; Pentcheva, R., Fundamental difference in the electronic reconstruction of infinite-layer versus perovskite neodymium nickelate films on $SrTiO_3$ (001). *Phy. Rev. B* **2020,** *102* (2), 104513.
22. He, R.; Jiang, P.; Lu, Y.; Song, Y.; Chen, M.; Jin, M.; Shui, L.; Zhong, Z., Polarity-induced electronic and atomic reconstruction at $NdNiO_2/SrTiO_3$ interfaces. *Phy. Rev. B* **2020,** *102* (3), 035118.
23. Liao, X.; Singh, V.; Park, H., Oxygen vacancy induced site-selective Mott transition in $LaNiO_3$. *Phy. Rev. B* **2021,** *103* (8), 085110.
24. Shin, Y.; Rondinelli, J. M., Magnetic structure of oxygen-deficient perovskite nickelates with ordered vacancies. *Phy. Rev. Res.* **2022,** 4 (2), L022069.
25. Zhang, Q.; Gao, A.; Meng, F.; Jin, Q.; Lin, S.; Wang, X.; Xiao, D.; Wang, C.; Jin, K.-j.; Su, D.; Guo, E.-J.; Gu, L., Near-room temperature ferromagnetic insulating state in highly distorted $LaCoO_{2.5}$ with CoO_5 square pyramids. *Nat. Commun.* **2021,** *12* (1), 1853.
26. Pan, G. A.; Ferenc Segedin, D.; LaBollita, H.; Song, Q.; Nica, E. M.; Goodge, B. H.; Pierce, A. T.; Doyle, S.; Novakov, S.; Córdova Carrizales, D.; N'Diaye, A. T.; Shafer, P.; Paik, H.; Heron, J. T.; Mason, J. A.; Yacoby, A.; Kourkoutis, L. F.; Erten, O.; Brooks, C. M.; Botana, A. S.; Mundy, J. A., Superconductivity in a quintuple-layer square-planar nickelate. *Nat. Mater.* **2022,** 21 (2), 160-164.
27. Benckiser, E.; Haverkort, M. W.; Bruck, S.; Goering, E.; Macke, S.; Frano, A.; Yang, X.; Andersen, O. K.; Cristiani, G.; Habermeier, H. U.; Boris, A. V.; Zegkinoglou, I.; Wochner, P.; Kim, H. J.; Hinkov, V.; Keimer, B., Orbital reflectometry of oxide heterostructures. *Nat. Mater.* **2011,** *10* (3), 189-193.
28. Frano, A.; Schierle, E.; Haverkort, M. W.; Lu, Y.; Wu, M.; Blanco-Canosa, S.; Nwankwo, U.; Boris, A. V.; Wochner, P.; Cristiani, G.; Habermeier, H. U.; Logvenov, G.; Hinkov, V.; Benckiser, E.; Weschke, E.; Keimer, B., Orbital control of noncollinear magnetic order in nickel oxide heterostructures. *Phys. Rev. Lett.* **2013,** *111* (10), 106804.
29. Wu, M.; Benckiser, E.; Haverkort, M. W.; Frano, A.; Lu, Y.; Nwankwo, U.; Brück, S.; Audehm, P.; Goering, E.; Macke, S.; Hinkov, V.; Wochner, P.; Christiani, G.; Heinze, S.; Logvenov, G.; Habermeier, H. U.; Keimer, B., Strain and composition dependence of orbital polarization in nickel oxide superlattices. *Phy. Rev. B* **2013,** *88* (12), 125124.
30. Hayward, M. A.; Rosseinsky, M. J., Cool conditions for mobile ions. *Nature* **2007,** *450* (7172), 960-961.
31. Si, L.; Xiao, W.; Kaufmann, J.; Tomczak, J. M.; Lu, Y.; Zhong, Z.; Held, K., Topotactic Hydrogen in Nickelate Superconductors and Akin Infinite-Layer Oxides ABO_2. *Phys. Rev. Lett.* **2020,** *124* (16), 166402.
32. Seddon, J.; Suard, E.; Hayward, M. A., Topotactic Reduction of $YBaCo_2O_5$ and $LaBaCo_2O_5$: Square-Planar Co(I) in an Extended Oxide. *J. Am. Chem. Soc.* **2010,** *132* (8), 2802-2810.
33. Zhang, H.; Gao, S.; Zhang, Q.; Wu, J.; Liang, J.; Dong, C.; Gu, L.; Dong, S.; Sun, J.; Liao, F.; Lin, J.; Zou, R.; Li, G., Topotactic Reduction toward a Noncentrosymmetric Deficient Perovskite Tb0.50Ca0.50Mn0.96O2.37 with Ordered Mn Vacancies and Piezoelectric Behavior. *Chem. Mater.* **2017,** *29* (22), 9840-9850.
34. Kawai, M.; Matsumoto, K.; Ichikawa, N.; Mizumaki, M.; Sakata, O.; Kawamura, N.; Kimura, S.; Shimakawa, Y., Orientation Change of an Infinite-Layer Structure $LaNiO_2$ Epitaxial Thin Film by Annealing with CaH_2. *Cryst. Growth Des.* **2010,** *10* (5), 2044-2046.
35. Kotiuga, M.; Zhang, Z.; Li, J.; Rodolakis, F.; Zhou, H.; Sutarto, R.; He, F.; Wang, Q.; Sun, Y.; Wang, Y.; Aghamiri, N. A.; Hancock, S. B.; Rokhinson, L. P.; Landau, D. P.; Abate, Y.; Freeland, J. W.; Comin, R.; Ramanathan, S.; Rabe, K. M., Carrier localization in perovskite nickelates from oxygen vacancies. *Proc. Natl. Acad. Sci. U. S. A.* **2019,** *116* (44), 21992-21997.
36. Kim, W. J.; Smeaton, M. A.; Jia, C.; Goodge, B. H.; Cho, B. G.; Lee, K.; Osada, M.; Jost, D.; Ievlev, A. V.; Moritz, B.; Kourkoutis, L. F.; Devereaux, T. P.; Hwang, H. Y., Geometric frustration of Jahn-Teller order in the infinite-layer lattice. *Nature* **2023,** *615* (7951), 237-243.
37. Hachtel, J. A.; Lupini, A. R.; Idrobo, J. C., Exploring the capabilities of monochromated electron energy loss spectroscopy in the infrared regime. *Sci. Rep.* **2018,** *8* (1), 5637.
38. Ophus, C.; Ercius, P.; Sarahan, M. C.; Czarnik, C. M.; Ciston, J. J. M.; Microanalysis, Recording and Using 4D-STEM Datasets in Materials Science. *Microsc. Microanal.* **2014,** *20*, 62-63.
39. Dekkers, N. H.; de Lang, H., DIFFERENTIAL PHASE CONTRAST IN A STEM. *Optik* **1974,** *41* (4), 452-456.

40. Chapman, J. N.; Batson, P. E.; Waddell, E. M.; Ferrier, R. P., The direct determination of magnetic domain wall profiles by differential phase contrast electron microscopy. *Ultramicroscopy* **1978,** *3*, 203-214.
41. Shibata, N.; Kohno, Y.; Findlay, S. D.; Sawada, H.; Kondo, Y.; Ikuhara, Y., New area detector for atomic-resolution scanning transmission electron microscopy. *J. Electron Microsc.* **2010,** *59* (6), 473-479.
42. Lohr, M.; Schregle, R.; Jetter, M.; Wachter, C.; Wunderer, T.; Scholz, F.; Zweck, J., Differential phase contrast 2.0--opening new "fields" for an established technique. *Ultramicroscopy* **2012,** *117*, 7-14.
43. Shibata, N.; Findlay, S. D.; Kohno, Y.; Sawada, H.; Kondo, Y.; Ikuhara, Y., Differential phase-contrast microscopy at atomic resolution. *Nat. Phy.* **2012,** *8* (8), 611-615.
44. Muller, K.; Krause, F. F.; Beche, A.; Schowalter, M.; Galioit, V.; Loffler, S.; Verbeeck, J.; Zweck, J.; Schattschneider, P.; Rosenauer, A., Atomic electric fields revealed by a quantum mechanical approach to electron picodiffraction. *Nat. Commun.* **2014,** *5*, 5653.
45. Lazic, I.; Bosch, E. G. T.; Lazar, S., Phase contrast STEM for thin samples: Integrated differential phase contrast. *Ultramicroscopy* **2016,** *160*, 265-280.
46. W. Hoppe, Beugung im Inhomogenen Prim~irstrahlwellenfeld. I. Prinzip einer Phasenmessung von Elektronenbeugungsinterferenzen. *Acta Cryst.* **1969,** *25(4)*, 495-501.
47. Guizar-Sicairos, M.; Thibault, P., Ptychography: A solution to the phase problem. *Phys. Today* **2021,** *74* (9), 42-48.
48. Spence, J. C., & Hawkes Peter, W. (Eds.). Springer Handbook of Microscopy. Springer, **2019**.
49. Pennycook, T. J.; Lupini, A. R.; Yang, H.; Murfitt, M. F.; Jones, L.; Nellist, P. D., Efficient phase contrast imaging in STEM using a pixelated detector. Part 1: experimental demonstration at atomic resolution. *Ultramicroscopy* **2015,** *151*, 160-167.
50. Rodenburg, J. M.; Bates, R. H. T., The theory of super-resolution electron microscopy via Wigner-distribution deconvolution. **1992,** *339* (1655), 521-553.
51. Rodenburg, J. M.; Faulkner, H. M. L., A phase retrieval algorithm for shifting illumination. *Appl. Phys. Lett.* **2004,** *85* (20), 4795-4797.
52. Guizar-Sicairos, M.; Fienup, J. R., Phase retrieval with transverse translation diversity: a nonlinear optimization approach. *Opt. Express* **2008,** *16* (10), 7264-7278.
53. Maiden, A. M.; Rodenburg, J. M., An improved ptychographical phase retrieval algorithm for diffractive imaging. *Ultramicroscopy* **2009,** *109* (10), 1256-1262.
54. Thibault, P.; Dierolf, M.; Menzel, A.; Bunk, O.; David, C.; Pfeiffer, F., High-Resolution Scanning X-ray Diffraction Microscopy. **2008,** *321* (5887), 379-382.
55. Nord, M.; Vullum, P. E.; MacLaren, I.; Tybell, T.; Holmestad, R., Atomap: a new software tool for the automated analysis of atomic resolution images using two-dimensional Gaussian fitting. *Adv. Struct. Chem. Imaging* **2017,** *3* (1), 9.
56. Koch, C., Determination of core structure periodicity and defect density along dislocations. Arizona State University, **2002**.
57. Madsen, J.; Susi, T., The abTEM code: transmission electron microscopy from first principles. *Open Research Europe* **2021,** 1(24), 24.
58. Xu, X.; Liu, Y.; Wang, J.; Isheim, D.; Dravid, V. P.; Phatak, C.; Haile, S. M., Variability and origins of grain boundary electric potential detected by electron holography and atom-probe tomography. *Nat. Mater.* **2020,** *19* (8), 887-893.
59. Rau, W. D.; Schwander, P.; Baumann, F. H.; Höppner, W.; Ourmazd, A., Two-Dimensional Mapping of the Electrostatic Potential in Transistors by Electron Holography. *Phys. Rev. Lett.* **1999,** *82* (12), 2614-2617.
60. Dunin-Borkowski, R. E., The development of Fresnel contrast analysis, and the interpretation of mean inner potential profiles at interfaces. *Ultramicroscopy* **2000,** *83* (3), 193-216.
61. von Alfthan, S.; Benedek, N. A.; Chen, L.; Chua, A.; Cockayne, D.; Dudeck, K. J.; Elsässer, C.; Finnis, M. W.; Koch, C. T.; Rahmati, B.; Rühle, M.; Shih, S.-J.; Sutton, A. P., The Structure of Grain Boundaries in Strontium Titanate: Theory, Simulation, and Electron Microscopy. *Annu. Rev. Mater. Res.* **2010,** *40* (1), 557-599.

62. Abou-Ras, D.; Schmidt, S. S.; Caballero, R.; Unold, T.; Schock, H.-W.; Koch, C. T.; Schaffer, B.; Schaffer, M.; Choi, P.-P.; Cojocaru-Mirédin, O., Confined and Chemically Flexible Grain Boundaries in Polycrystalline Compound Semiconductors. *Adv. Energy Mater.* **2012,** *2* (8), 992-998.
63. Shibata, N.; Seki, T.; Sanchez-Santolino, G.; Findlay, S. D.; Kohno, Y.; Matsumoto, T.; Ishikawa, R.; Ikuhara, Y., Electric field imaging of single atoms. *Nat. Commun.* **2017,** *8*, 15631.
64. Close, R.; Chen, Z.; Shibata, N.; Findlay, S. D., Towards quantitative, atomic-resolution reconstruction of the electrostatic potential via differential phase contrast using electrons. *Ultramicroscopy* **2015,** *159*, 124-37.
65. Hachtel, J. A.; Idrobo, J. C.; Chi, M., Sub-Angstrom electric field measurements on a universal detector in a scanning transmission electron microscope. *Adv. Struct. Chem. Imaging* **2018,** *4* (1), 10.
66. Gao, W.; Addiego, C.; Wang, H.; Yan, X.; Hou, Y.; Ji, D.; Heikes, C.; Zhang, Y.; Li, L.; Huyan, H.; Blum, T.; Aoki, T.; Nie, Y.; Schlom, D. G.; Wu, R.; Pan, X., Real-space charge-density imaging with sub-angstrom resolution by four-dimensional electron microscopy. *Nature* **2019,** *575* (7783), 480-484.
67. Muller-Caspary, K.; Grieb, T.; Mussener, J.; Gauquelin, N.; Hille, P.; Schormann, J.; Verbeeck, J.; Van Aert, S.; Eickhoff, M.; Rosenauer, A., Electrical Polarization in AlN/GaN Nanodisks Measured by Momentum-Resolved 4D Scanning Transmission Electron Microscopy. *Phys. Rev. Lett.* **2019,** *122* (10), 106102.
68. Waser, R., Electronic properties of grain boundaries in $SrTiO_3$ and $BaTiO_3$ ceramics. *Solid State Ion.* **1995,** *75*, 89-99.
69. Browning, N. D.; Buban, J. P.; Moltaji, H. O.; Pennycook, S. J.; Duscher, G.; Johnson, K. D.; Rodrigues, R. P.; Dravid, V. P., The influence of atomic structure on the formation of electrical barriers at grain boundaries in $SrTiO_3$. *Appl. Phys. Lett.* **1999,** *74* (18), 2638-2640.
70. Imaeda, M.; Mizoguchi, T.; Sato, Y.; Lee, H. S.; Findlay, S. D.; Shibata, N.; Yamamoto, T.; Ikuhara, Y., Atomic structure, electronic structure, and defect energetics in [001](310) Σ5 grain boundaries of $SrTiO_3$ and $BaTiO_3$. *Phy. Rev. B* **2008,** *78* (24), 245320.
71. De Souza, R. A.; Fleig, J.; Maier, J.; Zhang, Z.; Sigle, W.; Rühle, M., Electrical resistance of low-angle tilt grain boundaries in acceptor-doped $SrTiO_3$ as a function of misorientation angle. *J. Appl. Phys.* **2005,** *97* (5), 053502.
72. Koch, C. T., Determination of grain boundary potentials in ceramics: Combining impedance spectroscopy and inline electron holography. *Int. J. Mater. Res.* **2010,** *101* (1), 43-49.
73. Ravikumar, V. V.; Rodrigues, R. P.; Dravid, V. P., Direct imaging of spatially varying potential and charge across internal interfaces in solids. *Phys. Rev. Lett.* **1995,** *75* (22), 4063-4066.
74. Shao, R.; Chisholm, M. F.; Duscher, G.; Bonnell, D. A., Low-temperature resistance anomaly at $SrTiO_3$ grain boundaries: evidence for an interface-induced phase transition. *Phys. Rev. Lett.* **2005,** *95* (19), 197601.
75. Souza, R. A.; Fleig, J.; Maier, J.; Kienzle, O.; Zhang, Z.; Sigle, W.; Rühle, M., Electrical and Structural Characterization of a Low-Angle Tilt Grain Boundary in Iron-Doped Strontium Titanate. *J. Am. Ceram. Soc.* **2003,** *86* (6), 922-928.
76. Lee, S. B.; Lee, J. H.; Cho, P. S.; Kim, D. Y.; Sigle, W.; Phillipp, F., High-Temperature Resistance Anomaly at a Strontium Titanate Grain Boundary and Its Correlation with the Grain-Boundary Faceting–Defaceting Transition. *Adv. Mater.* **2007,** *19* (3), 391-395.
77. Kim, S.; Fleig, J.; Maier, J., Space charge conduction: Simple analytical solutions for ionic and mixed conductors and application to nanocrystalline ceria. *Phys. Chem. Chem. Phys.* **2003,** *5* (11), 2268-2273.
78. Rodenbücher, C.; Wrana, D.; Gensch, T.; Krok, F.; Korte, C.; Szot, K., The Electronic Properties of Extended Defects in $SrTiO_3$—A Case Study of a Real Bicrystal Boundary. *Crystals* **2020,** *10* (8), 665.
79. Moos, R.; Hardtl, K. H., Defect Chemistry of Donor-Doped and Undoped Strontium Titanate Ceramics between 1000° and 1400°C. *J. Am. Ceram. Soc.* **2005,** *80* (10), 2549-2562.
80. Lucas, G.; Burdet, P.; Cantoni, M.; Hebert, C., Multivariate statistical analysis as a tool for the segmentation of 3D spectral data. *Micron* **2013,** *52-53*, 49-56.
81. Lloyd, G. E.; Farmer, A. B.; Mainprice, D., Misorientation analysis and the formation and orientation of subgrain and grain boundaries. *Tectonophysics* **1997,** *279* (1), 55-78.

82. Pennycook, S. J.; Jesson, D. E., High-resolution incoherent imaging of crystals. *Phys. Rev. Lett.* **1990,** *64* (8), 938-941.
83. Ravikumar, V.; Dravid, V. P., Atomic structure of undoped Σ = 5 symmetrical tilt grain boundary in strontium titanate. *Ultramicroscopy* **1993,** *52* (3), 557-563.
84. Han, B.; Zhu, R.; Li, X.; Wu, M.; Ishikawa, R.; Feng, B.; Bai, X.; Ikuhara, Y.; Gao, P., Two-Dimensional Room-Temperature Giant Antiferrodistortive $SrTiO_3$ at a Grain Boundary. *Phys. Rev. Lett.* **2021,** *126* (22), 225702.
85. Choi, M.; Oba, F.; Kumagai, Y.; Tanaka, I., Anti-ferrodistortive-like oxygen-octahedron rotation induced by the oxygen vacancy in cubic $SrTiO_3$. *Adv. Mater.* **2013,** *25* (1), 86-90.
86. Sarahan, M. C.; Chi, M.; Masiel, D. J.; Browning, N. D., Point defect characterization in HAADF-STEM images using multivariate statistical analysis. *Ultramicroscopy* **2011,** *111* (3), 251-7.
87. Gao, P.; Yang, S.; Ishikawa, R.; Li, N.; Feng, B.; Kumamoto, A.; Shibata, N.; Yu, P.; Ikuhara, Y., Atomic-Scale Measurement of Flexoelectric Polarization at $SrTiO_3$ Dislocations. *Phys. Rev. Lett.* **2018,** *120* (26), 267601.
88. Zhang, Z.; Sigle, W.; Rühle, M., Atomic and electronic characterization of the [100] dislocation core in $SrTiO_3$. *Phys. Rev. B* **2002,** *66* (9), 094108.
89. Fitting, L.; Thiel, S.; Schmehl, A.; Mannhart, J.; Muller, D. A., Subtleties in ADF imaging and spatially resolved EELS: A case study of low-angle twist boundaries in $SrTiO_3$. *Ultramicroscopy* **2006,** *106* (11-12), 1053-1061.
90. Radtke, G.; Hennes, M.; Bugnet, M.; Ramasse, Q. M.; Weng, X.; Demaille, D.; Gobaut, B.; Ohresser, P.; Otero, E.; Choueikani, F.; Juhin, A.; Sainctavit, P.; Zheng, Y.; Vidal, F., Atomic-Scale Study of Metal–Oxide Interfaces and Magnetoelastic Coupling in Self-Assembled Epitaxial Vertically Aligned Magnetic Nanocomposites. *Adv. Mater. Interfaces* **2019,** *6* (17), 1900549.
91. Wang, H.; Jiang, X.; Wang, Y.; Stark, R. W.; van Aken, P. A.; Mannhart, J.; Boschker, H., Direct Observation of Huge Flexoelectric Polarization around Crack Tips. *Nano Lett.* **2020,** *20* (1), 88-94.
92. Ohtomo, A.; Muller, D. A.; Grazul, J. L.; Hwang, H. Y., Artificial charge-modulationin atomic-scale perovskite titanate superlattices. *Nature* **2002,** *419* (6905), 378-380.
93. Savitzky, B. H.; Zeltmann, S. E.; Hughes, L. A.; Brown, H. G.; Zhao, S.; Pelz, P. M.; Pekin, T. C.; Barnard, E. S.; Donohue, J.; Rangel DaCosta, L.; Kennedy, E.; Xie, Y.; Janish, M. T.; Schneider, M. M.; Herring, P.; Gopal, C.; Anapolsky, A.; Dhall, R.; Bustillo, K. C.; Ercius, P.; Scott, M. C.; Ciston, J.; Minor, A. M.; Ophus, C., py4DSTEM: A Software Package for Four-Dimensional Scanning Transmission Electron Microscopy Data Analysis. *Microsc. Microanal.* **2021,** *27* (4), 712-743.
94. Muller-Caspary, K.; Krause, F. F.; Grieb, T.; Loffler, S.; Schowalter, M.; Beche, A.; Galioit, V.; Marquardt, D.; Zweck, J.; Schattschneider, P.; Verbeeck, J.; Rosenauer, A., Measurement of atomic electric fields and charge densities from average momentum transfers using scanning transmission electron microscopy. *Ultramicroscopy* **2017,** *178*, 62-80.
95. Addiego, C.; Gao, W.; Pan, X., Thickness and defocus dependence of inter-atomic electric fields measured by scanning diffraction. *Ultramicroscopy* **2020,** *208*, 112850.
96. Rodewald, S.; Fleig, J.; Maier, J., Microcontact Impedance Spectroscopy at Single Grain Boundaries in Fe-Doped $SrTiO_3$ Polycrystals. *J. Am. Ceram. Soc.* **2001,** *84* (3), 521-530.
97. Yang, C.; Wang, Y.; Sigle, W.; van Aken, P. A., Determination of Grain-Boundary Structure and Electrostatic Characteristics in a $SrTiO_3$ Bicrystal by Four-Dimensional Electron Microscopy. *Nano Lett.* **2021,** *21* (21), 9138-9145.
98. Yang, C.; Wang, Y.; Sigle, W.; van Aken, P. A., Probing Grain-boundary Structure and Electrostatic Characteristics in a $SrTiO_3$ Bi-crystal by 4D-STEM. *Microsc. Microanal.* **2022,** *28* (S1), 592-594.
99. Li, D.; Wang, B. Y.; Lee, K.; Harvey, S. P.; Osada, M.; Goodge, B. H.; Kourkoutis, L. F.; Hwang, H. Y., Superconducting Dome in $Nd_{1-x}Sr_xNiO_2$ Infinite Layer Films. *Phys. Rev. Lett.* **2020,** *125* (2), 027001.
100. Hepting, M.; Li, D.; Jia, C. J.; Lu, H.; Paris, E.; Tseng, Y.; Feng, X.; Osada, M.; Been, E.; Hikita, Y.; Chuang, Y. D.; Hussain, Z.; Zhou, K. J.; Nag, A.; Garcia-Fernandez, M.; Rossi, M.; Huang, H. Y.; Huang, D. J.; Shen, Z. X.; Schmitt, T.; Hwang, H. Y.; Moritz, B.; Zaanen, J.; Devereaux, T. P.; Lee, W. S., Electronic structure of the parent compound of superconducting infinite-layer nickelates. *Nat. Mater.* **2020,** *19* (4), 381-385.

101. Goodge, B. H.; Li, D.; Lee, K.; Osada, M.; Wang, B. Y.; Sawatzky, G. A.; Hwang, H. Y.; Kourkoutis, L. F., Doping evolution of the Mott-Hubbard landscape in infinite-layer nickelates. *Proc. Natl. Acad. Sci. U.S.A.* **2021,** *118* (2), 2007683118.
102. Hayward, M. A.; Green, M. A.; Rosseinsky, M. J.; Sloan, J., Sodium Hydride as a Powerful Reducing Agent for Topotactic Oxide Deintercalation: Synthesis and Characterization of the Nickel(I) Oxide $LaNiO_2$. *J. Am. Chem. Soc.* **1999,** *121* (38), 8843-8854.
103. Bak, J.; Chung, S.-Y., Observation of fault-free coherent layer during Ruddlesden–Popper faults generation in LaNiO3 thin films. *J. Korean Ceram. Soc.* **2020,** *58* (2), 169-177.
104. Qi, H.; Chen, X.; Benckiser, E.; Wu, M.; Cristiani, G.; Logvenov, G.; Keimer, B.; Kaiser, U., Formation mechanism of Ruddlesden-Popper faults in compressive-strained ABO_3 perovskite superlattices. *Nanoscale* **2021,** *13* (48), 20663-20669.
105. Ruddlesden, S. N.; Popper, P., New compounds of the K_2NIF_4 type. *Acta Crystallogr.* **1957,** *10* (8), 538-539.
106. Yu, Y.; Zhang, D.; Yang, P., Ruddlesden–Popper Phase in Two-Dimensional Inorganic Halide Perovskites: A Plausible Model and the Supporting Observations. *Nano Lett.* **2017,** *17* (9), 5489-5494.
107. Detemple, E.; Ramasse, Q. M.; Sigle, W.; Cristiani, G.; Habermeier, H. U.; Keimer, B.; van Aken, P. A., Ruddlesden-Popper faults in $LaNiO_3/LaAlO_3$ superlattices. *J. Appl. Phys.* **2012,** *112* (1), 013509.
108. Li, Z.; Guo, W.; Zhang, T. T.; Song, J. H.; Gao, T. Y.; Gu, Z. B.; Nie, Y. F., Epitaxial growth and electronic structure of Ruddlesden–Popper nickelates ($La_{n+1}Ni_nO3_{n+1}$, n = 1–5). *APL Materials* **2020,** *8* (9).
109. Wang, W. Y.; Tang, Y. L.; Zhu, Y. L.; Suriyaprakash, J.; Xu, Y. B.; Liu, Y.; Gao, B.; Cheong, S. W.; Ma, X. L., Atomic mapping of Ruddlesden-Popper faults in transparent conducting $BaSnO_3$-based thin films. *Sci. Rep.* **2015,** *5*, 16097.
110. Gauquelin, N.; Benckiser, E.; Kinyanjui, M. K.; Wu, M.; Lu, Y.; Christiani, G.; Logvenov, G.; Habermeier, H. U.; Kaiser, U.; Keimer, B.; Botton, G. A., Atomically resolved EELS mapping of the interfacial structure of epitaxially strained $LaNiO_3/LaAlO_3$ superlattices. *Phys. Rev. B* **2014,** *90* (19), 195140.
111. Thind, A. S.; Luo, G.; Hachtel, J. A.; Morrell, M. V.; Cho, S. B.; Borisevich, A. Y.; Idrobo, J. C.; Xing, Y.; Mishra, R., Atomic Structure and Electrical Activity of Grain Boundaries and Ruddlesden-Popper Faults in Cesium Lead Bromide Perovskite. *Adv. Mater.* **2019,** *31* (4), e1805047.
112. Bak, J.; Bae, H. B.; Kim, J.; Oh, J.; Chung, S. Y., Formation of Two-Dimensional Homologous Faults and Oxygen Electrocatalytic Activities in a Perovskite Nickelate. *Nano Lett.* **2017,** *17* (5), 3126-3132.
113. Lee, C. H.; Orloff, N. D.; Birol, T.; Zhu, Y.; Goian, V.; Rocas, E.; Haislmaier, R.; Vlahos, E.; Mundy, J. A.; Kourkoutis, L. F.; Nie, Y.; Biegalski, M. D.; Zhang, J.; Bernhagen, M.; Benedek, N. A.; Kim, Y.; Brock, J. D.; Uecker, R.; Xi, X. X.; Gopalan, V.; Nuzhnyy, D.; Kamba, S.; Muller, D. A.; Takeuchi, I.; Booth, J. C.; Fennie, C. J.; Schlom, D. G., Exploiting dimensionality and defect mitigation to create tunable microwave dielectrics. *Nature* **2013,** *502* (7472), 532-6.
114. Jing, H. M.; Cheng, S.; Mi, S. B.; Lu, L.; Liu, M.; Cheng, S. D.; Jia, C. L., Formation of Ruddlesden-Popper Faults and Their Effect on the Magnetic Properties in $Pr_{0.5}Sr_{0.5}CoO_3$ Thin Films. *ACS Appl. Mater. Interfaces* **2018,** *10* (1), 1428-1433.
115. Oh, Y. S.; Luo, X.; Huang, F. T.; Wang, Y.; Cheong, S. W., Experimental demonstration of hybrid improper ferroelectricity and the presence of abundant charged walls in $(Ca,Sr)_3Ti_2O_7$ crystals. *Nat. Mater.* **2015,** *14* (4), 407-413.
116. Wang, W.; Zhang, H.; Shen, X.; Guan, X.; Yao, Y.; Wang, Y.; Sun, J.; Yu, R., Atomic structures of Ruddlesden-Popper faults in $LaCoO_3/SrRuO_3$ multilayer thin films induced by epitaxial strain. *J. Cryst. Growth* **2018,** *490*, 110-115.
117. Mundet, B.; Jareño, J.; Gazquez, J.; Varela, M.; Obradors, X.; Puig, T., Defect landscape and electrical properties in solution-derived $LaNiO_3$ and $NdNiO_3$ epitaxial thin films. *Phys. Rev. Materials* **2018,** *2* (6), 063607.
118. Bak, J.; Bae, H. B.; Oh, C.; Son, J.; Chung, S. Y., Effect of Lattice Strain on the Formation of Ruddlesden-Popper Faults in Heteroepitaxial $LaNiO_3$ for Oxygen Evolution Electrocatalysis. *J. Phys. Chem. Lett.* **2020,** *11* (17), 7253-7260.

119. Coll, C.; López-Conesa, L.; Magén, C.; Sanchez, F.; Fontcuberta, J.; Estradé, S.; Peiró, F., Simulation of STEM-HAADF image contrast of Ruddlesden Popper faulted $LaNiO_3$ thin films. *J. Phys. Chem. C* **2016,** 121(17), 9300-9304.
120. Palgrave, R. G.; Borisov, P.; Dyer, M. S.; McMitchell, S. R.; Darling, G. R.; Claridge, J. B.; Batuk, M.; Tan, H.; Tian, H.; Verbeeck, J.; Hadermann, J.; Rosseinsky, M. J., Artificial construction of the layered Ruddlesden-Popper manganite $La_2Sr_2Mn_3O_{10}$ by reflection high energy electron diffraction monitored pulsed laser deposition. *J. Am. Chem. Soc.* **2012,** *134* (18), 7700-14.
121. Nellist, P. D.; Pennycook, S. J., Incoherent imaging using dynamically scattered coherent electrons. *Ultramicroscopy* **1999,** *78* (1), 111-124.
122. Tan, H.; Verbeeck, J.; Abakumov, A.; Van Tendeloo, G., Oxidation state and chemical shift investigation in transition metal oxides by EELS. *Ultramicroscopy* **2012,** *116*, 24-33.
123. Ahn, C. C., Transmission electron energy loss spectrometry in materials science and the EELS atlas. John Wiley & Sons: **2006**.
124. Phillips, P. J.; Rui, X.; Georgescu, A. B.; Disa, A. S.; Longo, P.; Okunishi, E.; Walker, F.; Ahn, C. H.; Ismail-Beigi, S.; Klie, R. F., Experimental verification of orbital engineering at the atomic scale: Charge transfer and symmetry breaking in nickelate heterostructures. *Phys. Rev. B* **2017,** *95* (20), 205131.
125. Mundet, B.; Domínguez, C.; Fowlie, J.; Gibert, M.; Triscone, J.-M.; Alexander, D. T. L., Near-Atomic-Scale Mapping of Electronic Phases in Rare Earth Nickelate Superlattices. *Nano Lett.* **2021,** *21* (6), 2436-2443.
126. Ahn, C. C. K. O. L. G. I. A. S. U. H. R. E. M. F., EELS atlas : a reference collection of electron energy loss spectra covering all stable elements. Gatan, Inc.: Warrendale, Pa., **1983**.
127. Kim, T. H.; Paudel, T. R.; Green, R. J.; Song, K.; Lee, H. S.; Choi, S. Y.; Irwin, J.; Noesges, B.; Brillson, L. J.; Rzchowski, M. S.; Sawatzky, G. A.; Tsymbal, E. Y.; Eom, C. B., Strain-driven disproportionation at a correlated oxide metal-insulator transition. *Phy. Rev. B* **2020,** *101* (12), 121105.
128. Wrobel, F.; Geisler, B.; Wang, Y.; Christiani, G.; Logvenov, G.; Bluschke, M.; Schierle, E.; van Aken, P. A.; Keimer, B.; Pentcheva, R.; Benckiser, E., Digital modulation of the nickel valence state in a cuprate-nickelate heterostructure. *Phys. Rev. Mater.* **2018,** *2* (3), 035001.
129. Yang, C.; Wang, Y.; Putzky, D.; Sigle, W.; Wang, H.; Ortiz, R. A.; Logvenov, G.; Benckiser, E.; Keimer, B.; van Aken, P. A., Ruddlesden–Popper Faults in $NdNiO_3$ Thin Films. *Symmetry* **2022,** *14* (3).
130. Yang, C.; Ortiz, R.; Wang, Y.; Putzky, D.; Benckiser, E.; Keimer, B.; van Aken, P. A., Generation of Ruddlesden-Popper faults in Sr doped $NdNiO_3$. *Micro. and Microanal.* **2021,** *27* (S1), 1198-1200.
131. Comes, R. B.; Spurgeon, S. R.; Heald, S. M.; Kepaptsoglou, D. M.; Jones, L.; Ong, P. V.; Bowden, M. E.; Ramasse, Q. M.; Sushko, P. V.; Chambers, S. A., Interface-Induced Polarization in $SrTiO_3$-$LaCrO_3$ Superlattices. *Adv. Mater. Interfaces* **2016,** *3* (10), 1500779.
132. Hoglund, E. R.; Bao, D. L.; O'Hara, A.; Makarem, S.; Piontkowski, Z. T.; Matson, J. R.; Yadav, A. K.; Haislmaier, R. C.; Engel-Herbert, R.; Ihlefeld, J. F.; Ravichandran, J.; Ramesh, R.; Caldwell, J. D.; Beechem, T. E.; Tomko, J. A.; Hachtel, J. A.; Pantelides, S. T.; Hopkins, P. E.; Howe, J. M., Emergent interface vibrational structure of oxide superlattices. *Nature* **2022,** *601* (7894), 556-561.
133. Zhong, Z.; Xu, P. X.; Kelly, P. J., Polarity-induced oxygen vacancies at LaAlO3/SrTiO3 interfaces. *Phys. Rev. B* **2010,** *82* (16), 165127.
134. Chen, B.; Gauquelin, N.; Green, R. J.; Lee, J. H.; Piamonteze, C.; Spreitzer, M.; Jannis, D.; Verbeeck, J.; Bibes, M.; Huijben, M.; Rijnders, G.; Koster, G., Spatially Controlled Octahedral Rotations and Metal-Insulator Transitions in Nickelate Superlattices. *Nano Lett.* **2021,** *21* (3), 1295-1302.
135. Hayward, M. A.; Rosseinsky, M. J., Synthesis of the infinite layer Ni(I) phase $NdNiO_{2+x}$ by low temperature reduction of $NdNiO_3$ with sodium hydride. *Solid State Sci.* **2003,** *5* (6), 839-850.
136. Crespin, M.; Isnard, O.; Dubois, F.; Choisnet, J.; Odier, P., $LaNiO_2$: Synthesis and structural characterization. *J. Solid State Chem.* **2005,** *178* (4), 1326-1334.
137. Osada, M.; Wang, B. Y.; Goodge, B. H.; Harvey, S. P.; Lee, K.; Li, D.; Kourkoutis, L. F.; Hwang, H. Y., Nickelate Superconductivity without Rare-Earth Magnetism: $(La,Sr)NiO_2$. *Adv. Mater.* **2021,** *33* (45), 2104083.

138. Osada, M.; Wang, B. Y.; Goodge, B. H.; Lee, K.; Yoon, H.; Sakuma, K.; Li, D.; Miura, M.; Kourkoutis, L. F.; Hwang, H. Y., A Superconducting Praseodymium Nickelate with Infinite Layer Structure. *Nano Lett.* **2020,** *20* (8), 5735-5740.
139. Zhang, Y.; Lin, L.-F.; Hu, W.; Moreo, A.; Dong, S.; Dagotto, E., Similarities and differences between nickelate and cuprate films grown on a $SrTiO_3$ substrate. *Phys. Rev. B* **2020,** *102* (19), 195117.
140. Reyren, N.; Thiel, S.; Caviglia, A. D.; Kourkoutis, L. F.; Hammerl, G.; Richter, C.; Schneider, C. W.; Kopp, T.; Rüetschi, A.-S.; Jaccard, D.; Gabay, M.; Muller, D. A.; Triscone, J.-M.; Mannhart, J., Superconducting Interfaces Between Insulating Oxides. *Science* **2007,** *317* (5842), 1196-1199.
141. Thiel, S.; Hammerl, G.; Schmehl, A.; Schneider, C. W.; Mannhart, J., Tunable Quasi-Two-Dimensional Electron Gases in Oxide Heterostructures. *Science* **2006,** *313* (5795), 1942-1945.
142. Dagotto, E., The conducting face of an insulator. *Nature* **2011,** *469* (7329), 167-168.
143. Lee, P. W.; Singh, V. N.; Guo, G. Y.; Liu, H. J.; Lin, J. C.; Chu, Y. H.; Chen, C. H.; Chu, M. W., Hidden lattice instabilities as origin of the conductive interface between insulating $LaAlO_3$ and $SrTiO_3$. *Nat. Commun.* **2016,** *7*, 12773.
144. Goodge, B. H.; Geisler, B.; Lee, K.; Osada, M.; Wang, B. Y.; Li, D.; Hwang, H. Y.; Pentcheva, R.; Kourkoutis, L. F. Resolving the polar interface of infinite-layer nickelate thin films, *Nat. Mater.* **2023**, 22(4), 466-473.
145. Ortiz, R. A.; Menke, H.; Misják, F.; Mantadakis, D. T.; Fürsich, K.; Schierle, E.; Logvenov, G.; Kaiser, U.; Keimer, B.; Hansmann, P.; Benckiser, E., Superlattice approach to doping infinite-layer nickelates. *Phys. Rev. B* **2021,** *104* (16), 165137.
146. Paterson, G. W.; Webster, R. W. H.; Ross, A.; Paton, K. A.; Macgregor, T. A.; McGrouther, D.; MacLaren, I.; Nord, M., Fast Pixelated Detectors in Scanning Transmission Electron Microscopy. Part II: Post-Acquisition Data Processing, Visualization, and Structural Characterization. *Microsc. Microanal.* **2020,** *26* (5), 944-963.
147. Noguera, C., Polar oxide surfaces. *J. Condens. Matter Phys.* **2000,** *12* (31), 367-410.
148. Curnan, M. T.; Kitchin, J. R., Effects of Concentration, Crystal Structure, Magnetism, and Electronic Structure Method on First-Principles Oxygen Vacancy Formation Energy Trends in Perovskites. *J. Phys. Chem. C* **2014,** *118* (49), 28776-28790.
149. Malashevich, A.; Ismail-Beigi, S., First-principles study of oxygen-deficient $LaNiO_3$ structures. *Phys. Rev. B* **2015,** *92* (14), 144102.
150. Roberto, A. O., Structural, electronic and magnetic properties of infinite-layer nickelate heterostructures and polycrystals. University of Stuttgart. **2022**.
151. Zhong, Z.; Koster, G.; Kelly, P. J., Prediction of thickness limits of ideal polar ultrathin films. *Phys. Rev. B* **2012,** *85* (12), 121411.
152. Evjen, H. M., On the Stability of Certain Heteropolar Crystals. *Phys. Rev.* **1932,** *39* (4), 675-687.
153. Yang, C.; Ortiz, R. A.; Wang, Y.; Sigle, W.; Wang, H.; Benckiser, E.; Keimer, B.; van Aken, P. A., Atomic Insights of Interface Polarity in $NdNiO_2/SrTiO_3$ Superlattices. *Microsc. Microanal.* **2023,** *29*, 321-322.
154. Yang, C.; Ortiz, R. A.; Wang, Y.; Sigle, W.; Wang, H.; Benckiser, E.; Keimer, B.; van Aken, P. A., Thickness-Dependent Interface Polarity in Infinite-Layer Nickelate Superlattices. *Nano Lett.* **2023**, 23, 3291–3297.
155. Hwang, H. Y.; Iwasa, Y.; Kawasaki, M.; Keimer, B.; Nagaosa, N.; Tokura, Y., Emergent phenomena at oxide interfaces. *Nat. Mater.* **2012,** *11* (2), 103-13.
156. Lazarov, V. K.; Chambers, S. A.; Gajdardziska-Josifovska, M., Polar oxide interface stabilization by formation of metallic nanocrystals. *Phys. Rev. Lett.* **2003,** *90* (21), 216108.
157. Song, K.; Min, T.; Seo, J.; Ryu, S.; Lee, H.; Wang, Z.; Choi, S. Y.; Lee, J.; Eom, C. B.; Oh, S. H., Electronic and Structural Transitions of $LaAlO_3/SrTiO_3$ Heterostructure Driven by Polar Field-Assisted Oxygen Vacancy Formation at the Surface. *Adv. Sci.* **2021,** *8* (14), 2002073.
158. Zubko, P.; Gariglio, S.; Gabay, M.; Ghosez, P.; Triscone, J.-M., Interface Physics in Complex Oxide Heterostructures. *Annu. Rev. Condens. Matter Phys.* **2011,** *2* (1), 141-165.
159. Goniakowski, J.; Finocchi, F.; Noguera, C., Polarity of oxide surfaces and nanostructures. *Rep. Prog. Phys.* **2008,** *71* (1), 016501.

160. De Luca, G.; Spring, J.; Kaviani, M.; Johr, S.; Campanini, M.; Zakharova, A.; Guillemard, C.; Herrero-Martin, J.; Erni, R.; Piamonteze, C.; Rossell, M. D.; Aschauer, U.; Gibert, M., Top-Layer Engineering Reshapes Charge Transfer at Polar Oxide Interfaces. *Adv. Mater.* **2022,** *34* (36), e2203071.
161. Lee, H. N.; Christen, H. M.; Chisholm, M. F.; Rouleau, C. M.; Lowndes, D. H., Strong polarization enhancement in asymmetric three-component ferroelectric superlattices. *Nature* **2005,** *433* (7024), 395-399.
162. Benedetti, S.; Nilius, N.; Torelli, P.; Renaud, G.; Freund, H. J.; Valeri, S., Competition between Polar and Nonpolar Growth of MgO Thin Films on Au(111). *J. Phys. Chem. C* **2011,** *115* (46), 23043-23049.
163. Ju, L.; Tang, X.; Kou, L., Polarization boosted catalysis: progress and outlook. *Microstructures* **2022**, 2, 2022008.
164. Gao, P.; Liu, H. J.; Huang, Y. L.; Chu, Y. H.; Ishikawa, R.; Feng, B.; Jiang, Y.; Shibata, N.; Wang, E. G.; Ikuhara, Y., Atomic mechanism of polarization-controlled surface reconstruction in ferroelectric thin films. *Nat. Commun.* **2016,** *7*, 11318.
165. Gazquez, J.; Stengel, M.; Mishra, R.; Scigaj, M.; Varela, M.; Roldan, M. A.; Fontcuberta, J.; Sanchez, F.; Herranz, G., Competition between Polar and Nonpolar Lattice Distortions in Oxide Quantum Wells: New Critical Thickness at Polar Interfaces. *Phys. Rev. Lett.* **2017,** *119* (10), 106102.
166. Kumah, D. P.; Malashevich, A.; Disa, A. S.; Arena, D. A.; Walker, F. J.; Ismail-Beigi, S.; Ahn, C. H., Effect of Surface Termination on the Electronic Properties of $LaNiO_3$ Films. *Phys. Rev. A* **2014,** *2* (5), 054004.
167. Medarde, M.; Fontaine, A.; Garcia-Munoz, J. L.; Rodriguez-Carvajal, J.; de Santis, M.; Sacchi, M.; Rossi, G.; Lacorre, P., $RNiO_3$ perovskites (R=Pr,Nd): Nickel valence and the metal-insulator transition investigated by x-ray-absorption spectroscopy. *Phys. Rev. B Condens. Matter* **1992,** *46* (23), 14975-14984.
168. Disa, A. S.; Kumah, D. P.; Ngai, J. H.; Specht, E. D.; Arena, D. A.; Walker, F. J.; Ahn, C. H., Phase diagram of compressively strained nickelate thin films. *APL Mater.* **2013,** *1* (3), 032110.
169. Fowlie, J.; Gibert, M.; Tieri, G.; Gloter, A.; Iniguez, J.; Filippetti, A.; Catalano, S.; Gariglio, S.; Schober, A.; Guennou, M.; Kreisel, J.; Stephan, O.; Triscone, J. M., Conductivity and Local Structure of $LaNiO_3$ Thin Films. *Adv. Mater.* **2017,** *29* (18), 1605197.
170. Tam, C. C.; Choi, J.; Ding, X.; Agrestini, S.; Nag, A.; Wu, M.; Huang, B.; Luo, H.; Gao, P.; Garcia-Fernandez, M.; Qiao, L.; Zhou, K. J., Charge density waves in infinite-layer $NdNiO_2$ nickelates. *Nat. Mater.* **2022,** *21* (10), 1116-1120.
171. Krieger, G.; Martinelli, L.; Zeng, S.; Chow, L. E.; Kummer, K.; Arpaia, R.; Moretti Sala, M.; Brookes, N. B.; Ariando, A.; Viart, N.; Salluzzo, M.; Ghiringhelli, G.; Preziosi, D., Charge and Spin Order Dichotomy in $NdNiO_2$ Driven by the Capping Layer. *Phys. Rev. Lett.* **2022,** *129* (2), 027002.
172. Rossi, M.; Osada, M.; Choi, J.; Agrestini, S.; Jost, D.; Lee, Y.; Lu, H.; Wang, B. Y.; Lee, K.; Nag, A.; Chuang, Y.-D.; Kuo, C.-T.; Lee, S.-J.; Moritz, B.; Devereaux, T. P.; Shen, Z.-X.; Lee, J.-S.; Zhou, K.-J.; Hwang, H. Y.; Lee, W.-S., A broken translational symmetry state in an infinite-layer nickelate. *Nat. Phys.* **2022,** *18* (8), 869-873.
173. Chen, H.; Kumah, D. P.; Disa, A. S.; Walker, F. J.; Ahn, C. H.; Ismail-Beigi, S., Modifying the electronic orbitals of nickelate heterostructures via structural distortions. *Phys. Rev. Lett.* **2013,** *110* (18), 186402.
174. Han, M. J.; van Veenendaal, M., Electronic structure and orbital polarization of $LaNiO_3$ with a reduced coordination and under strain: A first-principles study. *Phys. Rev. B* **2011,** *84* (12), 125323..
175. Geisler, B.; Pentcheva, R., Correlated interface electron gas in infinite-layer nickelate versus cuprate films on $SrTiO_3$(001). *Phys. Rev. Res.* **2021,** *3* (1), 013261.
176. Kumah, D. P.; Disa, A. S.; Ngai, J. H.; Chen, H.; Malashevich, A.; Reiner, J. W.; Ismail-Beigi, S.; Walker, F. J.; Ahn, C. H., Tuning the structure of nickelates to achieve two-dimensional electron conduction. *Adv. Mater.* **2014,** *26* (12), 1935-40.
177. Bousquet, E.; Dawber, M.; Stucki, N.; Lichtensteiger, C.; Hermet, P.; Gariglio, S.; Triscone, J. M.; Ghosez, P., Improper ferroelectricity in perovskite oxide artificial superlattices. *Nature* **2008,** *452* (7188), 732-6.